MICROFLUIDIC SYSTEMS FOR INVESTIGATING BACTERIAL CHEMOTAXIS AND COLONIZATION

A Dissertation

by

DEREK LYNN ENGLERT

Submitted to the Office of Graduate Studies of
Texas A&M University
in partial fulfillment of the requirements for the degree of

DOCTOR OF PHILOSOPHY

December 2009

Major Subject: Chemical Engineering

MICROFLUIDIC SYSTEMS FOR INVESTIGATING BACTERIAL CHEMOTAXIS AND COLONIZATION

A Dissertation

by

DEREK LYNN ENGLERT

Submitted to the Office of Graduate Studies of
Texas A&M University
in partial fulfillment of the requirements for the degree of

DOCTOR OF PHILOSOPHY

Approved by:

Chair of Committee,	Arul Jayaraman
Committee Members,	Thomas K. Wood
	Victor M. Ugaz
	Suresh D. Pillai
Head of Department,	Michael V. Pishko

December 2009

Major Subject: Chemical Engineering

ABSTRACT

Microfluidic Systems for Investigating Bacterial Chemotaxis and Colonization.

(December 2009)

Derek Lynn Englert, B.S., University of Mississippi

Chair of Advisory Committee: Dr. Arul Jayaraman

The overall goal of this work was to develop and utilize microfluidic models for investigating bacterial chemotaxis and biofilm formation - phenotypes that play key roles in bacterial infections. Classical methods for investigating chemotaxis and biofilm formation have many limitations and drawbacks. These include being unsuitable for investigating the effect of chemorepellents, non-quantitative readouts, and not accounting for interaction between hydrodynamics and biofilm formation. The novel microfluidic model systems for chemotaxis and biofilm formation developed in this study addresses these drawbacks.

Chemotaxis model system development was done in three stages. We first developed two static chemotaxis model systems – the two fluorophore chemotaxis agarose plug assay and the μPlug assay - for rapidly determining the extent of chemotaxis in a qualitative manner. A key feature of these model systems was the incorporation of dead cells and differential labeling with green and red fluorescent proteins for partitioning the effects of movement due to fluid flow from chemotaxis. The static systems were used to rapidly screen a wide range of conditions for use in the flow-

based μFlow chemotaxis model system. The effect of four major variables - cell preparation method, gradient strength, flow rate in the device, and imaging position - that influence the chemotactic response in the μFlow was characterized using the repellent taxis from Ni^{2+} gradients as the model chemoeffector.

Using the μFlow chemotaxis device, we investigated the chemotaxis of *Escherichia coli* RP437 to different signals that are present in the human gastrointestinal tract and are likely to be mediators of infection through their effect on chemotaxis. Our data show that the bacterial signal indole is a repellent, while the signals autoinducer-2 (AI-2) and isatin are attractants for *E. coli* RP437. However, cells exposed to a competing gradient of indole and either AI-2 or isatin, attracts *E. coli*. The μFlow device was also used to refute a long-standing view on how the repellent Ni^{2+} is sensed in *E. coli*. Our data show that only the Tar chemoreceptor is needed for sensing Ni^{2+} and the nickel binding protein, NikA, and the Ni^{2+} transport system proteins, NikB and NikC, are not required for repellent taxis from nickel.

A microfluidic biofilm model was also developed in this study and used in conjunction with a mathematical model to investigate biofilm formation and quorum sensing in closed systems (where biofilm growth and hydrodynamics are interdependent). The mathematical model predictions were experimentally validated using *Pseudomonas aeruginosa* PA14 in a microfluidic biofilm system at various flow rates.

DEDICATION

To my loving and understanding wife Shannon,

who has always supported me even when my decision meant being apart for so long.

To our daughter Mary Dianna “Maddie”,

who gave me a firm deadline for finishing.

To my mother Dianna,

who was always cheering me on and encouraging me to do my best.

To God,

without Him, all would be for nothing.

ACKNOWLEDGEMENTS

I would like to thank my committee chair Dr. Arul Jayaraman for allowing me to develop my ideas and troubleshoot my experiments. But also knowing when a small nudge is needed in the right direction. It was truly a pleasure working with him.

I will be eternally grateful to my committee members Dr. Suresh D. Pillai, Dr. Victor M. Ugaz, and Dr. Thomas K. Wood for their time and understanding.

I would like to thank our collaborator Dr. Mike D. Manson for all his knowledge of *E. coli* and chemotaxis and maybe most importantly, his name and reputation. With his name and support, the µPlug and µFlow devices may garner wide spread use for studying chemotaxis amongst microbiologists.

I would like to thank my colleagues in Dr. Jayaraman's lab, Dr. Jeongyun Kim, Tarun Bansal, Manjunath Hegde, Sunho Kim, Colby Moya, Billy Newton, and Fatih Senocak. I would also like to thank my colleague in Dr. Manson's lab Chris Adase for the nickel mutants used in Chapter VI. I would like to thank Vijay Janakiraman for his work on the model created in Chapter VII.

I appreciate the partial support of my research from the National Science Foundation.

Lastly, I would like to think my family and friends for all their support and encouragement throughout the years I have been working to complete this degree.

TABLE OF CONTENTS

Page

ABSTRACT iii

DEDICATION v

ACKNOWLEDGEMENTS vi

TABLE OF CONTENTS vii

LIST OF FIGURES ix

LIST OF TABLES xi

CHAPTER

I INTRODUCTION 1

1.1 Background 1
1.2 Motivation 3
1.3 Research Objectives, Importance, and Novelty 4

II LITERATURE REVIEW 12

2.1 Origins of Bacterial Motility and Chemotaxis Studies 12
2.2 How Bacteria Move During Chemotaxis 12
2.3 Established Methods for Assaying Bacterial Chemotaxis 14
2.4 Mathematical Modeling of Biofilm Formation 21

III MICROFLUIDIC CHEMOTAXIS METHOD DEVELOPMENT 24

3.1 Overview 24
3.2 Two-Fluorophore Agarose Plug Assay 26
3.3 Microplug 27
3.4 Microflow Chemotaxis Device 31

IV EXPERIMENTAL DESIGN VARIABLES FOR THE μFLOW DEVICE 35

CHAPTER Page

V FLOW-BASED MICROFLUIDIC DEVICE FOR QUANTIFYING BACTERIAL CHEMOTAXIS IN STABLE, COMPETING GRADIENTS 43

5.1 Overview 43
5.2 Introduction 44
5.3 Materials and Methods 46
5.4 Results 54
5.5 Discussion 63

VI REPELLENT TAXIS TO NICKEL ION REQUIRES NEITHER NI^{2+} TRANSPORT NOR THE PERIPLASMIC NIKA BINDING PROTEIN 68

VII MODELING GROWTH AND QUORUM SENSING IN BIOFILMS GROWN IN MICROFLUIDIC CHAMBERS 78

7.1 Overview 78
7.2 Introduction 79
7.3 Methods 81
7.4 Results 92
7.5 Discussion 103

VIII CONCLUSIONS AND RECOMMENDATIONS 109

8.1 Conclusions 109
8.2 Recommendations 111

REFERENCES 113

APPENDIX MATLAB CODE 133

VITA 186

LIST OF FIGURES

FIGURE		Page
1.1	Representative drawing of lumen	7
3.1	Agarose plug assay	28
3.2	Sample images of the TFCA plug assay after 30 minutes	28
3.3	µPlug chemotaxis device design	29
3.4	Characterization of gradient formation in the µPlug device	30
3.5	Fluorescent images of chemotaxis by E. coli strain RP437 in the µPlug and µFlow devices	31
3.6	Schematic of the µFlow gradient chemotaxis device	33
3.7	Sample µFlow device images	34
4.1	Quantification of migration profiles	36
4.2	Effect of the cell preparation method on chemotaxis	39
4.3	Effect of gradient strength on chemotaxis	40
4.4	Effect of flow rate on chemotaxis	41
5.1	The µFlow chemotaxis device	49
5.2	Formation of concentration gradients in the µFlow device	50
5.3	Chemotaxis in response to gradients of L-aspartate and $NiSO_4$	56
5.4	Quantification of migration profiles to a canonical attractant and repellent	57
5.5	Migration profiles in response to gradients of potential chemoeffectors	61
5.6	Migration profiles in response to combined gradients of potential chemoeffectors	62

FIGURE Page

6.1 PCR products of *nik*-knockout genes in strain CV1 71

6.2 Primer sequences and their locations in the *nik* operon 72

6.3 Distribution of wild-type and *nik*-knockout strains in a $NiSO_4$ gradient ... 73

6.4 Chemotaxis in a $NiSO_4$ gradient 74

7.1 Schematic representation of biofilm model 84

7.2 Schematic of the microfluidic model used for experimental investigation of biofilm thickness 92

7.3 Model predictions for biofilm thickness 94

7.4 Model predictions for oxygen levels 96

7.5 Model predictions for QS molecules..... 98

7.6 Experimental results for biofilm thickness..... 99

7.7 IMARIS representation of *P. aeruginosa* biofilms 101

7.8 Parameter sensitivity analysis of biofilm thickness 102

LIST OF TABLES

TABLE		Page
1.1	Primary chemoreceptors of *E. coli* O157:H7	7
2.1	Advantages and disadvantages of chemotaxis assays	22
4.1	CPC/CMC data for experimental design	38
5.1	CPC and CMC values of RP437 and RP437 Δ*tar* cells for concentration gradients of different chemoeffectors	59
6.1	Chemotaxis partition and migration coefficients in a $NiSO_4$ gradient	77
7.1	List of parameters used in simulation	89

CHAPTER I

INTRODUCTION

1.1 Background

It has been estimated that 99% of bacteria are associated with surfaces (30, 36). Bacteria can colonize on numerous surfaces and form organized structures known as biofilms (36, 101). Biofilms are ubiquitous and found in a broad range of environments on Earth (ship hulls, heat exchangers, drinking water reservoirs), in the human body (medical device implants, the gastrointestinal (GI) tract, the lungs of cystic fibrosis (CF) patients), and even on a space shuttle (36, 50, 72, 78, 117). Once biofilms have formed, they are extremely hard to eradicate (87, 91). Studies have shown that biofilms can be 10-1000 times more resistant to biocides than planktonic (suspension) cultures (91). Therefore, it is important to develop alternate approaches for controlling biofilm formation. A greater understanding of the different steps underlying biofilm development (e.g., the migration of bacteria to surfaces, competition with native bacteria species) could lead to the development of new approaches for combating infections.

As with most bacterial species, pathogenic bacteria are also often found associated with surfaces. Colonization of host tissue by pathogenic bacteria is a prelude to the infection process. Since many deadly pathogens are not indigenous and enter the body orally (e.g., as part of contaminated food), the first step in the infection process is

---

This dissertation follows the style of Applied and Environmental Microbiology.

often attachment to host tissue. More generally, the infection process can be thought of to occur in 3 distinct steps: an initial migration of the pathogen to the surface it is colonizing, the actual colonization of host cell surfaces, and invasion or injection of toxins to damage the host cell. However, not all bacteria need to form biofilms for infections to take place. For example, it is not clear that biofilm formation is necessary for *Escherichia coli* O157:H7 (EHEC) infections; instead, microcolony formation and attachment to host cells may be sufficient to initiate infection. In this case, recognition of the GI tract environment and migration is the required first step for EHEC infections. Previous work using *Helicobacter pylori* in an *in vivo* model suggest that chemotaxis is an important part of migration and attachment, as non-motile chemotaxis mutants had reduced attachment (95, 138). These studies clearly demonstrate the importance of the initial migration step in bacterial infection of the GI tract. A major portion of the work described in this study focuses on new methods and tools for investigating bacterial migration.

In some cases, infections do not start with migration as the pathogen is already present inside the human body (i.e., an opportunistic infection). In this case, colonization, and not migration, is an important determinant of infection (106). *P. aeruginosa* is the best-known example of an opportunistic pathogen present in the lungs of cystic fibrosis patients. The bacteria entering the lung through inhaled air become trapped in the thick mucus accumulated in lungs of cystic fibrosis patients. While the bacteria do migrate to the surface on their own, *P. aeruginosa* is able to easily attach because the thick mucus produced in their lungs inhibits the ability to expel bacteria via

coughing. Therefore, the important step in *P. aeruginosa* infections is not migration but the persistence of the pathogen in an attached lifestyle which leads to formation of biofilms. A second minor aspect of my research focuses on developing methods for investigating opportunistic pathogen colonization.

1.2 Motivation

Biofilm formation in the body is responsible for chronic relapses of bacterial infections (36). Traditional methods used to treat these bacterial infections kill some of the biofilm bacteria but do not completely destroy the biofilm that is the cause of the infection. Infection usually persists as the biofilm gradually redevelops. These ineffective treatments have significant economic implications. For example, there are nearly 73,000 reported EHEC infections annually in the gastrointestinal (GI) tract that lead to over 2000 hospitalizations and 60 deaths with total costs of $403 million (49). To make matters worse, a studies link antibiotic treatment for EHEC infection with greatly increasing the risk of hemolytic-uremic syndrome and renal failure (122, 141) and an increased mortality rate (28). *In vitro* experiments have shown that treatment with antibiotics actually enhances EHEC infections (141), as the genes responsible for shiga toxin production are controlled by the SOS response in EHEC and any stress (such as the presence of antibiotics) increases lysis of EHEC releasing shiga toxins. Therefore, understanding the mechanisms underlying bacterial migration to and colonization of surfaces, could lead to the development of novel treatments against bacterial infections.

Worldwide there are approximately 70,000 people diagnosed with CF annually (137). As many as 95% of CF patients die of respiratory failure brought about by chronic bacterial infection (88). *P. aeruginosa* has been shown to be the main cause of mortality (88, 99). By the time CF patients reach adolescence, 80% will have acquired *P. aeruginosa* in their lungs (88). Unfortunately, there is an emergence of antibiotic resistant bacteria (137) which makes it more difficult to combat these infections. The ability of *P. aeruginosa* to form a biofilm is one aspect of pathogenesis of chronic lung infection in CF patients (88). Therefore, it is important to study *P. aeruginosa* biofilm formation so that new approaches for disrupting biofilm formation can be identified.

1.3 Research Objectives, Importance, and Novelty

The overall goal of this work was to develop microfluidics-based tools for investigating the mechanisms involved in bacterial infection, specifically on the two initial steps of infection – chemotactic migration and colonization. The proposed work ranges from the development of novel microfluidic devices, to investigating mechanisms of signal recognition, to understanding the interaction between signals in regulating these phenotypes.

The major focus of this dissertation is on investigating the migration of bacteria towards surfaces; which is considered the first step in bacterial colonization and biofilm formation. A key question in bacterial migration during infection is: What are the driving forces underlying migration? This question has specific significance in EHEC infections as this pathogen does not randomly colonize the GI tract; instead, colonization

occurs almost always in the colon (large intestine). However, the colon is not the first section of the GI tract encountered by EHEC, as it passes from the stomach through the small intestine to reach the large intestine. In other words, it has been proposed that EHEC 'recognizes' its surroundings to initiate infection (73). Therefore, it is reasonable to speculate that the colon microenvironment plays a significant role in the initial migration of EHEC towards intestinal epithelial cells.

A distinguishing feature of the colon microenvironment is the abundance of both eukaryotic and bacterial cell signals. This signal environment arises primarily due to the organization of host cells and bacteria in the GI tract, as intestinal epithelial cells and non-pathogenic bacterial microflora exist in close proximity with one another. Cell signals are integral to the functioning of both cell types. Eukaryotic hormones (e.g., epinephrine, norepinephrine) are produced *in situ* in the GI tract through the enteric nervous system (9, 89) and are involved in controlling intestinal functions such as solute transport, defense, etc. It has been estimated that the GI tract is enervated with more than a million nerve endings (89); therefore, the local concentration of hormones is likely to be very high in the GI tract. For example, biogenic amines such as dopamine, serotonin, and norepinephrine are all produced locally in the GI tract, and nearly 60% of the norepinephrine in the body is produced by the enteric nervous system (51). Thus, the GI tract is enriched in eukaryotic hormones. Norepineprine in concentrations of 50-500 µM have been used to represent the physiological conditions of the lumen (64).

Large numbers (~ 10^{14}) of non-pathogenic bacteria also live in the GI tract, and utilize different cell-cell communication signals for metabolic cooperation and

communication. These include quorum sensing signals such as autoinducer-2 (AI-2), autoinducer-3 (AI-3), and stationary phase signals such as indole that are produced by non-pathogenic *E. coli*. The diversity in the bacterial microflora and the high cell density results in a diverse range of prokaryotic signals being present in the GI tract as well.

A second layer of complexity associated with these signals is that the concentration of signals is not expected to be uniform in the GI tract. **Figure 1.1** gives a graphical view of the lumen in the GI tract. This heterogeneity arises due to the organization of the different signal sources as well as the flow characteristics. Hormones or hormone precursors are produced on the basolateral side of the epithelial cells and diffuse into the intestinal lumen. This results in a radial concentration profile of hormones (i.e., diffusing from a point source and spreading outward). The distribution of bacterial microflora in the lumen is also not uniform as the bacteria often are often clustered together based on metabolic requirements. While some signals are produced by several bacterial species (e.g., AI-2 is a universal inter-species signal that is produced by nearly 55 bacterial species), some signals are produced only by specific bacteria (e.g., indole is produced by *E. coli*). Thus, there is likely to be heterogeneity in the production of the different signals. Second, the intestinal lumen is not static and the flow through the lumen can also cause variations in the spatial distribution of signals. Together, this leads to concentration gradients of signals being formed in the bacterial lumen.

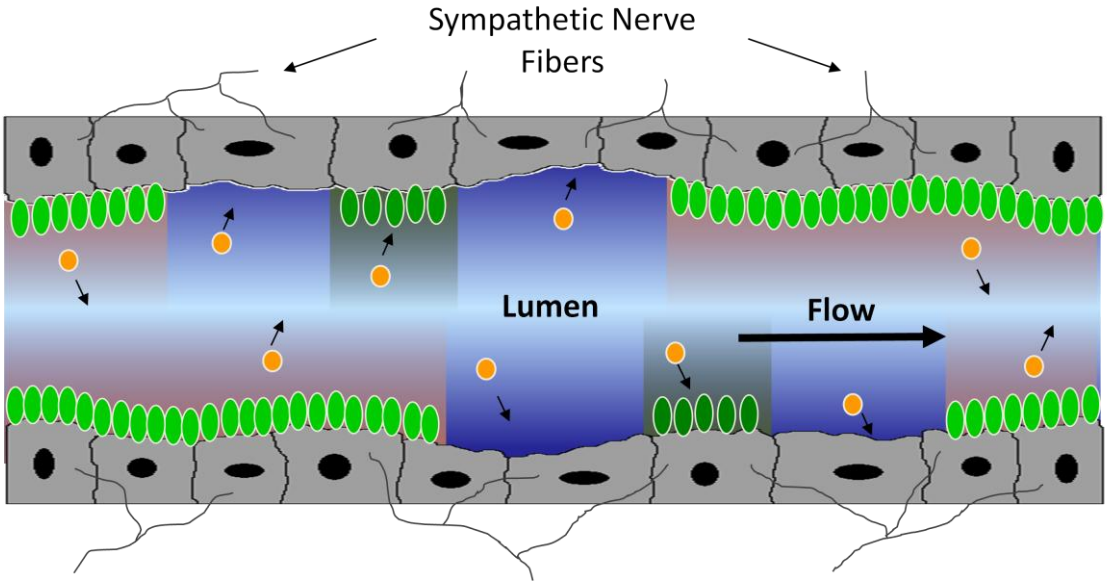

Figure 1.1: Representative drawing of lumen.

Table 1.1: Primary chemoreceptors of *E. coli* O157:H7.

Chemoreceptor	Senses	Comparison to E. coli K-12
Tar	Apartate, Glutamate, Methionine, Ni^{2+}	99.63% Identical
Tsr	Serine, Threonine, Glycine	98.71% Identical
Tap	Peptides	98.87% Identical
Trg	Ribose, Galactose	98.71% Identical
Aer	Oxygen	99.40% Identical

In this study, we used the non-pathogenic lab strain *E. coli* RP437 as a model system for investigating the chemotaxis of EHEC towards GI tract molecules. This is a valid approach as both non-pathogenic *E. coli* and EHEC possess the same five chemoreceptors with a high degree of sequence homology. **Table 1.1** shows the 5 chemoreceptors present in EHEC and *E. coli* K12 strains, the canonical chemoeffectors that are sensed using these receptors, and the homology. Second, isogenic receptor knock-out mutants are available for *E. coli* RP437. Lastly, using the non-pathogenic strain is a safer alternative to using the pathogenic bacterium.

Conventional methods of studying chemotaxis such as swarm plates and capillary assays, although widely used, have a number of drawbacks that limit their use in chemotaxis investigations. These include variability in the output (cell counts in the capillary assay varies significantly), unsuitability for studying repellent taxis (capillary assay cannot detect repulsion and only reports lack of attraction), temporally changing concentration gradients (i.e., the chemoeffector continually diffuses out from the source), and requirement for metabolizable chemoeffectors (e.g., movement towards sugars in swarm plates). Microfluidic chemotaxis models are uniquely suited to address these problems and facilitate chemotaxis investigations. For example, the flow-based microfluidic chemotaxis model developed in this study allows generation of temporally and spatially stable concentration gradients of chemoeffectors, is equally applicable for attractants and repellents, and is more sensitive than conventional methods. Furthermore, the concentration gradient altered to investigate the effect of different profiles – either strength of the gradient and/or shape of the gradient – on chemotaxis.

This advantage is also illustrated in Chapter V where we have utilized the flow-based microfluidic model to conclusively prove that the nickel binding, NikA, and nickel transport, NikB and NikC, systems are not necessary for chemotaxis away from Ni^{2+} gradients. This is consistent with conclusions reached using isothermal calorimtery by Ikuro Kawagishi and co-workers (Hosei University) in a concurrent study, and disprove previous work stating that the Nik genes were responsible for nickel taxis (40). To our knowledge, our work represents the first flow-based chemotaxis system where bacteria are exposed to a temporally and spatially-stable concentration gradient of chemoeffectors, and has attracted significant attention in the bacterial chemotaxis community.

The second area of research focuses on investigating biofilm formation and development after surface colonization. Biofilm development is controlled by numerous cellular and environmental factors. These factors include quorum sensing (QS) molecules, environmental chemicals and nutrients, environmental stress, and bacterial fighting agents released by a host in response to infection. Studies have shown that QS is necessary for the development and maturation of a biofilm (101).

Biofilm formation has been conventionally studied in batch and flow cell systems, however, these systems are not ideal for investigating spatio-temporal aspects of biofilm formation. Microfluidic devices are important as they offer two major advantages – (i) spatial and temporal control of the biofilm microenvironment through control of flow and micropatterning, and (ii) advantages of scale. The former arises from the fact that biofilm formation and maturation is spatio-temporally regulated (i.e.,

different bacteria colonize at different times and locations driven by metabolic and functional cooperation); hence, there is a need to be able to regulate the biofilm environment. The latter is important for screening biofilm inhibitors, as microfluidic reactors typically have nanoliter volumes and are much smaller than other flow cell systems.

As a first step towards characterizing biofilm formation in microfluidic devices, we (in collaboration with Prof. Harihara Baskaran at Case Western Reserve University) developed a mathematical model to describe biofilm formation and quorum sensing in closed channels. In macroscale systems, the dimensions of the system are very large compared to the dimensions of the biofilm. However in microfluidic systems, the height and volume of the system can be of the same magnitude of that of the biofilm. As the biofilm develops and grows, the cross sectional area of the system open for fluid flow decreases. This increases the velocities and in turn, the shear stress applied to the biofilm surface. This increase in shear stress increases the amount of bacteria that detach from the biofilm; thus, limiting the size of the biofilm. Our work is novel because it is the first model to take into consideration the change in the area available for flow as the biofilm increases.

The specific objectives were to:

- Develop new techniques and microfluidic devices for studying bacterial chemotaxis.
    - Two Fluorophore Chemotaxis Agarose Plug Assay
    - Microplug device
    - Microflow gradient device
- Study chemotactic response of *E. coli* RP437 to gradients of molecules found in the gastrointestinal tract (e.g., norepinephrine, indole, AI-2).
- Study the chemotactic response to a gradient of the repellent Ni^{2+} by *E. coli* RP437 WT and isogenic mutants for genes involved in Ni2+ binding and transport.
- Develop a microfluidic model for investigating biofilm growth and its relationship to QS.

CHAPTER II

LITERATURE REVIEW*

2.1 Origins of Bacterial Motility and Chemotaxis Studies

In 1676, Anton van Leeuwenhoek made the first observations of bacterial motility during the early stages of microbiology. In the late 19th century, Wilhelm Pfeffer in Tuebingen described how bacteria migrate towards nutrients. Chemotaxis studies progressed little until the1960s, when Julius Adler began to systematically study the chemotactic behavior of *Escherichia coli*. Adler's earliest published work on chemotaxis (3) set off a flurry of interest. Adler described how bacteria detect molecules without importing or metabolizing them (63). He established that there must be specific cell-surface receptors that are responsible for controlling migration. Edward Purcell has described bacteria living at low Reynolds number, where inertia effects are miniscule compared to the effects of viscosity (110).

2.2 How Bacteria Move During Chemotaxis

Bacterial movement is random as Brownian motion is continuously reorienting bacteria and they cannot out-swim diffusion. This causes the bacteria to have a random walk in the absence of a gradient. The role of diffusion on bacterial movement is

---

*Reprinted in part with permission from the book chapter "Microfluidic Techniques for the Analysis of Bacterial Chemotaxis" by Derek L. Englert, Arul Jayaraman, and Michael D. Manson, in Chemotaxis, Methods and Protocols, In Methods in Molecular Biology, Vol 571, 2009 Humana Press.

summarized in Berg's *Random Walks in Biology* (18). The numerous ways in which bacteria move through liquids or across wetted surfaces has been recently reviewed (68).

Many bacteria move by rotating their flagella to propel themselves forward or change direction. Flagellar rotation is driven by an inward ion current across the cell membrane through an embedded motor. In many bacteria, the rotation is bidirectional, clockwise (CW) or counterclockwise (CCW). By reversing the direction of rotation, the bacteria can tumble which causes a change in direction. In other bacteria, they change direction by varying the rotation speed of the flagella (11) which allows the bacteria to be reoriented by Brownian motion. Because of their small size, Brownian motion continually rotates the bacteria's trajectory so that they are unable to swim in a straight line.

As most bacteria are too small to detect concentration differences across their bodies, the Berg (25) and Koshland (90) laboratories proposed that bacteria overcome this by continuously monitoring concentrations and comparing them to the concentrations detected a few seconds earlier. This comparison requires a running short-term memory, where the newest concentration is added to the stack and the oldest is removed. In this way, the memory is continuously adapted to ambient stimulus levels so that future changes can be detected (79, 118).

Based on these concentration gradients, the bacteria will switch the flagellar motor between CCW and CW rotation. The CheY protein is responsible for regulating the flagellar motor's directional rotation. The motor responds to intracellular levels of phosphorylated CheY. The phospho-CheY level is constantly adjusted to prevent

directional reorientation when the cells are moving in a favorable direction. This causes a bias in the random walk. The net movement in the concentration gradient is typically twenty percent or less of the swimming velocity. If the swimming velocity is 50µm/sec, then the net migration would be 10µm/sec. Bacteria can swim anywhere from a few to a hundred body lengths per second. In the environment, the ability to migrate allows the bacteria to reach localized sources of attractants while avoiding sources of repellents.

2.3 Established Methods for Assaying Bacterial Chemotaxis

The overall simplicity of bacterial tactic behavior makes it possible to use a variety of methods to study it. Some of these methods monitor the movement of cell populations and others focus on individual cells. The temporal sensing mechanism utilized by bacteria makes it possible to study cells without net movement in a gradient like the tethered cell assay. This allows direct monitoring of cells while delivering stimuli and does not require expensive equipment.

2.3.1 Swim and Swarm Plates

When studying chemoeffectors that can be metabolized, agar plate assays can be used. Polymerized agar consists of extended polymer chains infused with water-filled channels. At low agar concentrations (0.25 to 0.4%) these channels are large enough that the bacteria can swim through them. In the absence of a chemoeffector, cells spread out evenly in all directions through the agar matrix from the point of inoculation. Since the cells are growing, an expanding colony forms within the agar. Smooth swimming

mutant cells get trapped by the many dead ends in the agar matrix (140). Just like the smooth swimming only mutants, the tumble only mutant colonies cannot expand significantly faster than those of non-motile cells.

As the colony grows, it metabolizes any attractants it can which causes the formation of a spatial concentration gradient in the agar. As a result, the cells migrate outward towards higher concentrations. Typically, a sharp ring can be seen where the cells congregate in the steepest part of the gradient. When an attractant can only be metabolized aerobically, the ring will form on the surface. For bacteria that perform aerotaxis (115), the cells may form a sharp ring as they follow oxygen gradients at the bottom of the agar layer. Chemotactic rings can easily be documented photographically by using a "bucket of light" (102).

A variation on the swim plate method is the swarm assay (59). If the agar is more solid (0.5% to 0.7% for *E. coli* and *Salmonella enterica*), cells can swim through the aqueous layer that forms on the agar surface. Swarming cells typically produce more, longer flagella. Even though an intact chemotaxis system is needed for swarming, it is not necessarily a chemotactic behavior. Some bacteria swarm using lateral flagella that are different from the polar flagellum that used for swimming in their planktonic state.

2.3.2 Capillary Assays

Pfeffer first described the capillary assay in the 1880's. In the 1970's, Adler standardized and popularized the assay (4). Many fundamental chemotaxis discoveries,

like specific cell-surface chemoreceptors (63) and the identification of attractant amino acids, sugars, and other compounds (6, 96), were made using this assay.

Chambers on the order of 1 cm^2 and 1 mm in height (the pond) are loaded with a suspension of highly motile bacteria in chemotaxis buffer. A 1 µm capillary is sealed at one end and filled with several mm of an attractant at the desired concentration. The capillary is then inserted into the chamber and incubated at the desired temperature for 30 to 45 minutes. The chemoeffector in the capillary will diffuse out into the well creating a gradient that the can be sensed by the bacteria around the opening of the capillary. The bacteria will then migrate into the capillary if the chemoeffector is an attractant. The capillary is then removed and the contents placed into dilution buffer. Dilutions are plated on nutrient agar and colonies are counted the next day. The colony counts allow the number of cells entering the capillary to be calculated. These numbers can then be used to compare the chemotactic response to various compounds. By filling the capillary with a dye, the gradient can be visualized and the profile calculated as a function of (52).

Repellents can be assayed the same way but would compare the decrease in the number of cells that enter capillaries filled with repellents to capillaries filled just with buffer. Alternatively, repellents could be added to the pond and the capillary filled with buffer (repellent-in-pond assay) (124). Although the capillary assay can be used for repellents, the results are not nearly as sensitive as those for repellents. Therefore, it is not ideal for use wit repellents. By placing a chemoeffector in the pond, competition between chemoeffectors can be assessed (5, 53). A high throughput method for running

parallel assays has been developed (13) that uses a multi-well microplate and a matching adapter that holds multiple capillaries.

2.3.3. Monitoring Movement of Bacteria in Stable Gradients

In the previous methods, the concentration gradients were changing with time, either by metabolism or diffusion. Therefore, a stable gradient device was needed. Some early work in which the migration of bacterial populations was quantified utilized glycerol-stabilized spatial gradients, as glycerol is inert as a chemoeffector at the concentrations used (0.3 – 0.5%) (38). By mixing attractants or repellents with the glycerol solutions during the formation of the gradients, virtually any profile of attractant or repellent concentrations can be achieved. The bacteria's position was determined by measuring light scattering along the chamber. Initially, the bacteria are uniformly distributed. They become depleted in some regions of the gradient and accumulate in others over time. The bacteria's position is measured over time and the response kinetics can be determined. A recent variant involves placing bacteria in a static, nonflowing chamber separated by a membrane from a flowing source of a chemoeffector and a flowing sink (41). This technique produces linear gradients and allows for individual bacteria to be tracked.

2.3.4 Tracking Individual Swimming Bacteria

Howard Berg discovered the random 3-D walk and biased random walk by studying *E. coli* using an automated tracking device (16, 21). Berg's device was a

mechanical stage that was controlled in 3 dimensions by DC servos. The electronic detector was able to control the stage so that the bacteria remained in center and focused. The stage axis coordinates could be recorded over time and then plotted in order to show the path of the bacteria (19).

Motion analysis systems are now commercially available and have been used to track cells (8). The measured parameter of motility is the rcd, the rate of change of direction, in degrees, per unit time. By tracking the bacteria in two-dimensions, periods of smooth swimming and reorientation can be observed. The technique can be used to determine baseline behavior and measure responses to added chemicals or light. A major development was the development of caged compounds that are released by flash photolysis (75). Depending on the size of the beam, impulse or step responses can be measured.

2.3.5 Tethered Cell Assay

For every force, there is an equal and opposite reaction. So when the flagella is rotated, the bacteria's body is counter-rotated. By holding a single flagellum, a CCW-spinning flagellum would turn the cell body CW, and a CW-spinning flagellum would turn the cell body CCW. When viewed from above, attractants lead to periods of CW-only rotation and repellents lead to briefer periods of CCW-only rotation. In *E. coli*, a CCW rotation corresponds to straight swimming "runs" which corresponds to favorable conditions, and CW rotation causes tumbles until proper reorientation for a more favorable direction. When heading up an attractant gradient, the flagella would be

rotating CCW. For a repellent, the bacteria would increase the CW rotations to increase the tumbles until it was heading down the repellent gradient.

Tethered cells are typically attached to a surface with antibodies attached to flagellar filaments (116). The antibodies bind specifically to the flagella and non-specifically to the glass slide or coverslip. By mechanically sheering the flagella to short stubs, the chance of binding multiple flagella is greatly reduced (22). Shearing can be done by passing cells back and forth rapidly between two syringes that are connected via small-gauge needles and thin tubing.

The ratio of total time spent in CW or CCW rotation give a quantitative measure of the cell's run-tumble bias. To prepare the system for imaging, a glass slide is evenly covered in a suspension of cells and antibodies. The bacteria are then allowed to settle onto the glass for 30 minutes. A good preparation yields several dozen rotating cells per image area at 1,000 X magnification. An alternative to using antibodies is to use a strain of an *E. coli* that produces "sticky" filaments because of the $fliC^{ST}$ mutation (81, 114). Another method is to use an antibody-coated latex bead. The bead then attaches to the flagellum of a immobilized bacteria. The latex bead allows the rotation of the flagellum to be visualized (31, 45).

A number of recorded videos can be saved and then batch analyzed, either by an observer with a stopwatch or by an automated system (17) or a motion analysis device (75). If the tethered cells are in a flow cell (20), responses to the addition or removal of attractants and repellents can also be monitored. Even modest changes of rotational bias in response to shallow temporal gradients can be measured (23).

2.3.6 Microfluidic Assays

The unique features of microfluidics, such as small volume and large surface-to-volume ratio, laminar flow, high throughput, and compact system size for fast and accurate analysis of samples, are increasingly useful in biology. The studies that microfluidic techniques enable were previously impossible or very challenging to perform. One example is the generation of gradients of signaling molecules in microfluidic channels for investigating bacterial and eukaryotic cell chemotaxis. These devices generate concentration gradients using laminar flow phenomena in microfluidic channels to split and recombine liquids coming into the channel from multiple outlets (27, 120, 129). Such microfluidic systems can dilute or mix liquids into linear or logarithmic concentration gradients. The sampling of the gradients generated is simply determined by splitting the output from the main channel into multiple outlets. While microfluidic gradient generators have been extensively used for investigating neutrophil migration, neural stem-cell differentiation, and hepatocyte gene-expression profiling (74), they have not been applied to microbiology studies.

Mao et al. (93) were the first to investigate bacterial taxis in a microfluidic flow cell, in which a concentration gradient was formed by diffusion of two parallel streams. These authors showed that a significant chemotactic response to L-aspartate can be obtained with concentrations as low as 3.2 nM. In addition, it was also observed that the same molecule (L-leucine) can be sensed as an attractant by Tar and as a repellent by Tsr. Different variations of this device, such as the three-channel microfluidic device where a linear gradient is generated in the absence of flow, have been developed for

investigating chemotaxis. Several microfluidic devices for investigating bacterial chemotaxis have been developed recently. One approach generates stable 2D and 3D concentration gradients using a microfluidic ladder chamber (113). Another involves using a T-shaped channel device to investigate chemotaxis perpendicular to the direction of fluid flow (83). The power of microfluidics is clearly evident from a recent demonstration of bacterial migration in response to nutrient patches with environmentally realistic dimensions and dynamics (119). These studies clearly show the potential of microfluidic approaches for investigating bacterial chemotaxis, especially in response to concentration gradients of different strengths, and for responses to two opposing gradients. See **Table 2.1** for a summary of the advantages and disadvantages of the methods.

2.4 Mathematical Modeling of Biofilm Formation

One current method for studying biofilm growth involves monitoring biofilm formation in batch cultures using multiwell plates. However, this does not accurately reflect the *in vivo* environment as there is continuous flow of fluids. For example, the luminal contents are constantly flowing in the GI tract. Continuous flow systems have also been used for biofilm studies (86). Continuous flow cell culture systems are a powerful approach that can be used to monitor real-time QS molecule expression in biofilms (56). To date, the majority of these approaches are macroscopic and involve the use of large flow cells where rigorous control of the spatio-temporal microenvironment

Table 2.1: Advantages and disadvantages of chemotaxis assays.

Advantages	Disadvantages
Chemotactic Ring Formation in Semi-solid Agar	
Easy to prepare Requires minimal equipment Strains can be compared directly Mutants and revertants easily identified	Requires metabolizable chemoeffector Hard to quantify because of metabolism Adaptation masks differences in response Obscures differences among individual cells Repellent taxis difficult to observe
Capillary Assays	
Gives quantitative data Requires minimal equipment Gradients created by diffusion, not metabolism Many compounds can be tested in parallel Competition between chemoeffectors can be studied	Time-consuming to prepare and score Uses lots of Petri dishes and media Not ideal for studying repellent taxis Obscures differences among individual cells
Monitoring Movement of Bacteria in Stable Gradients	
Gradients are constant over time Gradients of any profile can be created Kinetics of the response can be followed Large number of cells gives good population data Pseudotaxis and aerotaxis not complications Can use gaseous chemoeffectors (e.g., oxygen)	Only one strain and condition monitored per assay Requires significant set-up time and equipment Obscures differences among individual cells
Tracking Individual Swimming Bacteria	
The behavior of single cells can be followed Can couple with photolysis of caged compounds Impulse and step responses can be measured	The 3-D tracker is a custom-made, unique device Motion analysis records only 2-D behavior Motion analysis only measures run-tumble bias Motion analysis systems are relatively expensive Time-consuming to collect data for statistical tests
Tethered Cell Assay	
Simple to carry out CW and CCW intervals determinable for cells Quantitative measure of performance of one flagellum With flow cell can record responses to step gradients Can record responses to attractants and repellents Same cells can be exposed to multiple stimuli Can look at behavior of non-chemotactic mutants	Chemotactic migration not actually measured Flow cells relatively hard to make and operate Need good microscope and video recorder Only convenient to use with large step stimuli Only some types of flagellation allow tethering Usually need specific anti-flagellar sera
Microfluidic Assays	
Easy to fabricate and operate High degree of reproducibility Give quantitative data Gradients can be created over any concentration range High throughput	Requires access to microfabrication facilities May not work for all bacteria, as current application requires presence of GFP plasmid Cannot be used for bacteria with low motility

around the biofilm is difficult. Microfluidic techniques however, enable precise control of biofilm microenvironment, and hence are ideal for investigating QS and biofilm formation.

Mathematical models of biofilms can be used to obtain insights on the effect of various factors on QS and biofilm development. Such models can also minimize the number of experiments needed to investigate the biological process. Biofilm growth is regulated by numerous environmental factors. It was suggested by van Loosdrecht et al. (125, 126) that one such factor is detachment, as it is the primary process to balance bacterial growth. Picioreanu et al. studied and modeled biofilm growth and detachment based on nutrient growth and shear forces due to flow rate (108). It was found that detachment depended not only on flow rates, but how quickly the biofilm was able to grow based on the availability of nutrients. After the recognition of the role of quorum sensing in biofilm development, various models were developed that looked at the effect flow has on QS concentrations inside biofilms (67, 77). These models focused on the transport of nutrients and oxygen to and QS molecules away from the biofilm. Current models work well for large continuous flow cell systems but break down when applied to the microenvironment inside microfluidic devices. In these micro flow cells, the growth of the biofilm affects its hydrodynamic environment. With an increase in biofilm thickness, the cross sectional area available for bulk fluid flow is decreased.

CHAPTER III

MICROFLUIDIC CHEMOTAXIS METHOD DEVELOPMENT*

3.1 Overview

Bacteria migrate in chemical gradients by sensing the concentration of chemoeffector molecules using cell-surface receptors (63, 90). By constantly monitoring the concentration and comparing it to the concentration detected a few seconds earlier, bacteria make "decisions" on the net direction of movement (i.e., either up attractant or down repellent gradients) (25, 90). A more complex decision-making process arises in natural bacterial habitats in which bacteria are likely to encounter multiple chemoeffectors with potentially opposing effects.

Classical methods for investigating bacterial chemotaxis in the laboratory include the following; formation of chemotactic rings in semi-solid agar, plug-in-pond assays, and capillary assays. Although widely used, these methods have significant disadvantages. The formation of chemotactic rings in semi-solid agar requires that the chemoeffector being tested be metabolizable, and it is impossible to use for repellents. The plug-in-pond assay requires a high concentration of chemoeffector in the plug to establish a gradient, and both it and the capillary assay generate gradients that change

---

*Reprinted in part with permission from "Differential Effects of Epinephrine, Norepinephrine, and Indole on *Escherichia coli* O157:H7 Chemotaxis, Colonization, and Gene Expression" by Tarun Bansal, Derek Englert, Jintae Lee, Manjunath Hegde, Thomas K. Wood, and Arul Jayaraman, 2007, Infection and Immunity 75: 4597-4607, Copyright by American Society for Microbiology.

over time. These methods also are not ideal for quantifying subtle differences in migration rates or for looking at responses to complex gradients consisting of multiple chemoeffectors.

Some of these issues have been addressed through the use of microfluidics-based chemotaxis models. Microfluidic methods have tremendous potential for chemotaxis studies because they can be used to measure chemotaxis quantitatively. In addition, they work equally well for attractants and repellents, and they can generate highly stable gradients over any user-defined concentration range.

This chapter describes the development of three new chemotaxis models that addresses the drawbacks described above for swarm plate and capillary assays. The first method – the two fluorophore chemotaxis agarose (TFCA) plug assay - was developed as a rapid screening method for investigating chemotaxis prior to performing complicated experiments in microfluidic devices. For example, it is important to determine the effective concentration range and exposure time for different chemoeffectors so that these conditions can form the initial testing point in the microfluidic device. As an improvement to the TCFA plug method, we developed a simple static microfluidic chemotaxis device – the μPlug - that is suitable for long-term investigation of chemotaxis. . Lastly, we developed a flow-based microfluidic device (μFlow) for quantitatively investigating bacterial chemotaxis in response to stable concentration gradients.

3.2 Two Fluorophore Chemotaxis Agarose Plug Assay

The TFCA plug assay is based on the agarose-in-plug bridge method developed by Yu and Alam (146). Yu's assay consisted of an agarose plug containing chemoeffector sandwiched between a glass slide and a glass coverslip that was raised by another set of coverslips. Although simple and easy to use, the assay developed by Yu and Alam suffers from a significant drawback in that the extent of migration is often affected by movement of the bulk liquid surrounding the agarose plug. This results in movement of bacteria and makes it difficult to differentiate between cells moving due to chemotaxis and those moving due to the movement of fluid. In order to partition these two phenomena, we used differential labeling of live and dead bacteria and introduced them both into the chamber. If fluid flow effects are dominant, one would expect to observe movement of both live and dead cells. On the other hand, if movement is due to chemotaxis, one would observe only live cells moving towards or away from the signal. *E. coli* expressing either green fluorescent protein (GFP) or red fluorescent protein (RFP) were used for these studies. GFP expression was from the plasmid pCM18 (100) while RFP expression was through plasmid pDSRedExpress (Clontech, CA). RFP expressing cells were grown overnight and then killed by exposure to 1000 μg/mL of kanamycin for 1 h).

In the agarose plug assay, a 2% low melting point agarose solution is made in chemotaxis buffer (1X PBS, 0.1 mM EDTA, 0.01 mM L-Methionine, and 10 mM DL-Lactate) containing the chemoeffector being tested is heated to 55°C. The agarose is spotted on a glass slide and sandwiched between a raised glass cover slip using double-

sided tape. This arrangement creates an agarose 'plug' between the two glass surfaces (**Figure 3.1**). The bacteria (OD ~0.7) are introduced around the plug in the chamber created by the microscope slide and the raised cover slip. As the chemoeffector being tested diffuses out of the agarose plug, it generates a radial concentration gradient around the agarose plug (**Figure 3.1**). If the bacterium being tested is attracted to the signal, it will move towards the gradient and result in the accumulation of bacteria at the agarose plug boundary. A chemoattractant will result in a green ring (from GFP expressing bacteria) next to the plug followed by an area containing fewer green cells (since the bacteria in this region have moved towards the plug). A repellent will result in an area of random dispersed red cells with fewer green cells near the plug as compared to areas farther away from the plug. Images were captured over 30 minutes at the agarose plug boundary to determine the chemotaxis response of the bacteria towards or away from the plug. **Figure 3.2** shows representative images of the plug assay for wild type *E. coli* towards an attractant, repellent, and a blank plug.

3.3 Microplug

Although the TFCA plug assay is simple to use, it has a few significant limitations. First, the seal between the glass slide and the coverslip is not permanent and any movement immediately caused disruption of the plug. Second, since the volume of liquid in the chamber between the two glass surfaces was very small (~50 μL), the cell suspension evaporated with long-term (> 10 min) imaging, which caused movement of the bulk fluid. Most importantly, the concentration gradient generated in the TFCA plug

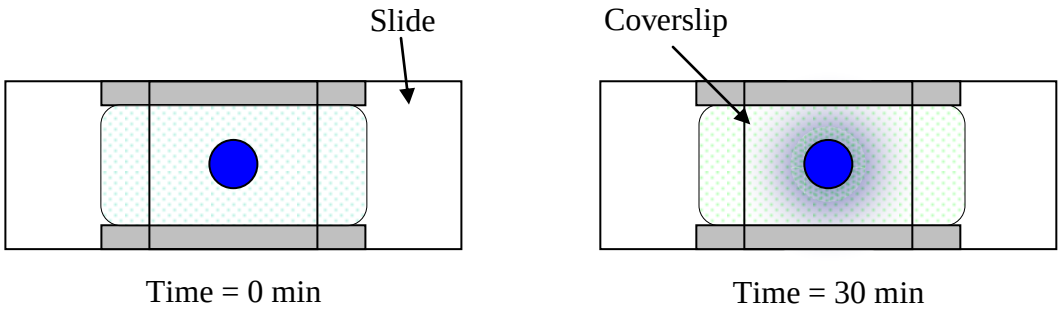

Figure 3.1: Agarose plug assay. The blue circle represents the agarose plug. After 30 minutes, the chemical has diffused outwards and concentration gradient has formed. For attractants, a green ring will form around the edge of the agarose plug.

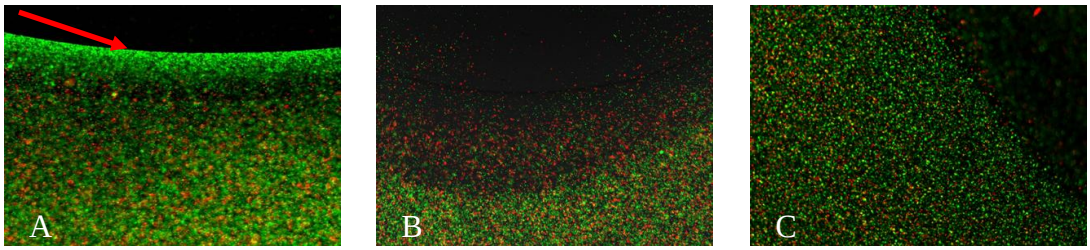

Figure 3.2: Sample images of the TFCA plug assay after 30 minutes. The dark area is the agarose plug and the red arrow indicates ring formed by attracted bacteria. Images show the response to an attractant (A), repellent (B), and blank (C).

was not stable as the chemoeffector continued to diffuse out of the plug. In other words, cells are exposed to a continually changing gradient which complicates analyzing the response to the chemoeffector being studied.

To address these issues, we developed a static microfluidic plug method. The µPlug is constructed from a top layer of molded poly-dimethylsiloxane (PDMS) permanently bonded to a glass slide. In this device, a plug of agarose containing the

chemoeffector molecule is formed in a square, microfabricated chamber (15 mm sides and ~75 microns high). Agarose is introduced through a 1.5 mm diameter hole in the middle of the chamber, and two 1.5 mm holes along the diagonal serve to introduce cells into the chamber and to provide a vent, respectively. **Figure 3.3** shows a diagram of the µPlug device. The formation of a fluoroscein concentration gradient in the µPlug device is shown in **Figure 3.4**. Fluorescein was added to the agarose plug at a concentration of 100 ng/mL, and uninoculated CB was added to the device. The device was imaged using a 5X objective every minute for 20 min. The pixel intensity was used to determine the concentration profile over time.

The migration of *E. coli* RP437 in the µPlug device in response to $NiSO_4$ and L-serine is shown in **Figure 3.5**. For a repellent, a band of GFP-labeled bacteria moves away from the plug as Ni^{2+} diffuses into the CB. For strong repellents, like Ni^{2+}, this

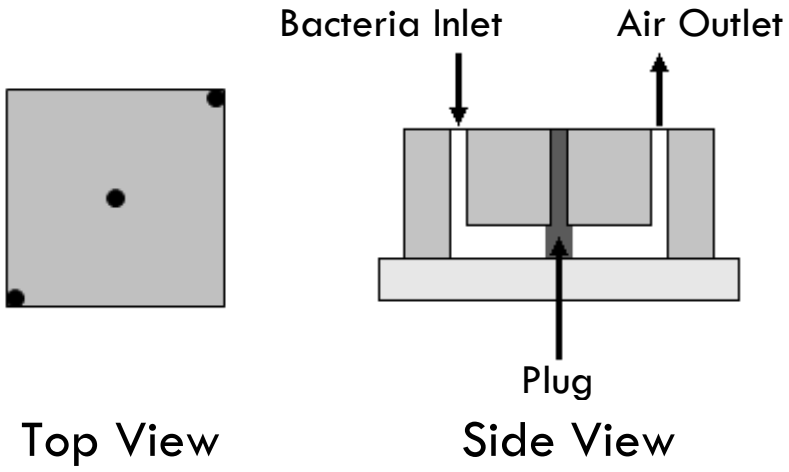

Figure 3.3:. **µPlug chemotaxis device design**. Top and side views of the µplug model are shown.

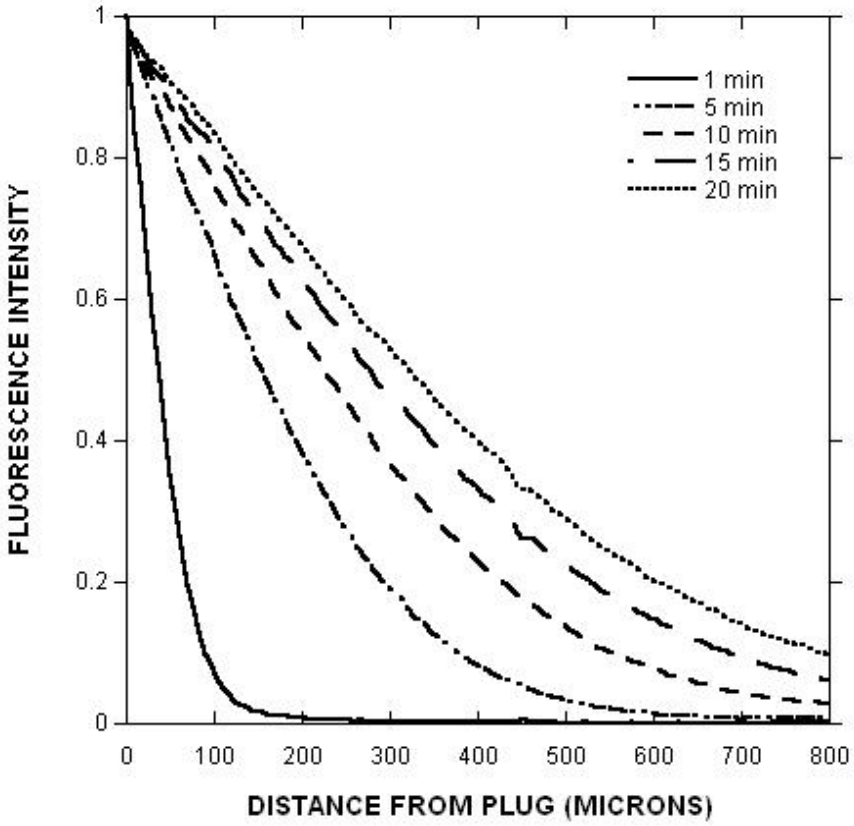

Figure 3.4: Characterization of gradient formation in the µPlug device. The diffusion of 100 ng/mL fluorescein from the µPlug was monitored using fluorescence microscopy for 30 min. Fluorescence images were quantified by image analysis and used to determine the distance to which the fluorescent dye diffuses (i.e., the concentration gradient) surrounding the plug. Figure comes from Englert et al (46).

repellent band forms and moves quickly (i.e., within ~ 15 min). For an attractant, the bacterial band becomes brighter and thicker as time progresses. Depending on the concentration and efficacy of the attractant being tested, this response can also occur rapidly.

The advantages of the µPlug method are the rapid identification of the chemotactic response to a molecule and the ability to compare the responses of two different bacteria using differential labeling (i.e., one strain expresses GFP while the

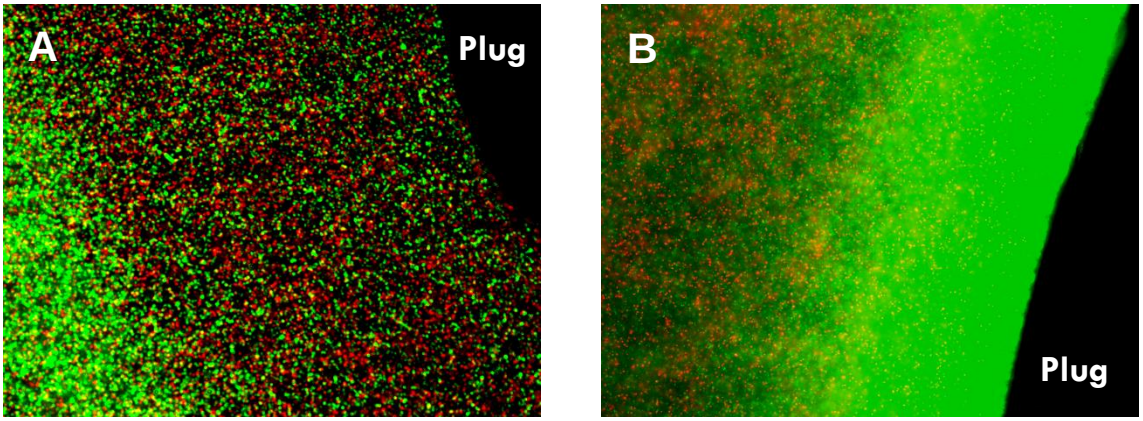

Figure 3.5: Fluorescent images of chemotaxis by *E. coli* strain RP437 in the µPlug and µFlow devices. In the µPlug device, bacteria were exposed to: (A) 225 µM $NiSO_4$; (B) 100 µM L-serine. Cells were imaged after 30 min incubation at room temperature. The location of the agarose plug containing the chemoeffector molecule is indicated. Live bacteria are green, dead bacteria are red.

other expresses RFP). In **Figure 3.5A** and **3.5B**, the RFP-labeled cells were killed by exposure to a lethal dose of kanamycin to provide a non-responsive control to monitor bulk flow, which was negligible. However, this method does not lend itself to quantitative assessment of migration. To obtain a more-quantitative characterization of chemotaxis, the flow-based microfluidic device described below was developed.

3.4 Microflow Chemotaxis Device

While the µPlug assay is a rapid test for chemotaxis attraction or repulsion to various signals, it has a few limitations. Like the TFCA, there is little control over the chemical gradient that is formed as it entirely depends on the concentration of the chemoeffector in the plug and the agarose composition (which is subject to variability). Second, the gradient strength is not constant and changes over time. Initially, the

gradient is very sharp (i.e., high concentration that only covers a small distance), but as the signal diffuses, the gradient strength decreases as the distance to which the signal has diffused increases. While these are minor limitations, the biggest drawback is that it only provides a qualitative assessment of chemotaxis and is not suited for differentiating between different levels of response. To address these issues, we developed a new microfluidic device in which the gradient strength and distance can be precisely controlled to investigate swimming motility.

The μFlow device was based on a simple flow system developed by Mao et al. (93). In that system, bacteria are introduced between two parallel streams, one containing the buffer and the other buffer with a chemoeffector. Bacteria either swim towards or away from the interface of the two streams. The μFlow device described in our prior work (47) combines a microfluidic concentration-generator with a chemotaxis observation channel to facilitate investigation of bacterial migration in response to concentration gradients of chemoeffectors. The concentration-gradient generator was inspired by the designs described in Jeon et al. (70) and Thompson et al. (123). It consists of a network of microfluidic channels (20 x 100 x 18,750 μm) fabricated in poly-dimethylsiloxane (PDMS). The network of channels generates a nearly linear concentration gradient across the width of the chemotaxis chamber from two input concentrations through a series of diffusive mixing steps. The concentration gradient is stable both throughout the chemotaxis chamber (depending upon the flow rate being used) and for the entire duration of the experiment (~ 2 h). GFP-expressing bacteria concentration gradient as opposed to the end-point concentrations in the device entering

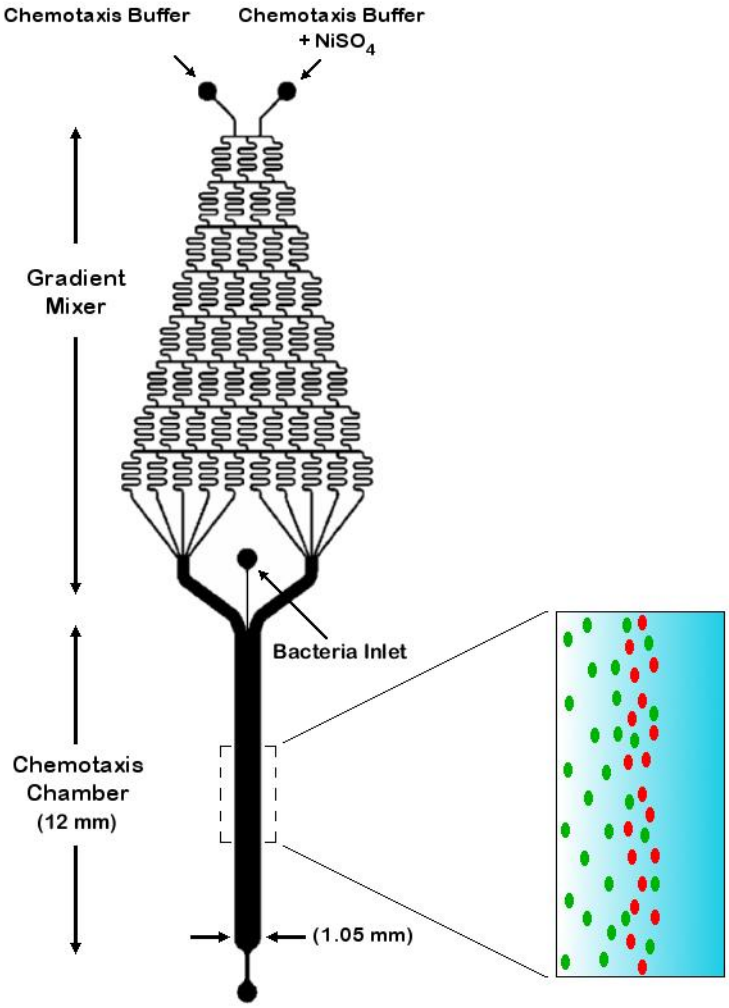

Figure 3.6: Schematic of the µFlow gradient chemotaxis device. A linear concentration gradient of signaling molecules can be generated in the microfluidic channels through diffusion. Bacteria are introduced through the middle inlet. Here is shown with a NiSO4 gradient.

the chemotaxis observation chamber immediately encounter the midpoint of the described by Mao et al (93). Depending on the flow rate used, bacteria are exposed to the gradient for different times (18 - 21 sec in our work) before imaging. Image analysis can then be used to enumerate bacterial counts at different locations across the width of the chemotaxis chamber (47). The principles underlying the µFlow device are shown schematically in **Figure 3.6**. **Figure 3.7A & 3.7B** shows fluorescence images of migration in attractant and repellent, respectively, gradients in the µFlow device.

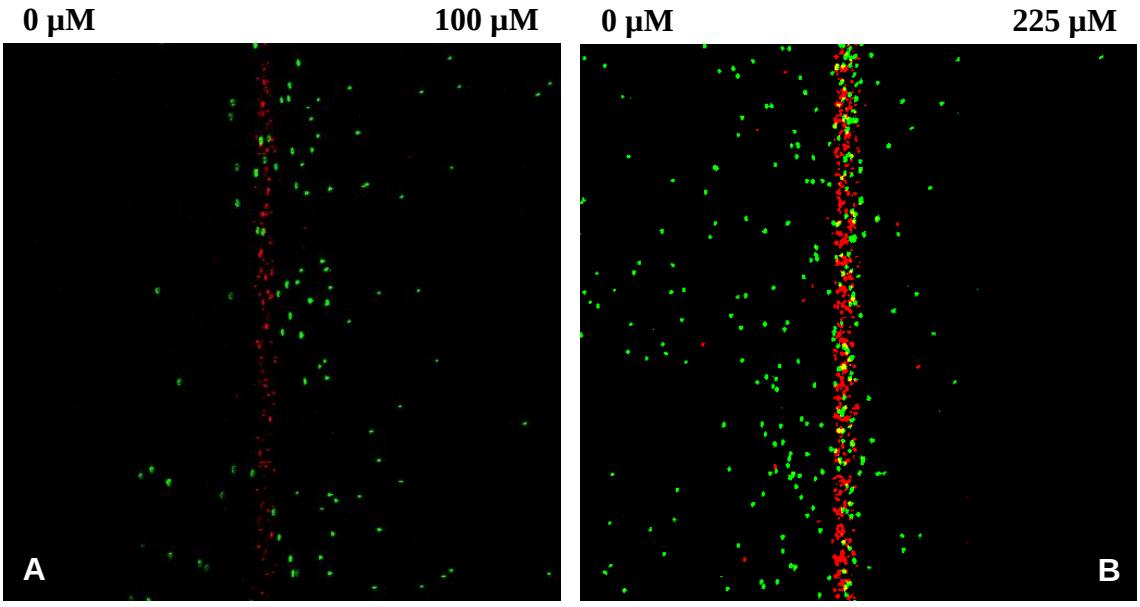

Figure 3.7: Sample µFlow device images. In the µFlow device, *E. coli* RP437 was exposed to a gradient of (A) 0-100 µM L-aspartate: (B) 0-225 µM $NiSO_4$. The migration of live bacteria towards L-aspartate or away from nickel was imaged every 2.5 sec and quantified by image analysis. Live bacteria are green, dead bacteria are red. Data shown are representative images from three independent experiments.

CHAPTER IV

EXPERIMENTAL DESIGN VARIABLES FOR THE μFLOW DEVICE*

We first demonstrated the different types of responses that can be observed in the μFlow device. **Figure 4.1A** shows the distribution profiles of dead cells in a gradient of 0-225 μM $NiSO_4$ and CV1 cells at a uniform concentration of 100 μM $NiSO_4$. As expected, the dead cells localized near the center of the chemotaxis channel and showed little lateral spreading. The position of dead cells indicates the center of the chemotaxis chamber. CV1 cells in the absence of a gradient spread out in both directions from the point of entry. **Figure 4.1B** shows the distribution profile of CV1 cells in response to gradients of attractant (0-100 μM *L*-aspartate) and repellent (0-225 μM $NiSO_4$). Since the low and high concentrations are on the left and right sides of the chemotaxis chamber (i.e., towards positions "0" and "64", respectively), the data show that CV1 migrates toward the high concentration of aspartate, whereas it moves down the gradient of $NiSO_4$. Although the distribution in the presence of the attractant is wider than that observed with the repellent (i.e., cells are observed on both sides of the chemotaxis chamber center), there is a distinct bias towards the high concentration. The four profiles in **Figures 4.1A & B** are representative responses. The calculated chemotaxis partition and migration coefficients (CPC and CMC, respectively) (See chapter V for more

---

* Submitted in part as "Investigating Bacterial Chemotaxis in Flow-based Microfluidic Devices" by Derek L. Englert, Michael D. Manson, and Arul Jayaraman, Nature Protocols (In revision).

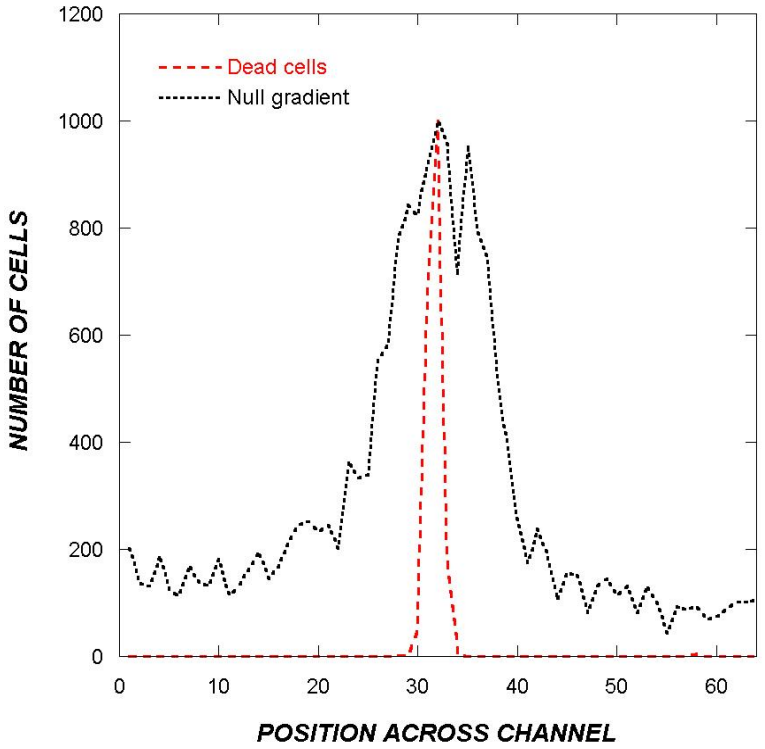

A

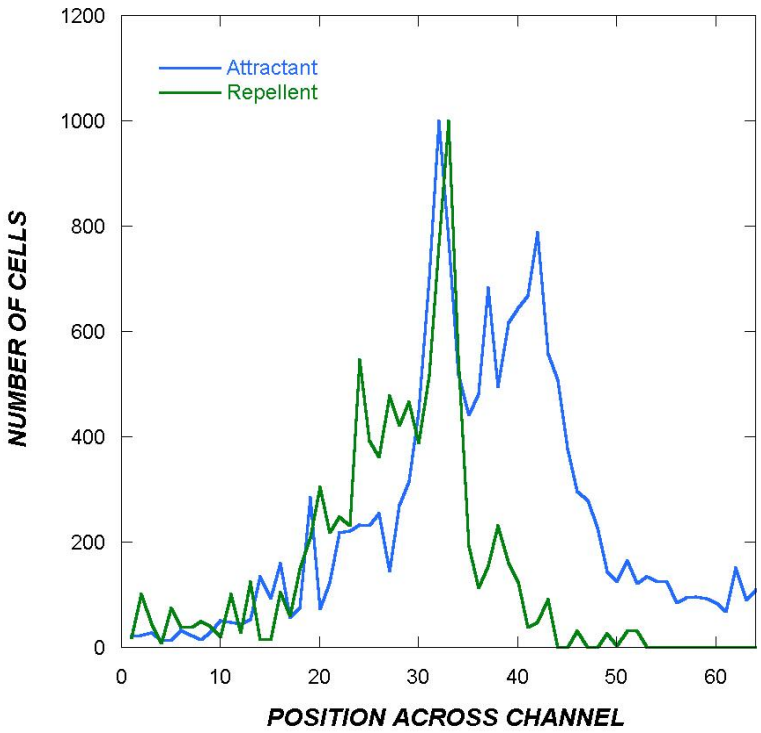

B

Figure 4.1: Quantification of migration profiles. Spatial distribution of cells in 16 micron-wide channels across the width of the chemotaxis chamber was calculated using image analysis. (A) Control profiles obtained with live CV1 cells exposed to a uniform concentration of $NiSO_4$ (50 µM) in the chemotaxis chamber and dead TG1 cells as the bulk-flow control. (B) Profiles in response to a 0 – 100 µM gradient of aspartate and a 0 – 225 µM gradient of $NiSO_4$. The low concentration is to the left, and the high concentration is to the right. The midpoint of the chamber (where bacteria enter) corresponds to channels 32-33.

details) values reflect the trends visible in the profiles. Aspartate gave positive values (0.33 and 0.13, respectively), $NiSO_4$ gave negative values (-0.34 and -0.14, respectively), and the values for the null gradient (0.04 and 0.04, respectively) were essentially zero (see rows 1-3 in **Table 4.1**).

The data shown in **Figure 4.1** were obtained with cells harvested and washed using a 0.45 μm nitrocellulose filter. **Figure 4.2** shows that, in a 0-225 mM $NiSO_4$ gradient, the distribution of cells prepared by filtration was narrower than that observed with cells prepared by low-speed (400 x *g*) centrifugation, and there was a more obvious peak of non-motile cells. The increased spreading was also reflected in the modestly increased CPC values (-0.34 for filtration and -0.50 for centrifugation; see rows 3 and 5 in **Table 4.1**) The flagellar filaments were presumably sheared to a greater extent with the filtration method. We suggest using centrifugation for most strains, because the extent of migration can be determined based on migration of a larger cell population.

The gradient steepness can also influence cell migration. Intuitively, a steeper gradient would be expected to lead to better migration. However, if the concentration of the chemoeffector is high enough to saturate its receptor an inhibitory effect may be seen. Responses of CV1 cells in two $NiSO_4$ gradients (0-100 μM and 0-225 μM) are shown in **Figure 4.3**. (Note that concentrations of Ni^{2+} up to 300 μM do not interfere with cell motility, although concentrations higher than that do.) The data show that more bacteria reach positions with lower concentrations (0 – 10) when exposed to the shallower gradient, but more bacteria are detected on the high concentration side as well.

Table 4.1: CPC/CMC data for experimental design.

Gradient strength	Chemoeffector	Preparation method	Flow rate (nL/min)	Imaging position[a]	CPC	CMC
Uniform 50 µM	$NiSO_4$	Filtration	2000	7000 µm	+0.04	+0.04
0-100 µM	*L*-aspartate	Filtration	2000	7000 µm	+0.33	+0.13
0 – 225 µM	$NiSO_4$	Filtration	2000	7000 µm	-0.34	-0.14
0 – 100 µM	$NiSO_4$	Centrifugation	2000	7000 µm	-0.47	-0.15
0 – 225 µM	$NiSO_4$	Centrifugation	2000	7000 µm	-0.50	-0.13
0 – 225 µM	$NiSO_4$	Centrifugation	1500	7000 µm	-0.36	-0.15
0 – 225 µM	$NiSO_4$	Centrifugation	1000	7000 µm	-0.23	-0.15
0 – 225 µM	$NiSO_4$	Centrifugation	2000	11500 µm	-0.44	-0.15
0 – 225 µM	$NiSO_4$	Centrifugation	1500	11500 µm	-0.34	-0.18
0 – 225 µM	$NiSO_4$	Centrifugation	1000	11500 µm	-0.22	-0.14

[a] Distance from the inlet for bacteria

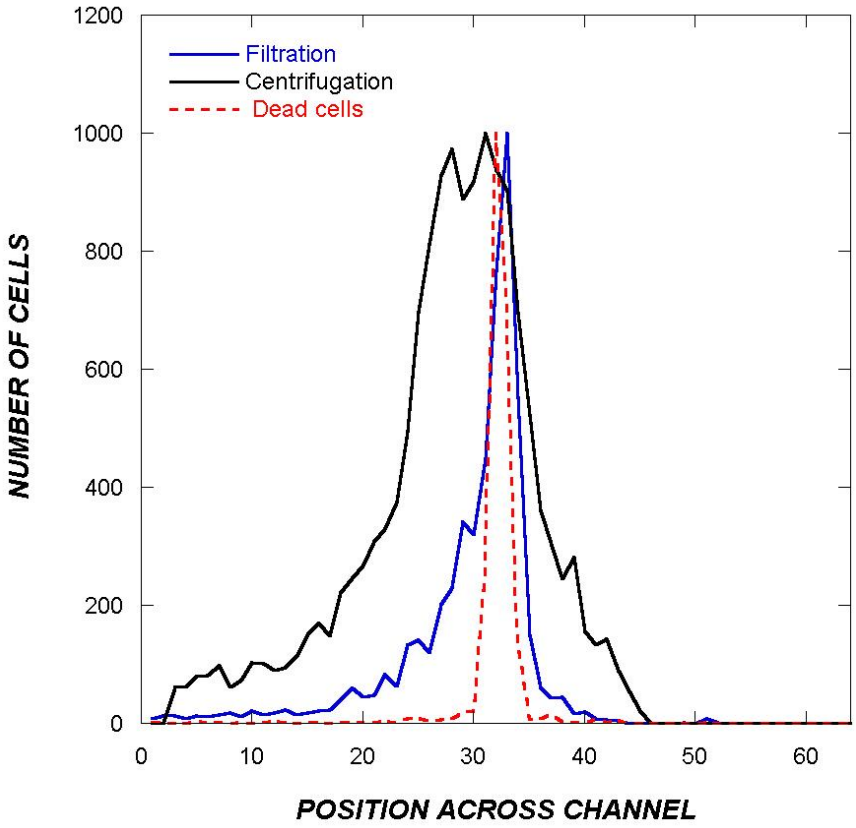

Figure 4.2: Effect of the cell preparation method on chemotaxis. Highly motile CV1 cells were prepared either by filtration or low-speed centrifugation. Chemotaxis was assayed in a gradient of 0 – 225 µM $NiSO_4$. The total flow rate (gradient + cells) was 2000 nL/min. The low concentration is to the left, and the high concentration is to the right. The midpoint of the chamber (where bacteria enter) corresponds to channels 32-33.

As a result, the CPC and CMC values for the two gradients are similar (see rows 4 and 5 in **Table 4.1**). Clearly, a range of concentrations should be tested in order to understand the full nature of the response.

A third important variable is the time during which cells are exposed to the gradient, which is a function of the flow rate through the chemotaxis chamber. **Figure 4.4A** shows repellent chemotaxis of CV1 cells in a gradient of 0 – 225 µM $NiSO_4$ at

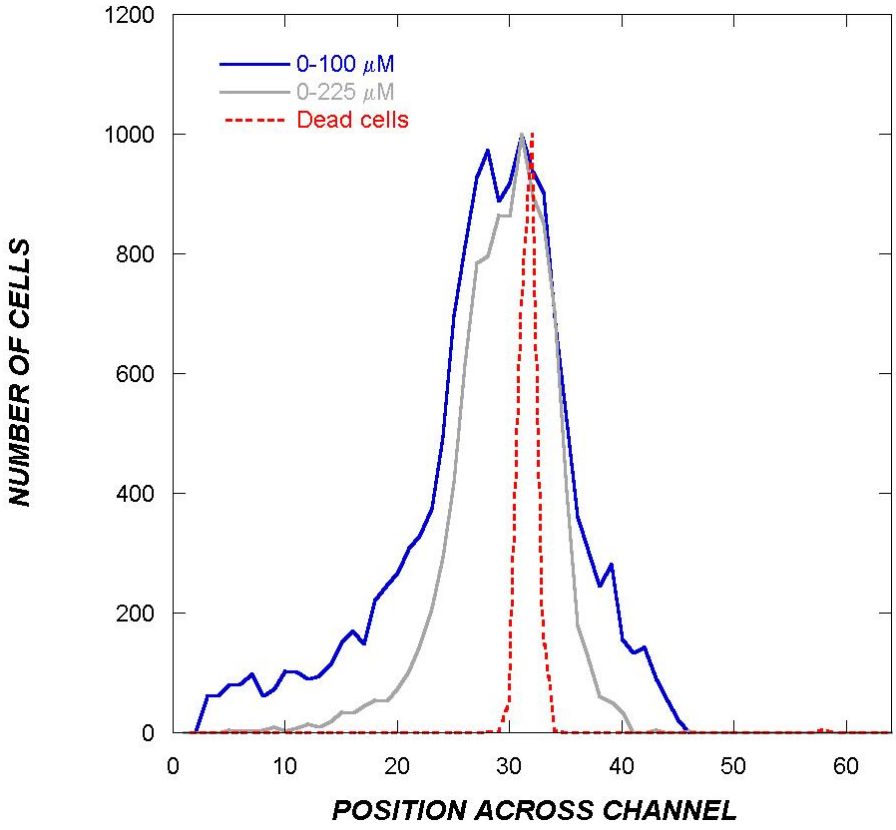

Figure 4.3: Effect of gradient strength on chemotaxis. CV1 cells were prepared by centrifugation, and chemotaxis was assayed in two $NiSO_4$ gradients (0-100 µM and 0-225 µM) at a flow rate of 2000 nL/min. The low concentration is to the left, and the high concentration is to the right. The midpoint of the chamber (where bacteria enter) corresponds to channels 32-33.

three flow rates – 1000, 1500, and 2000 nL/min. (The flow rate used for generating the data shown in **Figures 4.1 – 4.3** was 2000 nL/min). The data show that, when images are taken 7000 mm from the inlet, more cells are detected at the low concentration side of the chamber when the flow rate is 1000 nL/min (which corresponds to an exposure time to the gradient of ~ 50 sec) than when the flow rate is 2000 nL/min (exposure time to gradient of ~ 20 sec). **Figure 4.4A** also shows that more cells are detected at the higher

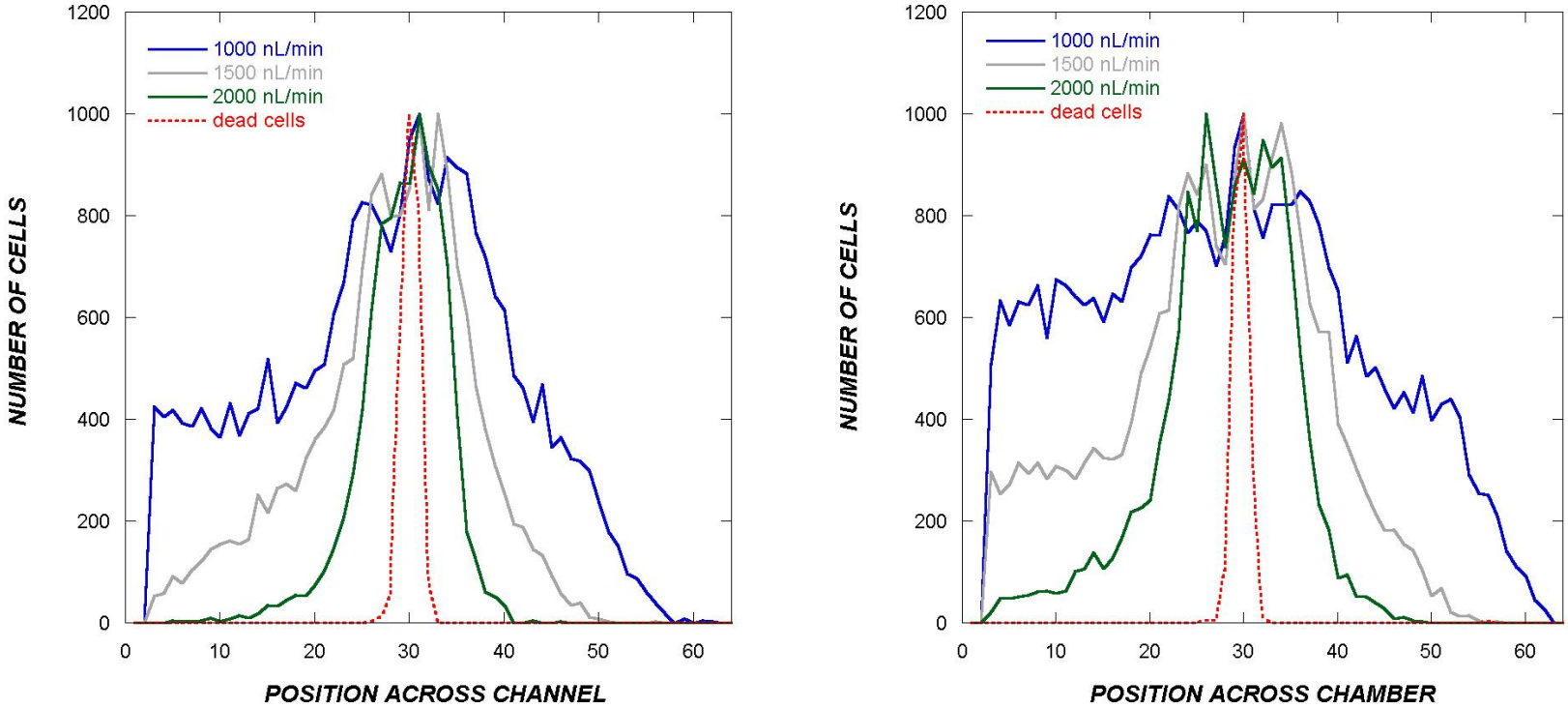

A B

Figure 4.4: Effect of flow rate on chemotaxis. CV1 cells were prepared by centrifugation, and chemotaxis was assayed in a gradient of 0-225 µM $NiSO_4$ at three flow rates – 1000, 1500, and 2000 nL/min. The dead cells correspond to a flow rate of 2000 nL/min. Cells were imaged either two-thirds down the chemotaxis chamber (A) or at the chamber outlet (B). The low concentration is to the left, and the high concentration is to the right and the midpoint of the chamber (where bacteria enter) corresponds to channels 32-33.

concentration side of the chamber when the flow rate is 1000 nL/min. Thus, there is a trade-off between obtaining the maximum possible migration and minimizing the random spreading of the bacteria. This trade-off becomes clear when the data are expressed as CPC/CMC values. The CPC value is highest at the fastest flow rate because spreading is minimized, although the CMC value remains nearly constant (**Table 4.1**, rows 5-7).

Since exposure time can also be varied by changing the position along the chamber at which images are taken, we also collected data at the outlet of the chemotaxis chamber. Similar trends in the CPC and CMC values as a function of time of exposure to the gradient were observed as with the different flow (**Table 4.1**; rows 8-10). The CPC values at the outlet are smaller than when images are taken ~ 2/3rd down the chamber because more random spreading occurs. Thus, both the extent of motility and the strength of the chemotaxis response must be considered when deciding which flow rates and imaging locations should be used.

CHAPTER V

FLOW-BASED MICROFLUIDIC DEVICE FOR QUANTIFYING BACTERIAL CHEMOTAXIS IN STABLE, COMPETING GRADIENTS*

5.1 Overview

Chemotaxis is the migration of cells in gradients of chemoeffector molecules. Although multiple, competing gradients must often coexist in nature, conventional approaches for investigating bacterial chemotaxis are suboptimal for quantifying migration in response to gradients of multiple signals. In this work, we developed a microfluidic device for generating precise and stable gradients of signaling molecules. We used the device to investigate the effects of individual and combined chemoeffector gradients on *Escherichia coli* chemotaxis. Laminar flow-based diffusive mixing was used to generate gradients, and the chemotactic responses of cells expressing green fluorescent protein (GFP) were determined using fluorescence microscopy. Quantification of the migration profiles indicated that *E. coli* was attracted to the quorum-sensing molecule autoinducer-2 (AI-2) but repelled from the stationary-phase signal indole. Cells also migrated towards higher concentrations of isatin (2-3-indole-dione), an oxidized derivative of indole. Attraction to AI-2 overcame repulsion by indole

---

*Reprinted with permission from "Flow-Based Microfluidic Device for Quantifying Bacterial Chemotaxis in Stable, Competing Gradients" by Derek L. Englert, Michael D. Manson, and Arul Jayaraman, 2009, Applied and Environmental Microbiology 75: 4557-4564, Copyright by American Society for Microbiology.

in equal, competing gradients. Our data suggest that concentration-dependent interactions between attractant and repellent signals may be an important determinants of bacterial colonization of the gut.

5.2 Introduction

Bacteria sense chemoeffectors using cell-surface receptors (63, 128). Cells constantly monitor the concentration of specific molecules, comparing the current concentration to the concentration detected a few seconds earlier. This comparison determines the net direction of movement (25, 90). Chemotaxis allows bacteria to approach sources of attractant chemicals or to avoid sources of repellent chemicals. Natural habitats for *E. coli*, such as the gastrointestinal tract, are typically heterogeneous and contain multiple chemoeffectors with potentially opposing effects. The integrated chemotactic response in such environments is thus likely to be an important factor in bacterial colonization.

Conventional approaches for investigating bacterial chemotaxis, such as the swim plate and capillary (4) assays, are not ideal for quantifying bacterial migration. Chemotactic-ring formation in semi-solid agar requires metabolizable attractants and is subject to multiple factors, and both it and the traditional capillary assay are poorly designed to investigate repellent taxis. Mao et al. (93) were the first to investigate bacterial taxis in a microfluidic flow cell. In their device, a concentration gradient is formed by diffusive mixing of two inlet streams. However, the exposure to a fully

developed gradient in this device is limited because it takes time for the gradient to develop.

Variations of this technique, such as three-channel microfluidic devices (32, 41) in which a linear gradient is generated in the absence of flow, or a T-channel device that monitors chemotaxis perpendicular to the direction of fluid flow (83), have been developed subsequently. The T-channel system has many of the limitations of the device developed by Mao et al. (93), and non-flow systems, like the capillary assay (4), suffer from lack of temporal stability of the gradients.

Here, we report a flow-based microfluidic chemotaxis device that is coupled to a gradient generator. Bacteria are exposed to precise and temporally stable concentration gradients of chemoeffectors over the length of the microfluidic channel. This device was used to quantify *E. coli* chemotaxis in response to the canonical chemoeffectors L-aspartate and Ni^{2+}. The device was also used to investigate chemotaxis toward cell-cell communication signals such as AI-2, indole, and isatin, both individually and in combination, that are likely to be present in the in vivo microenvironment in which *E. coli* is present (e.g., the human GI tract). The data obtained reinforce the idea that concentration-dependent interactions between different chemical signals could be important determinants of bacterial colonization in natural environments.

5.3 Materials and Methods

5.3.1 Bacterial Strains, Materials and Growth Media

E. coli RP437 (93) is wild type for chemotaxis, and strain RP437 *eda+ Δtar* (54) is blind to aspartate and Ni^{2+}. *E. coli* TG1 was obtained from Stratagene (La Jolla, CA). Plasmids pCM18 (58) and pDS-RedExpress (Clontech, CA) were used to express the green fluorescent protein (GFP) and the red fluorescent protein (RFP), respectively, at high, constitutive levels. Tryptone broth (TB; 10 g L^{-1} tryptone and 8 g L^{-1} NaCl) was used for liquid cultures. Erythromycin (200 µg mL^{-1}) and ampicillin (100 µg mL^{-1}) were used for plasmid selection and retention. Chemically synthesized AI-2 [(S)-4,5-dihydroxy-2,3-pentanedione] was purchased from Omm Scientific (Dallas, TX) and exists as an equilibrium mixture of different isomers; the sample contains dimethylsulfoxide (DMSO) and methanol as solvents in about a 1:1 ratio with AI-2 (information from manufacturer). Indole (99% pure) and isatin (indole-2,3-dione; 98% pure) were purchased from Fisher Scientific (Pittsburgh, PA). All other chemicals were purchased from Sigma Chemical.

5.3.2 Fabrication of the Microfluidic Device

Microfluidic devices were fabricated as previously described (76, 82, 123, 136) in the Materials Characterization Facility at Texas A&M University. Briefly, device designs were drawn in AutoCAD and used to create a high-resolution (> 3000 dpi) photolithography mask produced with a laser printer (Advanced Reproductions, North

Andover, MA). Standard photolithography techniques with SU-8 2015 (Microchem Corp, MA) were used to generate imprints of the microfluidic devices on silicon wafers. The silicone-wafer templates served as negative molds to generate the chemotaxis device in poly(dimethyl)siloxane (PDMS), using standard soft-lithography protocols (94). Channel dimensions were measured using a profilometer. Devices were fabricated by bonding the patterned PDMS slab to clean glass slides using oxygen-plasma bonding in a plasma etcher (150 mTorr, 50 W, 20 sec) to create optically transparent devices. Access ports were punched into the PDMS using a blunt 20-gauge needle.

5.3.3 Growth of Bacteria for the Chemotaxis Assay

Bacteria were prepared for chemotaxis assays as described by Mao et al. (93). Briefly, overnight cultures of bacteria were used to inoculate 10 mL samples of TB containing erythromycin to a turbidity of ~ 0.05 at 600 nm. Cultures were grown to late-exponential phase (turbidity of 0.45 at 600 nm). The appropriate chemoeffectors at the midpoint concentrations were added to the cells during growth in case induction of receptors was necessary. The cells were harvested by filtering 1-3 mL of culture through a 0.4 μm filter, and the cells on the filter were washed twice with 15 mL of chemotaxis buffer (CB; 1X phosphate-buffered saline, 0.1 mM EDTA, 0.01 mM L-methionine, and 10 mM DL-lactate). The filter paper was placed at the bottom of a 50 mL Falcon tube, and the bacteria were resuspended by gentle shaking in 1-2 mL of CB containing the midpoint concentration of chemoeffector to a turbidity of ~ 0.3 at 600 nm (~ 1.5×10^8 cells/mL). For example, for a 0-100 μM gradient of L-aspartate, CB contained 50 μM

aspartate. TG1 cells expressing RFP were killed by exposure to 1 mM kanamycin for 1 h (complete killing verified based on lack of growth on LB agar plates) and mixed with the GFP expressing RP437 cells at approximately equal densities. Assays were performed within 60 min of resuspension in CB.

5.3.4 Microfluidic Chemotaxis

The microfluidic-chemotaxis (μFlow) device (**Figure 5.1**) consists of a gradient generator and a chemotaxis-observation module. The gradient generator was inspired by the designs described in Jeon et al. (70) and Thompson et al. (123) and consists of a network of microfluidic channels (20 by 100 by 18,750 μm) that enables diffusive mixing from two inputs to generate a nearly linear concentration gradient (**Figure 5.2A**). The width of each channel exiting the gradient mixer and entering the chemotaxis observation chamber is 500 μm. The observation module comprises a channel (20 by 1050 by 11,500 μm) connected to the gradient-generator module. A secondary inlet (50 μm) was used to introduce bacteria into the observation module at the mid-point of the concentration gradient. Silicone tubing was used to introduce the bacteria and the established concentration gradient into the device. All experiments were conducted at room temperature (~ 23°C).

The flow rate in the microfluidic device was controlled using a PicoPlus programmable pump (Harvard Apparatus, Holliston, MA). The assembled device was positioned on the stage of a Leica TCS SP5 resonant-scanner confocal microscope. Two 500 μL syringes containing either CB or CB with the chemoeffector molecule being

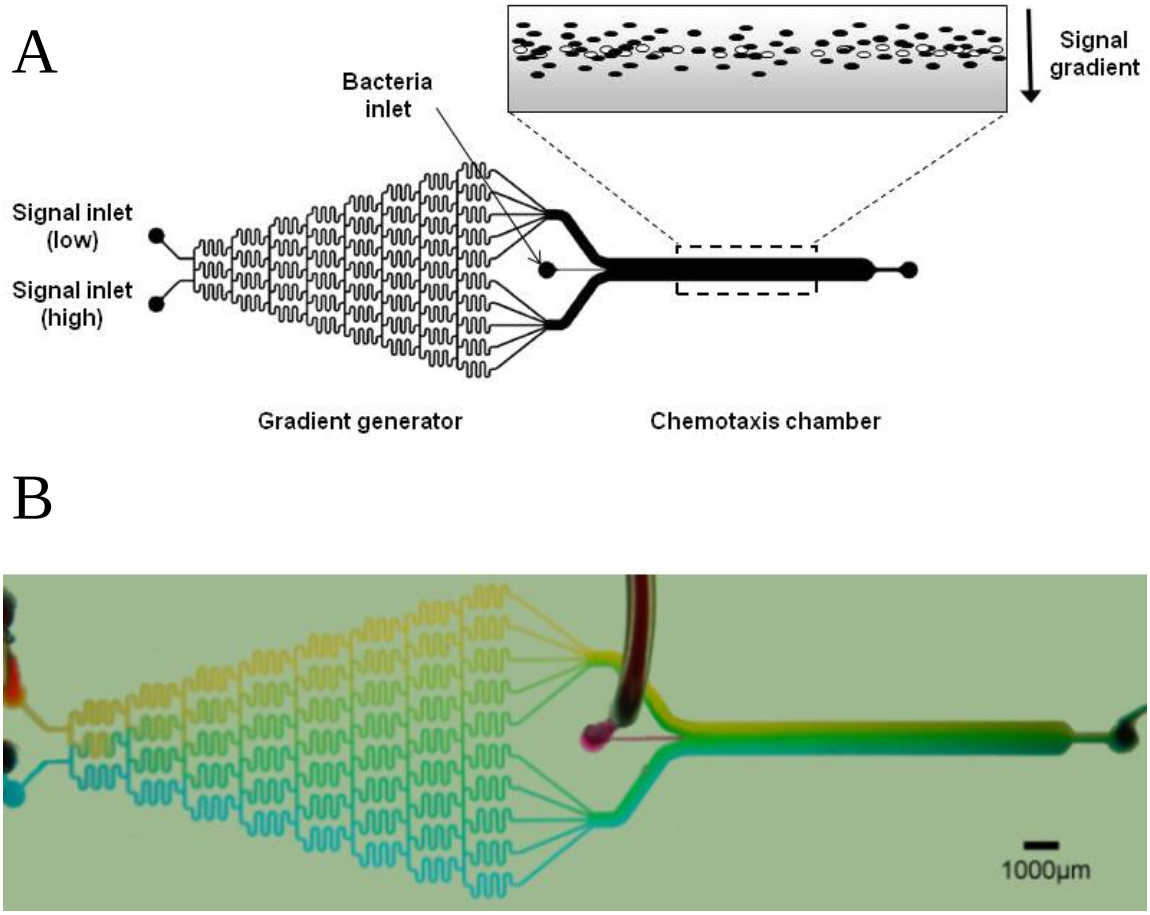

Fig 5.1: The µFlow chemotaxis device. (A) Schematic representation of the µFlow device. The device consists of a gradient-mixing module (20 by 100 by 18750 µm) and a chemotaxis-observation module (20 x 1050 x 11500 µm). The inset schematically depicts a gradient of a repellent molecule (grey) and bacteria migrating in response to it. Live bacteria are depicted as solid ovals, whereas dead bacteria are shown as open ovals. (B) Food-dye representation of gradient formation in the µFlow device, showing formation of a range of green colors from blue and yellow inputs. Scale bar indicates 1000 µm.

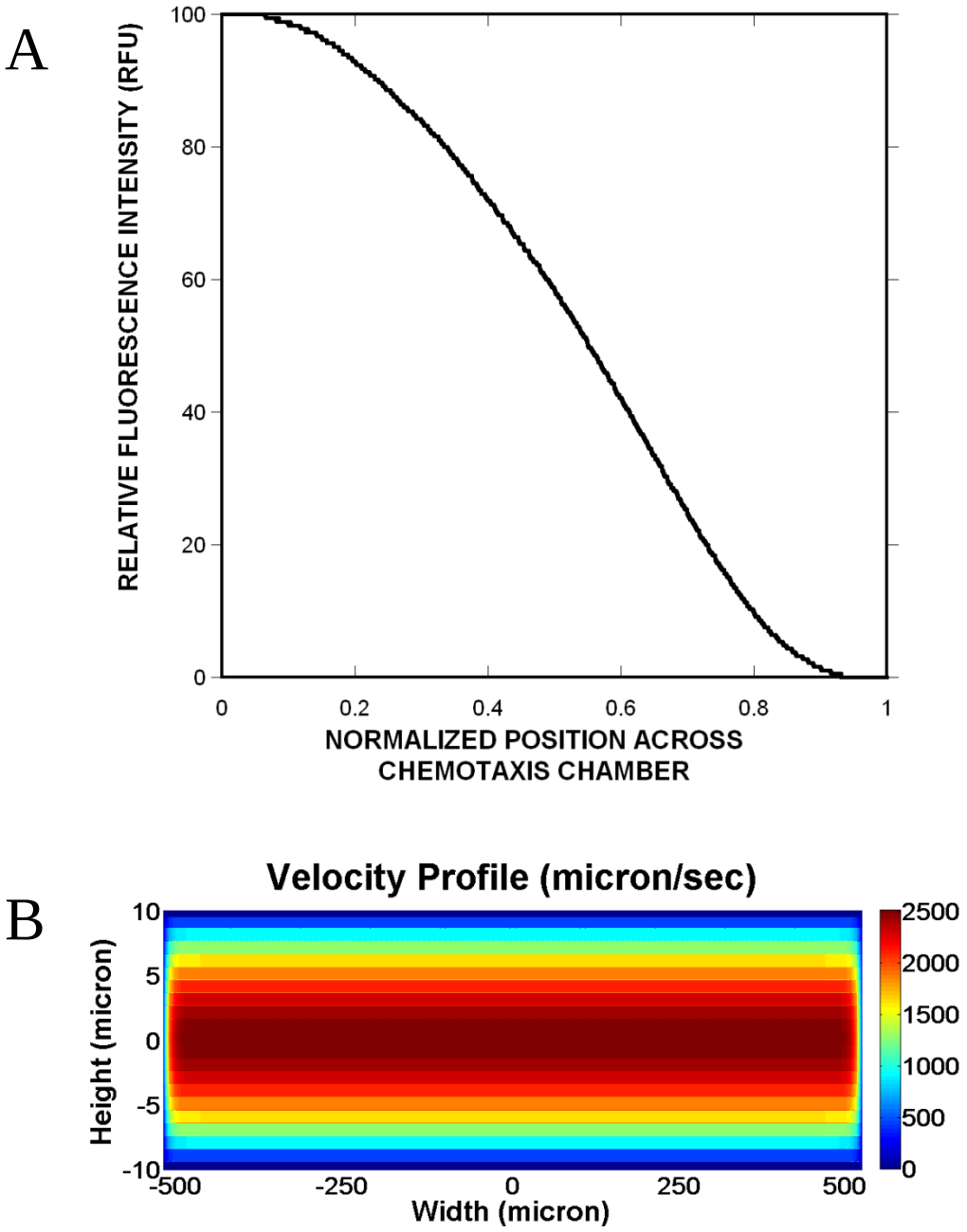

Figure 5.2: Formation of concentration gradients in the µFlow device. (A) A concentration gradient of 0 – 100 ng/mL of fluorescein isothiocyanate (FITC) was established in the µFlow device. Fluorescence images were acquired after 30 min, and the fluorescence intensity was determined at 16 µm intervals, using Matlab. (B) The velocity profile in the device along the z-direction was simulated using the equations described by Brody et al. (24).

tested were connected to the two inlets of the gradient generator module, with care being taken to avoid air bubbles. The bacteria, prepared as described above, were introduced into a 50 µL syringe that was connected to the bacterial inlet port. The syringes connected to the gradient generator and the bacterial inlet were operated using different pumps. The flow rate through each of the two gradient inlets was 1000 nL/min, and the flow rate of the bacteria was 100 nL/min, such that the total flow rate through the observation module was 2100 nL/min. For experiments in which a combined gradient of two molecules was applied, one of the inlets contained both chemicals being tested. The different concentration gradients (i.e., concentration range per 1050 microns of chamber width) used in these studies were as follows: L-aspartate, 0 – 100 µM; $NiSO_4$, 0 – 225 µM; AI-2, 0 – 500 µM; indole, 0 – 500 µM; and isatin, 0 – 250 µM. The velocity profile in the device along the x, y, and z-directions of the device was simulated for the channel dimensions and volumetric flow rate used in this study using the equations derived by Brody et al. (24) in Matlab version 7.4.0.

Green and red fluorescence images were acquired for ~ 20 min after cells initially entered the observation module. For each experiment, 100 images for each fluorophore were collected approximately 2/3rds down the length of the observation chamber (~ 7000 microns from the inlet) at 2.5 sec intervals. The 2.5 sec imaging interval was chosen based on our observation that bacteria took ~ 2.5 – 3 sec to traverse a 1000 micron imaging field-of-view; therefore, bacteria were exposed to the gradient for ~ 18 – 21 sec prior to imaging. At the flow rate used, the gradient remained intact for

~90% of the length of the chamber. The middle 90% of the width of the observation module was included in each image.

5.3.5 Quantification of Chemotaxis Using Image Analysis

The migration and distribution of bacteria in each image was quantified using a Matlab (Mathworks, Natick, MA) image-analysis subroutine developed in house. The analysis consisted of the following steps: (i) removal of background pixels in the image based on pixel size and intensities; (ii) determination of the center of the image (i.e., where bacteria enter the observation chamber), using the dead cells (red fluorescence) as the reference; (iii) location of green cells (i.e., live bacteria expressing GFP) in the images relative to the center, determined by calculating the centroid; and (iv) quantification of the number of live cells in 16 micron wide intervals (channels); there are a total of 64 channels across the width of the chemotaxis chamber. These steps were repeated for each image, and the total counts of cells in each image were summed for analysis. The quantified live and dead cell counts in each channel were scaled to facilitate plotting and comparison.

5.3.6 Chemotaxis Partition and Migration Coefficients

The migration profiles were used to calculate parameters for bacterial responses to chemoeffectors. Chemotaxis partition and migration coefficients (CPC and CMC, respectively) were calculated based on the location of green bacteria in 100 images, as previously described (93). The CPC value represents the direction of migration (i.e.,

towards or away from a gradient) and quantifies the number of bacteria on either side of the bacterial inlet. A CPC value of 0.20 indicates that 20% more of the total bacteria (e.g., 60% moved to the right and 40% moved to the left) moved to the higher-concentration side (right side) than the lower-concentration side (left side) for an attractant, whereas a CPC value of -0.20 indicates that 20% less of the total bacteria moved to the higher-concentration side than the higher-concentration side for a repellent.

The CPC value considers only the direction of bacterial migration. The CMC weights the migration of cells by the distance they move. For example, a cell that moves to the right to the farthest high-concentration position (channel 64) would be given a weighting factor of 1, whereas one that moves halfway into the higher concentration side (channel 48) would be given a weighting factor of 0.5. Thus, CMC values will always be less than or equal to CPC values.

The center of each image (i.e., the region where bacteria move due to flow and not motility, corresponding to the place where signal noise is highest) was not included in the CPC/CMC calculations. The average location (i.e., the channel interval) of the red (dead) cells was calculated based on all of the images generated (100 images per experiment over 45 experiments). Any cell that was located within 3 channels of the mean location of the dead cells (~ 48 microns on either side) was excluded from the analysis. Less than 1% of the dead bacteria were detected outside of this limit, whereas live bacteria were detected at all locations in the channel. This analysis allowed us to identify bacteria that exhibited significant movement from the center of the channel and eliminated biases due to bulk flow.

5.4 Results

5.4.1 Chemotaxis Toward a Canonical Attractant and Away from a Canonical Repellent

The formation of a concentration gradient in the device was first demonstrated using a gradient of 0 – 100 ng/mL of fluorescein. **Figure 5.2A** shows that the gradient formed in the µFlow device channel is linear for most of its 1050 µm width. The velocity profile in the channel was simulated in order to determine the time for which bacteria were exposed to the different gradients. The velocity profile along the length and width of the channel (y and x directions, respectively) was uniform at all planes (not shown), whereas the velocity profile in the z-direction varied along the height of the channel (**Figure 5.2B**). At the mid-plane along the z-direction, the velocity was ~ 2500 µm/sec but decreased sharply beyond a distance of 5 microns on either side of the mid-plane. Since the bacteria were present at all z-planes, our simulation results suggest that bacteria in the mid-plane could move at a much higher velocity than those present near the top or bottom surface of the channel. In addition, since bacterial migration is also likely to be retarded by the flagella colliding with the top or bottom surface of the channel, the average velocity of bacteria in the device is likely to be lower than the theoretical value of ~ 2500 µm/sec, and the minimum residence time in the device greater than ~ 7 sec. Indeed, our observations over the ~ 45 experiments indicate that the average time taken for a bacterium to cover a 1000 microns imaging field-of-view was ~ 2.5 – 3 sec. Since the imaging point was ~ 7000 microns from the inlet, the average time

for which bacteria were exposed to the gradient before imaging was calculated to be ~18 – 21 sec.

The migration of *E. coli* RP437 was initially determined for the known attractant L-aspartate and the known repellent Ni^{2+} (93). Gradients of 0 – 100 µM L-asparate/1050 µm and 0 – 225 µM $NiSO_4$/1050 µm were established in the µFlow device. A mixture of GFP-labeled *E. coli* RP437 cells and RFP-labeled dead *E. coli* TG1 cells were introduced into the device such that the entering bacteria immediately encountered the midpoint of the established gradient (i.e., 50 µM L-aspartate and 122.5 µM $NiSO_4$, respectively). **Figures 5.3A & B** show representative pseudo-colored fluorescent micrographs of bacteria after ~ 18 - 21 sec exposure to the gradient. Cells respond to L-aspartate by migrating toward the higher concentration, since more cells move to the right. In contrast, Ni^{2+} repels RP437 cells, since almost all movement was toward the left. It should be noted that 300 µM $NiSO_4$ has little effect on the aerobic growth rate of RP437 cells in TB, nor does it have any significant effect on motility in TB (S. Meghani, unpublished data).

Chemotaxis was quantified by determining the spatial distribution of GFP-expressing RP437 cells and RFP-expressing dead TG1 cells. Dead bacteria were tightly distributed and were predominantly located in a ~50 micron region at the center of the channel (**Figure 5.4**). Thus, the effect of bulk flow on the distribution of these cells was minimal. In contrast, live bacteria were detected at all positions across the channel. In the absence of any signal (chemotaxis buffer in both signal inlets) or with a uniform signal concentration across the channel (100 µM – 100 µM L-aspartate), the mean

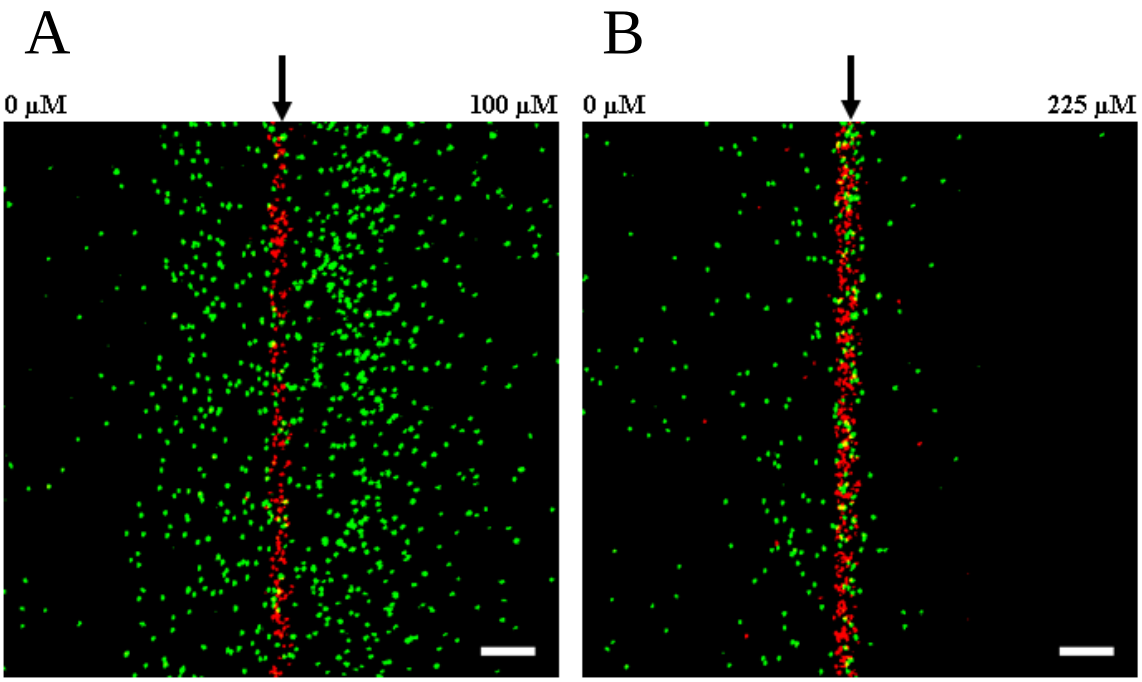

Figure 5.3: Chemotaxis in response to gradients of L-aspartate and $NiSO_4$. RP437cells were exposed to gradients of 0 – 100 µM L-aspartate and 0 – 225 µM $NiSO_4$. Representative fluorescence images of movement toward L-aspartate (A) and away from Ni^{2+} (B) are shown. Live cells are green, and dead cells are red. An arrow indicates the position along the width of the chamber where cells enter. The low concentration is to the left, and the high concentration is to the right. Scale bar indicates 100 µm.

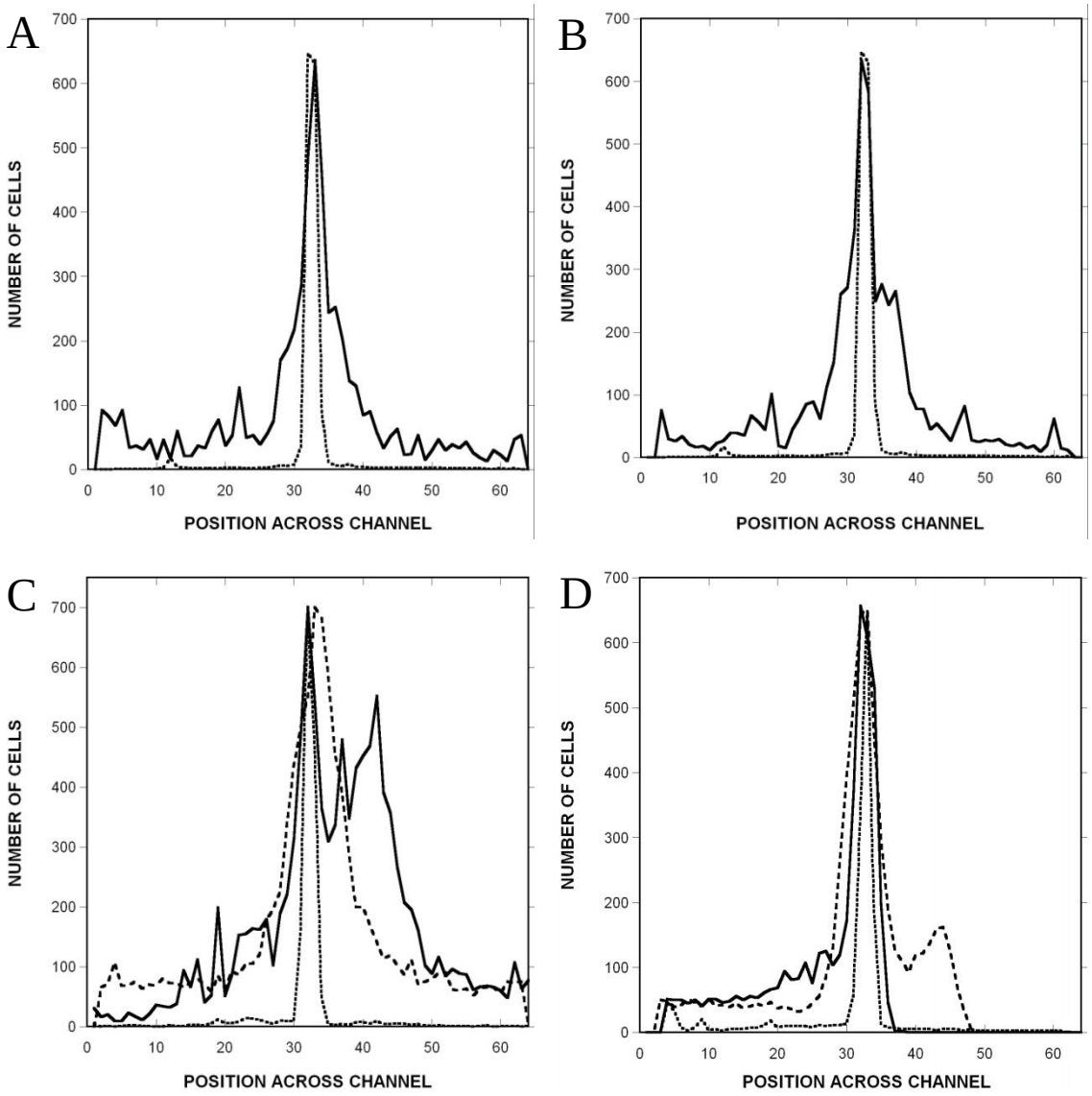

Figure 5.4: Quantification of migration profiles to a canonical attractant and repellent. Spatial distribution of RP437 and RP437 *eda*$^{+}$ *Δtar* cells in response to gradients of L-aspartate and $NiSO_4$. Controls with strain RP437 were run with: (A) no chemoeffector; (B) uniform 100 μM L-aspartate. Panels (C) and (D) show responses to a 0 – 100 μM gradient of aspartate and a 0 – 225 μM gradient of $NiSO_4$, respectively. The distribution of TG1 (dead) cells is shown as a dotted line, the distribution of RP437 cells is shown as a solid line, and the distribution of RP437 *eda*$^{+}$ Δ*tar* cells is shown as a dashed line. The number of live and dead bacteria in 16 micron-wide channels across the width of the chemotaxis chamber was calculated using image analysis. The midpoint of the chamber (where bacteria enter) corresponds to channels 32-33. Data shown are averaged for three independent experiments.

position of the live cells was indistinguishable from that of the dead cells **(Figures 5.4A & B**), although their distribution was much broader.

Chemotaxis toward L-aspartate and away from Ni^{2+} is evident from the markedly different profiles obtained with RP437 and RP437 *Δtar* cells. For example, RP437 cells moved preferentially to the right (high concentration) in the aspartate gradient (**Figure 5.4C**), whereas no such bias was seen with the *Δtar* mutant. Similarly, virtually no RP437 cells were detected on the right (high-concentration) side of the device in the $NiSO_4$ gradient (**Figure 5.4D**), whereas the *Δtar* cells moved to both sides of the cell inlet, although not as far to the right. The device thus yields the expected results for a canonical attractant and a canonical repellent sensed by Tar.

Table 5.1 shows the CPC and CMC values for RP437 cells (see Materials and Methods). For the 0-100 μM L-aspartate gradient, the CPC value was 0.33 ± 0.05, and the CPC value in the 0-225 μM $NiSO_4$ gradient was -0.34 ± 0.04. The corresponding CMC values were 0.13 ± 0.03 and -0.14 ± 0.03. The CPC and CMC values for the *Δtar* strain were significantly smaller (CPC and CMC values for L-aspartate, 0.02 ± 0.02 and 0.01 ± 0.01; CPC and CMC values for $NiSO_4$: -0.07 ± 0.03 and -0.05 ± 0.02), a result that confirms the specificity of the responses.

5.4.2 Chemotaxis Toward or Away from Bacterial Cell-Cell Communication Signals

Next, chemotaxis toward or away from different potential chemoeffectors generated by bacterial metabolism was investigated. Specifically, we focused on the general quorum-sensing signal AI-2 (69) and on the stationary-phase signal indole (85).

Table 5.1: CPC and CMC values of RP437 and RP437 Δ*tar* cells for concentration gradients of different chemoeffectors.[b]

Signal(s)	Concentration Gradient (µM)	CPC	CMC
No signal (blank)	0 – 0	0.03 ± 0.01	-0.01 ± 0.01
Null gradient (L-aspartic acid)	100 – 100	-0.01 ± 0.01	-0.01 ± 0.01
L-Aspartic acid	0 – 100	0. 33 ± 0.05	0.13 ± 0.03
L-Aspartic acid[a]	0 – 100	0.02 ± 0.02	0.01 ± 0.01
Nickel sulfate	0 – 225	-0.34 ± 0.04	-0.14 ± 0.03
Nickel sulfate[a]	0 – 225	-0.07 ± 0.03	-0.05 ± 0.02
AI-2	0 – 500	0.28 ± 0.05	0.11 ± 0.02
DMSO solvent	0 – 500	-0.01 ± 0.01	0.01 0.01
Indole	0 – 500	-0.35 ± 0.03	-0.15 ± 0.02
Isatin	0 – 250	0.21 ± 0.05	0.09 ± 0.01
Indole + AI-2	0 – 500 / 0 – 500	0.19 ± 0.03	0.08 ± 0.02

[a] RP437 *eda*$^+$ Δ*tar*
[b] Mean values and standard deviations for data from 100 images per experiment over three independent experiments are shown.

The responses of RP437 cells to gradients of 0 – 500 µM AI-2/1050 µm and 0 – 500 µM indole/1050 µm were measured. The migration profiles in each case were significantly different from the blank and null-gradient controls (**Figures 5.5A & B**). The DMSO solvent present in the AI-2 sample was shown to be inactive (**Figure 5.5A**). The 0 – 500 µM gradient of AI-2 (CPC and CMC values of 0.28 ± 0.05 and 0.11 ± 0.02, respectively) was also only slightly less effective than a 0 – 100 µM gradient of L-aspartate as an attractant (**Table 5.1**). Similarly, the distribution of cells within a gradient of 0 – 500 µM indole (CPC and CMC values of -0.35 ± 0.03 and -0.15 ± 0.02, respectively) was comparable to that observed with a 0 – 225 µM gradient of $NiSO_4$ (**Figure 5.5B**).

The migration of RP437 cells in response to a 0 – 250 µM /1050 µm gradient of isatin (indole 2,3-dione) (86) was also investigated (**Figure 5.5C**). Although *E. coli* lacks the enzymes required to convert indole to isatin, the monooxygenase activity required to generate isatin is present in other bacteria that co-exist with *E. coli* (e.g., Pseudomonas) (86). Therefore, isatin is likely to be present in mixed bacterial communities. The CPC and CMC values for isatin were 0.21 ± 0.05 and 0.09 ± 0.01, respectively (**Table 5.1**), indicating that *E. coli* senses isatin as an attractant, although these cells move away from indole, a precursor of isatin.

5.4.3 Chemotaxis in Mixed Gradients

Bacteria are likely to encounter gradients of different chemoeffectors simultaneously in their local microenvironments; for example, both AI-2 and indole are

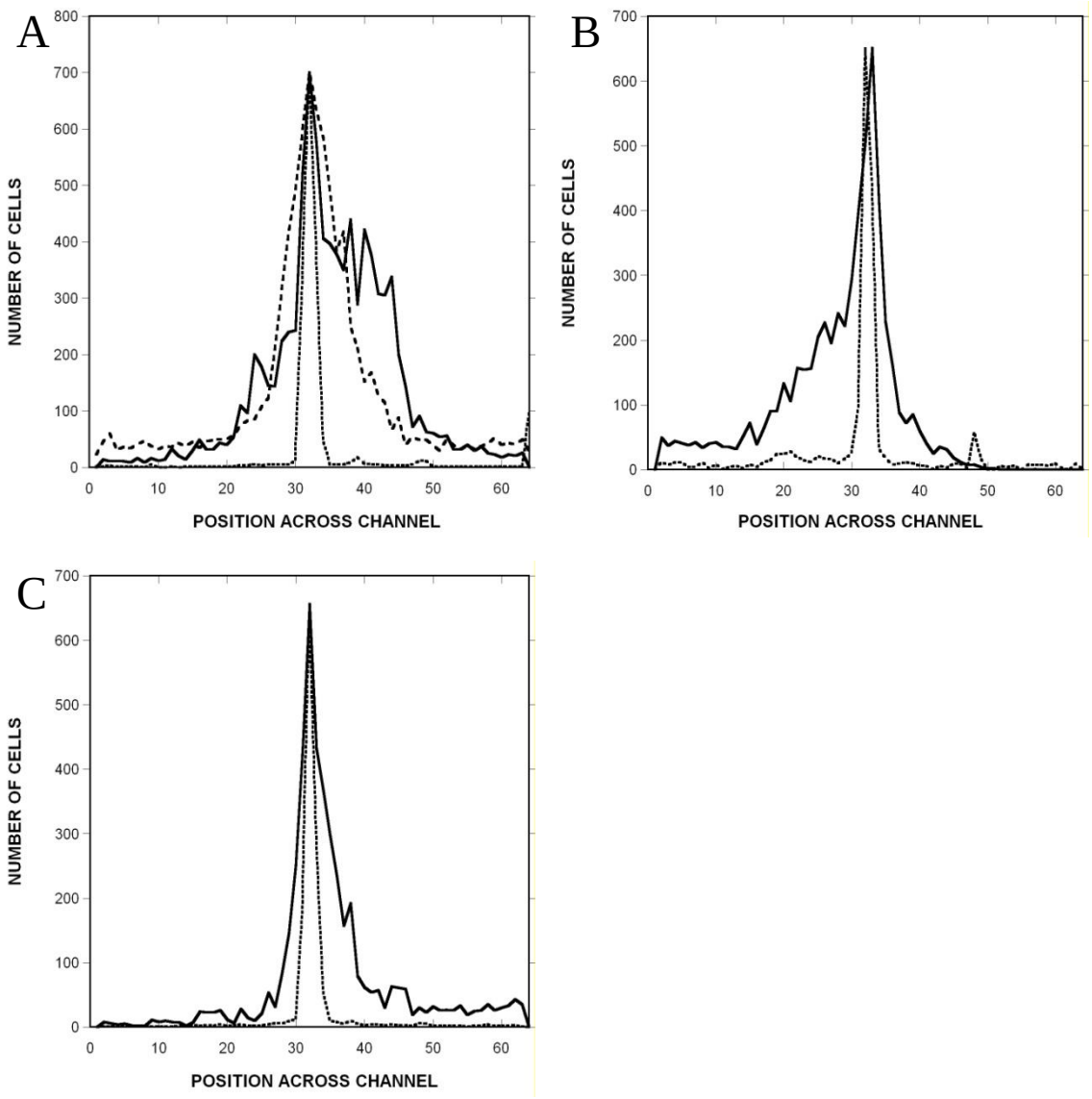

Figure 5.5: Migration profiles in response to gradients of potential chemoeffectors. Panel (A) shows the spatial distribution of RP437 cells from one of three representative experiments in gradients of 0 – 500 µM AI-2 and 0 – 500 µM DMSO. The distribution of dead cells is shown with a dotted line, the distribution of living cells in the AI-2 gradient is shown with a solid line, and the distribution of living cells in the DMSO gradient is shown with a dashed line. Panels (B) and (C) show the distribution of cells in gradients of 0 – 500 µM indole and 0 – 250 µM isatin, respectively. The distribution of dead cells is shown with a dotted line, and the distribution of living cells is shown with a solid line. Data were collected and analyzed as for **Figure 4.4**.

produced by commensal *E. coli*. Since indole is a repellent and AI-2 is an attractant, the migration of *E. coli* RP437 in the presence of competing gradients of both chemicals was investigated. Cells were exposed to combined gradients of 0 – 500 µM indole and 0 – 500 µM AI-2/1050 µm, and the resulting migration profiles were determined (**Figure 5.6**). The CPC value for the combined gradient was 0.19 ± 0.03 (**Table 5.1**) and the corresponding CMC value was 0.08 ± 0.02. These values are about 70% of those found in the absence of a competing indole gradient, indicating that at these concentrations, attraction to AI-2 dominates over repulsion by indole.

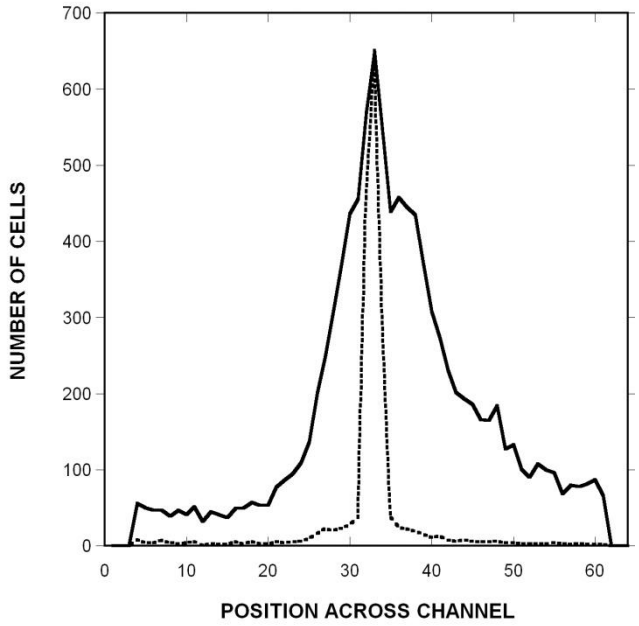

Figure 5.6: Migration profiles in response to combined gradients of potential chemoeffectors. Spatial distribution of RP437 cells from one of three representative experiments for a combined gradient of 0 – 500 µM AI-2 and 0 – 500 µM indole. The distribution of dead cells is shown with a dotted line, and the distribution of living cells is shown with a solid line. Data were collected and analyzed as for **Figure 4.4**.

5.5 Discussion

Bacteria are constantly exposed to competing gradients of different chemicals in their local microenvironments. However, conventional methods for investigating bacterial chemotaxis have focused primarily on responses to single chemoeffectors (4). In this study, we report the development of a flow-based microfluidic system capable of investigating chemotaxis in response to stable concentration gradients of single and multiple chemoeffectors.

Different microfluidic devices, ranging from static (no-flow) systems to simple flow devices, have been developed previously. Static chemotaxis systems, such as hydrogel and agarose-based devices (32, 41), are useful because they facilitate rapid screening of different signals with minimal equipment needs. The μFlow device described here generates gradients that are stable in space and time, and it can be used to generate multiple gradients simultaneously. It also represents a physiologically relevant model for environments such as the human GI tract, since it creates an environment in which chemotaxis occurs transverse to bulk flow. It should be noted that Ford and co-workers (83) also recently demonstrated bacterial chemotaxis transverse to fluid flow.

In our μFlow device, bacteria entering the chemotaxis chamber immediately encounter established gradients of chemoeffectors, and the cells experience a stable gradient throughout the length of the channel. This situation contrasts with the systems described by Mao et al. (93) and Lanning et al. (83), in which gradients are established in the observation chamber such that the bacteria flowing through the chamber are exposed to a changing gradient. This difference in design leads to a longer time available

for cells to respond to the gradient in our device, making it more appropriate for investigating signals that elicit weaker responses.

Lamanna et al. (82) suggest that sudden, large increases in attractant concentration may disrupt localization of chemoreceptors and inhibit signal transduction. Thus, bacteria suddenly exposed to a high signal concentration, as in the device described by Mao et al. (93), could show an atypical, non-physiological response. However, by establishing the final gradient at the chamber inlet, the μFlow device enables investigation of responses in the absence of perturbing "edge" or "step" effects. Furthermore, defined gradients can be generated at any absolute concentration and steepness desired.

Since chemotaxis occurs transverse to bulk fluid flow in the μFlow device, it could be argued that hydrodynamic effects might impact the chemotaxis response. We addressed this problem by differentially labeling dead bacteria so that motility could be distinguished from movement due to bulk flow. Data from nearly 50 independent experiments show that dead bacteria (labeled red) always migrate near the center of the observation chamber, whereas live bacteria (labeled green) are present in all positions across the width of the channel. Thus, the analysis presented here accurately represents chemotaxis, since the position of dead cells that move only through bulk flow is accounted for in each experiment. The increased dispersal observed by RP437 in the absence of chemoeffector or in a null gradient (i.e., a uniform concentration of chemoeffector) also indicates that the migration observed is due to the intrinsic motility of the cells (**Figure 5.4A & B**).

Our data provide several insights into chemotaxis responses to inter- and intraspecies cell-cell communication signals. First, the CPC and CMC values observed with AI-2 and isatin as attractants, and with indole as a repellent, respectively, were comparable to those seen with the canonical attractant and repellent sensed by Tar: L-aspartate and Ni^{2+}, respectively. Indole is known to be sensed by Tsr (124), but there is very limited information about how AI-2 and isatin are perceived by *E. coli*. Since AI-2 can be taken into cells via the *lsr* genes (131, 136, 143), it is possible that this operon is involved in the chemotactic response to AI-2. The attraction observed with isatin is intriguing, as isatin is a derivative of the repellent indole. The basis for the diametrically opposed effects of these two structurally similar compounds remains to be determined, as is the attraction observed with a combined gradient of AI-2 and indole.

The generation of countervailing gradients of different attractants or repellents can help determine the relative strengths of the responses to the different chemoeffectors. Adler and Tso (5) have suggested that bacteria receiving opposing (i.e., attractant and repellent) signals sums up the signals to decide the direction of movement. In other words, the signal that is present at the optimal or most effective concentration will be the one that dominates the response. This suggests that the 0-500 μM gradient of AI-2 was more effective than the 0-500 μM gradient of indole. It should be noted that any synergism or additivity would presumably only be seen for sub-optimal gradients, since the intrinsic properties of the biased random walk are likely to set an upper limit on the drift rate in single or combined gradients. It will be interesting to investigate whether all cells respond the same averaged way or if they fall into two populations that respond

more strongly to different chemoeffectors. If two populations are observed, it will also be instructive to determine if this is true only for chemoeffectors sensed by different receptors, and if so, whether differences in the abundance of different receptor types define the two populations.

Although we used the well-characterized, non-pathogenic *E. coli* lab strain RP437 in these studies, the results here potentially describe mechanisms underlying colonization of the human GI tract by pathogenic strains such as enterohemorrhagic *E. coli* (Englert and Jayaraman, unpublished data). The four classical *E. coli* chemotaxis receptors Tar, Tsr, Tap, Trg, as well as the aerotaxis transducer Aer (104), are also present in EHEC. Thus, chemosensing capabilities are expected to be conserved between these strains. Indeed, unpublished data from our lab show that *E. coli* RP437 and EHEC strains demonstrate similar chemotaxis toward a broad range of signals, ranging from classical chemoeffectors (L-aspartate, Ni^{2+}) to eukaryotic hormones (norepinephrine) to bacterial molecules (AI-2, indole, isatin).

The initial migration of pathogenic bacteria to epithelial cell surfaces is a key step in GI tract infections, and recent studies suggest that chemotaxis is important for this migration. Williams et al. (138) and McGee et al. (95) have demonstrated, using an in vivo model, that adherence of the ulcer-causing bacterium Helicobacter pylori is attenuated in non-motile chemotaxis mutants, suggesting that this pathogen uses chemotaxis to guide itself to the stomach epithelium.

Our data showing that the chemotactic attraction towards AI-2 is stronger than the repulsion by indole at the concentrations tested could also be a significant factor in

EHEC colonization, since both of these molecules are likely to be present in the same local microenvironment. For example, non-pathogenic *E. coli*, which constitute ~ 8% of the commensally micro flora in the human GI tract (60, 84), secrete ~ 500 μM indole (85) and ~ 100 μM AI-2 (14) per 109 cells. Prior work has demonstrated that AI-2 increases EHEC motility and attachment to epithelial cells, whereas indole decreases these phenotypes (14, 15). Although many other combinations of competing concentration gradients need to be tested, it is intriguing to speculate that colonization occurs primarily in regions in which the effects of AI-2 dominate over those of indole.

In summary, we have developed a microfluidic flow-based device for investigating interactions between different bacterial chemoeffectors. We have demonstrated that the device allows *E. coli* chemotaxis to be quantified in response to individual and combined signals. Our data suggest that interactions between signaling pairs, such as AI-2 and indole, could be important in determining the extent of pathogen colonization in the GI tract.

CHAPTER VI

REPELLENT TAXIS TO NICKEL ION REQUIRES NEITHER Ni^{2+} TRANSPORT NOR THE PERIPLASMIC NIKA BINDING PROTEIN*

Nickel (Ni^{2+}) and cobalt (Co^{2+}) ions are sensed as repellents by the *E. coli* Tar chemoreceptor. The periplasmic Ni^{2+} binding protein, NikA, has been suggested to sense Ni^{2+}. We show here that neither NikA nor the membrane-bound NikB and NikC proteins of the Ni^{2+} transport system are required for repellent taxis to Ni^{2+}.

E. coli cells are repelled by Ni^{2+} and, with lower sensitivity, Co^{2+} (124). This response is mediated primarily by the aspartate/maltose chemoreceptor, Tar. A Tar-Tsr chimeric receptor fused at residues 256-257 of Tar still senses Ni^{2+}, whereas the reciprocal Tsr-Tar chimera does not (80). The authors of that study concluded that Ni^{2+} is sensed by the N-terminal periplasmic of Tar. The fusion joint is actually near the C-terminal end of AS2, the second amphipathic helix of the HAMP (histidine kinases, adenylyl cyclases, methyl binding proteins and phosphatases) domain (10) that couples the transmembrane sensing domain to the cytoplasmic kinase-control domain. Thus, a more cautious interpretation of their results is that the ability to sense Ni^{2+} is conferred by the periplasmic, transmembrane, or HAMP region of Tar.

---

*Submitted as "Repellent Taxis to Nickel Ion Requires Neither Ni^{2+} Transport nor the Periplasmic NikA Binding Protein" by Derek L. Englert, Chris Adase, Michael D. Manson, and Arul Jayaraman to Journal of Bacteriology (In revision).

The five-gene *nikABCDE* operon encodes ATP-dependent high-affinity uptake system for Ni^{2+}. This operon is quite similar in its construction to the five-gene operons encoding the oligopeptide (Opp) and dipeptide (Dpp) transport systems (2, 65). Furthermore, the periplasmic binding proteins encoded by the first gene of all three operons are very similar in their folds (142). The DppA protein interacts with the Tap chemoreceptor of *E. coli* and is the substrate-recognition component of the attractant chemotaxis response to dipeptides (1, 43, 92). The NikA binding protein (98) has been suggested to be the substrate-recognition component of repellent chemotaxis to Ni^{2+} (40). However, there are several problems with this proposal. First, NikA is produced only under conditions of anaerobiosis (40) and Ni^{2+} limitation (39), but Ni^{2+} taxis is seen in cells grown aerobically in tryptone broth whether or not $NiSO_4$ is present (47). Second, concentrations of Ni^{2+} that are needed to see significant responses to up or down step changes are between 10 and 100 μM (124), whereas the K_d for Ni^{2+} binding to NikA is on the order of 0.1 μM (40). Third, the other periplasmic binding proteins of *E. coli* that are involved in chemotaxis – DppA, the ribose-binding protein (RBP; (7)), the galactose/glucose-binding protein (GBP; (62)), and the maltose-binding protein (MBP; (61)) – all mediate attractant taxis. Thus, NikA would have to evoke a response opposite to those generated by the other binding proteins.

These apparent discrepancies led us to examine whether NikA actually is the Ni^{2+} sensor in *E. coli*. We obtained knockout mutations of the *nikA*, *nikB*, and *nikC* genes from the Keio collection (12). These mutations replace the bulk of a given gene sequence with a kanamycin-resistance cassette. The knockout mutations were

transferred into the chemotactically wild-type strain CV1 (identical to RP437; (103)), and the transfer of the mutations was confirmed by PCR analysis (**Figure 6.1**). **Figure 6.2** shows the primers used for PCR analysis shown in **Figure 6.1**.To insure that we were always working with mutant cells, we left the Kan^r cassettes in the disrupted genes. Although the *nikA* insertion could have a polar effect on *nikBC*, and the *nikB* insertion could have a polar effect on *nikC*, we could still independently assess the effect of knocking out Ni^{2+} transport while retaining NikA with the *nikB* and *nikC* insertions and of eliminating Ni^{2+}-binding protein and transport with the *nikA* insertion.

Next, we investigated the effect of the *nikA*, *nikB*, and *nikC* mutations on chemotaxis, using our recently described microfluidic chemotaxis device (47). In this device, diffusive mixing between two inlet concentrations of a chemoeffector is used to generate a gradient of the chemoeffector. Bacteria entering the device immediately encounter the midpoint of the gradient and are exposed to it for ~ 16-21 sec before imaging. This assay allows easy and rapid quantification of the chemotactic response. **Figure 6.3** shows the response of wild type and *nik*-mutant cells to a gradient of 0 – 100 μM $NiSO_4$. Representative composite pseudo-colored images of chemotaxis under the different conditions are shown in **Figure 6.4**. High motility *E. coli* cells were prepared as described (47) except that cells were harvested and washed by centrifugation at 150 x g instead of by filtering. The low-speed centrifugation method produced a higher proportion of fully motile cells. Cells in chemotaxis buffer containing 50 μM $NiSO_4$ were introduced at the midpoint of the 0-100 μM Ni^{2+} gradient. The wild-type cells

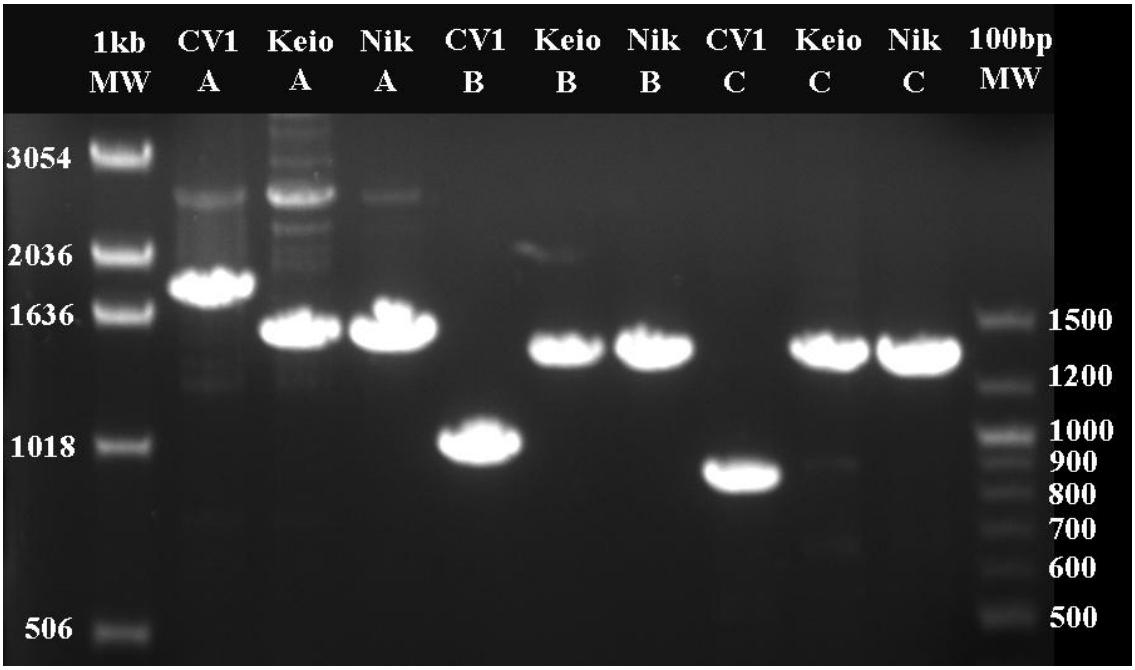

Figure 6.1: PCR products of *nik*-knockout genes in strain CV1. Phage $P1_{vir}$ transduction was used to transfer *nikA*, *nikB*, and *nikC*-knockout mutations from their respective Keio collection K-12 strain (12) to strain RP437 (CV1). Colonies were selected on Luria Bertani (LB) agar (18) containing 15µg/mL kanamycin. Kan^r transductants were transformed with plasmid pCM18 (Erm^r) encoding green fluorescent protein (GFP). Transformants were selected on LB agar containing 15µg/mL kanamycin and 120 µg/mL erythromycin. Multiple colonies were picked, grown overnight in tryptone broth (TB) containing 60 µg/mL erythromycin and 15 µg/mL kanamycin, then back diluted into the same medium and grown to mid-logarithmic phase (OD_{600nm} = 0.7). Chromosomal DNA preparations were made following the procedure of A. Z. Buscher of the P. A. Levin Laboratory (11). Forward and reverse primers were designed for each gene (**Figure 6.2**). The forward primer for *nikA* was complementary to a sequence somewhat farther upstream, leading to a slightly larger PCR product. The PCR product for each gene was compared for the original CV1 strain (CV1 A-C), the original Keio strain Keio A-C, and the transductants (Nik A-C). PCR products were run at 120 volts for 90 min on a 1% agarose gel containing 0.1µl/ml ethidium bromide. Two different base pair length standards are shown to the right and left; the sizes, in base pairs, are indicated.

A

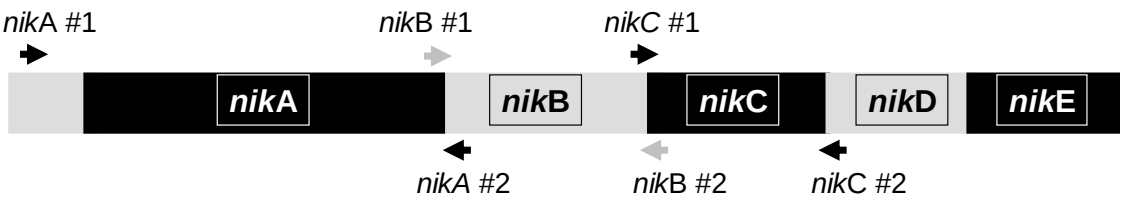

B

Primer name	Primer Sequence	# bases	T_m
*nik*A #1	ATT CGT CGT CAT GAA GGA GCG CA	23	62.5
*nik*A #2	CGA TAT TAC GTA GGT CAA TCT GTT GCG GC	29	62.6
*nik*B #1	CGA ACA GAT TAA ACC GGT GAA ACC TTA	27	59.6
*nik*B #2	CGA CCA GCG GGA AGA GAG GAA A	22	61.3
*nik*C #1	TTT ACG CTC ACC GCC GAC AGT GT	23	62.4
*nik*C #2	AAG CGG CGT AAT ACG TAA CGC AAC A	25	62.4

Figure 6.2: Primer sequences and their locations in the *nik* operon. (A) The location of each forward and reverse primer within the *nik* operon or upstream region is shown. (B) Primer sequences used to generate PCR products. Number 1 designates the forward primer and number 2 designates the reverse primer. Primers were designed to have approximately the same T_m and to be long enough so that they are unique in the *E. coli* chromosome.

show a net migration toward lower concentrations of $NiSO_4$. Cells of the isogenic Δ*tar-tap* mutant CV4 migrate significantly less than CV1 cells, but they do seem to be repelled by higher Ni^{2+} concentrations (dotted line in **Figure 6.3A**). CV1 cells are distributed symmetrically across the channel when the $NiSO_4$ concentration is uniformly 50 μM (**Figure 6.3A**).

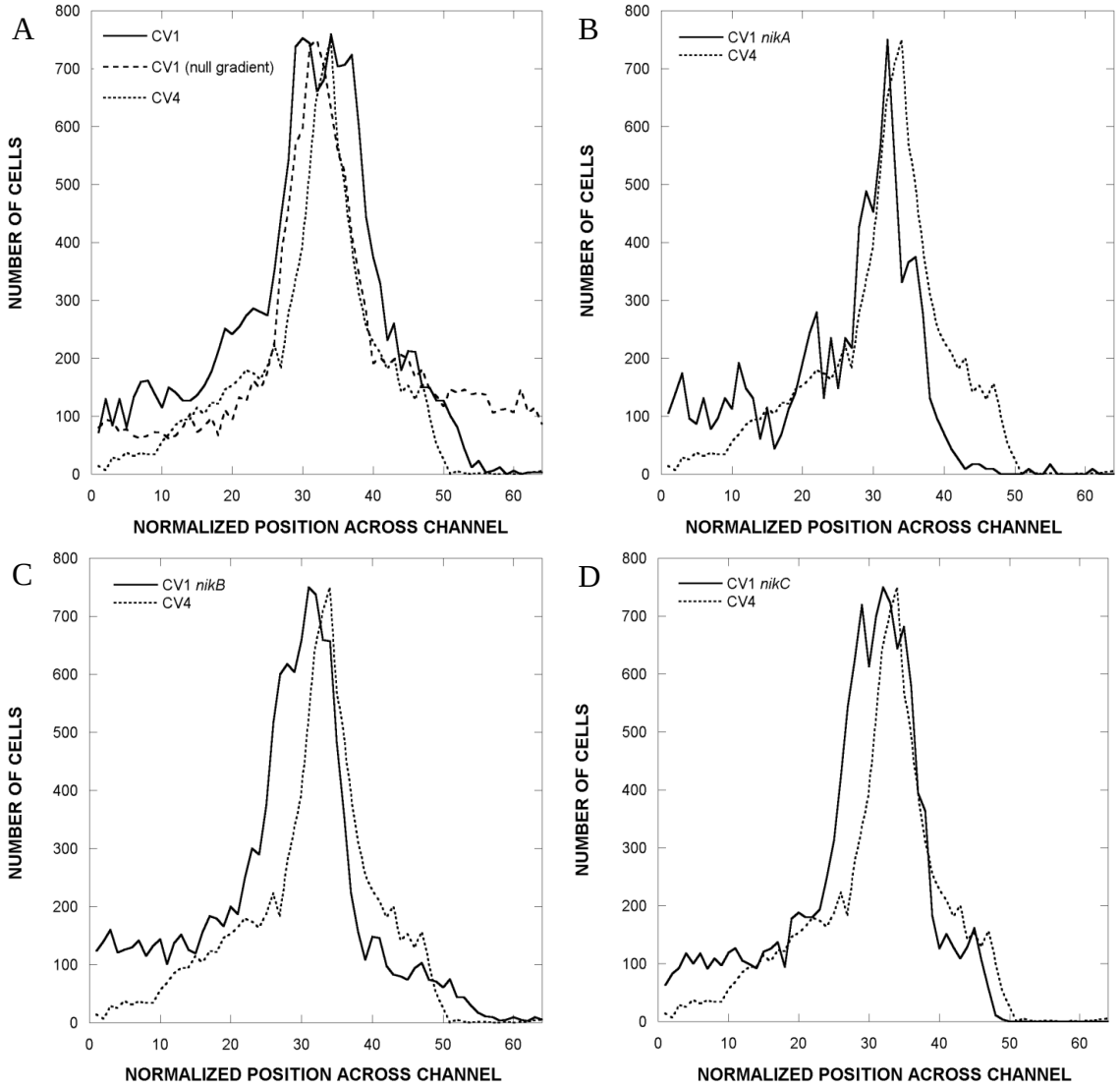

Figure 6.3: Distribution of wild-type and *nik*-knockout strains in a $NiSO_4$ gradient. Cells were exposed to $NiSO_4$ in a previously described microfluidic device (9). The dimensions of the observation chamber are 20 x 1050 x 11500 µm. (A) Comparison of CV1 and CV4 responses to a 0-100 µM gradient of $NiSO_4$. CV1, solid line; CV4 dotted line. The dashed line shows the distribution of CV1 cells when $NiSO_4$ was present uniformly at 50 µM across the channel. (B) Comparison of CV1 *nikA* and CV4 responses to a 0-100 µM gradient of $NiSO_4$. CV1 *nikA*, solid line; CV4 dotted line. (C) Comparison of CV1 *nikB* and CV4 responses to a 0-100 µM gradient of $NiSO_4$. CV1 *nikB*, solid line; CV4 dotted line. (D) Comparison of CV1 *nikC* and CV4 responses to a 0-100 µM gradient of $NiSO_4$. CV1 *nikC*, solid line; CV4 dotted line. Cell counts for each were determined from 100 images taken over a 5 min interval from a point approximately 7000 µm down the channel.

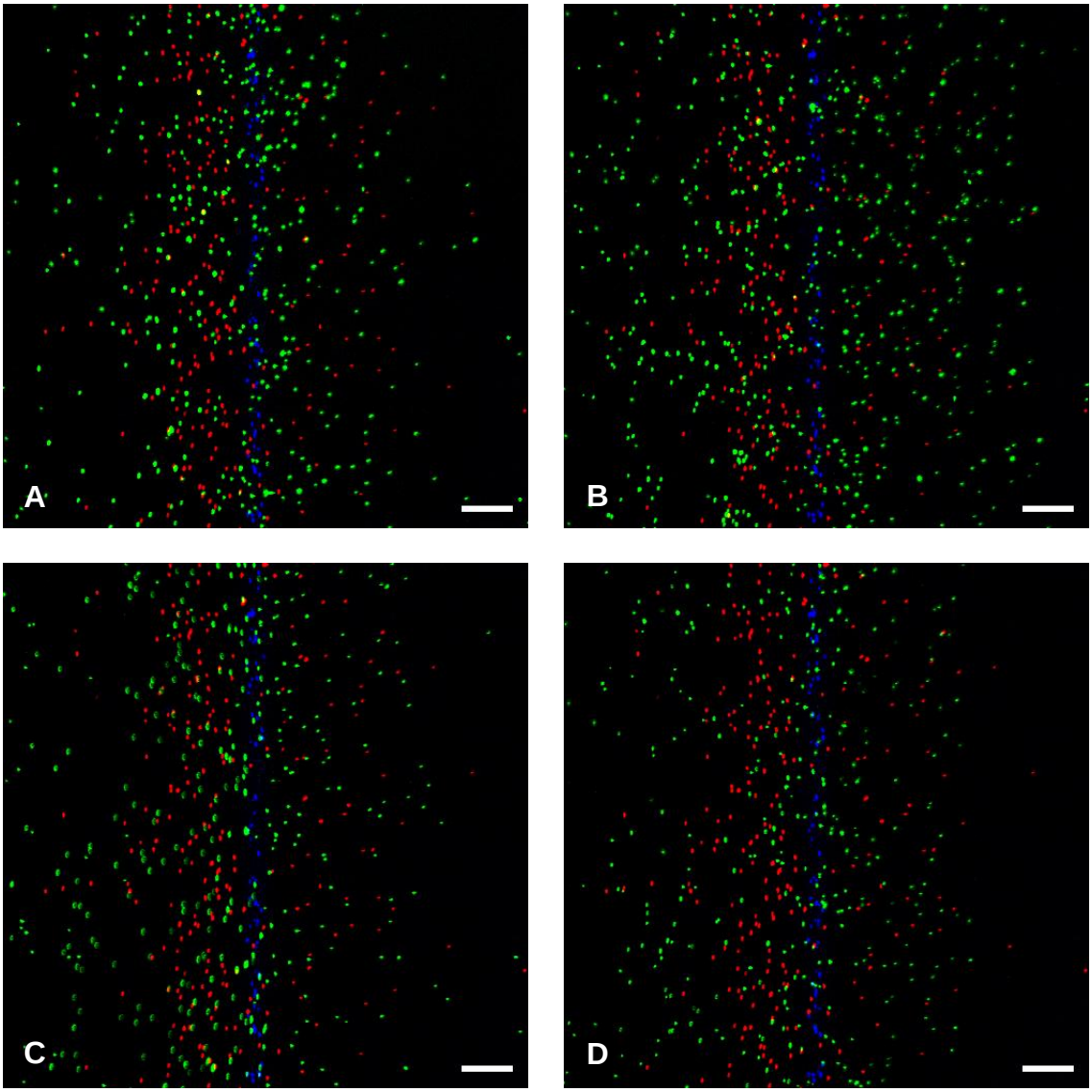

Figure 6.4: Chemotaxis in a $NiSO_4$ gradient. CV1, CV4, and CV1 *nik*-knockout strains were exposed to a gradient of 0-100 μM $NiSO_4$. Representative pseudo-colored overlay images are shown. The high concentration is at the right side of the image. In all images, CV1 or CV1 *nik*-knockout cells are green, CV4 cells are red, and dead cells are blue. (A) CV1. (B) CV1 *nikA*. (C) CV1 *nikB*. (D) CV1 *nikC*. Scale bar indicates 100 μm.

The responses of the *nik*-mutant cells are shown in Figures 6.2B-D. In a 0-100 μM gradient of $NiSO_4$, all three strains show a net migration toward lower Ni^{2+} concentrations. As with strain CV1, more cells are detected at the lower concentrations (i.e., positions 1 – 10 of the device), and the location of the peak also shifts toward lower concentrations. The shift in the peak indicates that most cells in the population respond to the Ni^{2+} gradient. Similar results were obtained when the flow rate was lower, but under those conditions the cells were exposed to the gradient for a longer time before imaging, and the average distance migrated was greater (data not shown).

The extent of migration in response to the Ni^{2+} gradient was quantified based on the chemotaxis partition and migration coefficients (CPC and CMC, respectively). The CPC value reflects the direction of migration (i.e., towards or away from a gradient) and quantifies the number of bacteria on either side of the bacterial inlet (93). For example, a CPC value of -0.30 indicates that 30% more bacteria move to the lower-concentration side than the higher-concentration side. The CMC weights the migration of cells by the distance they move. For example, a cell that moves to the left to the farthest low-concentration position (channel 1) is given a weighting factor of -1, whereas one that moves halfway into the lower concentration side (channel 16) is given a weighting factor of -0.5. CMC values are larger at lower flow rates.

The CPC values for CV1 and all three *nik* mutants (**Table 6.1**) were similar (-0.21 to -0.39). The CPC value for CV4 cells was only -0.08. Cells in a null gradient of NiSO4 (a uniform 50 μM across the channel width) showed a slight bias to the right (CPC of 0.04). Such small CPC values are probably not significant because of the

difficulty in accurately estimating cell number near the point where they enter the chemotaxis channel (i.e., where the cell density is maximal). The CMC values were also comparable for the wild-type and *nik* mutants (-0.11 to -0.16) and significantly higher than for the CV4 *tar* mutant in the same gradient (CMC of -0.06). The CMC value for CV1 cells in the null gradient was 0.05. These results show that repellent taxis to Ni^{2+}, even in this relatively shallow gradient, does not require NikA, NikB or NikC. It should be noted that $NiS0_4$ at concentrations of up to 300 μM does not significantly inhibit growth or motility in TB liquid medium (47).

Our results clearly show that nickel taxis can occur in the absence of the Nik proteins. The marginal response of CV4 cells to the Ni^{2+} gradient raises the possibility that Ni^{2+} is sensed by chemoreceptors other than Tar. The response is so weak, however, that it would have been missed in previous, less-sensitive assays.

The accompanying paper describes an analysis of chimeric proteins that demonstrates that the Ni^{2+}–binding site is in the periplasm. That conclusion is consistent with our observation that Ni^{2+} uptake is not required for repellent taxis to Ni^{2+}. The loss of Ni^{2+} sensing by Tar should give a sufficient difference in behavior to allow for an enrichment, using a variation of our recently developed microfluidic device (47), for *tar* mutants that are Ni^{2+}-blind but still competent for maltose and/or aspartate taxis (54). In this way, we hope to characterize the Ni^{2+}-binding site in detail and shed more light on the poorly understood mechanism of repellent taxis.

Table 6.1: Chemotaxis partition and migration coefficients in a $NiSO_4$ gradient.[a]

Strain	CPC	CMC
CV1 (Null gradient)	0.04 ± 0.01	0.04 ± 0.02
CV1	-0. 31 ± 0.02	-0.13 ± 0.03
CV4	-0.08 ± 0.03	-0.06 ± 0.03
CV1 *nikA*	-0.25 ± 0.05	-0.11 ± 0.01
CV1 *nikB*	-0.39 ± 0.06	-0.16 ± 0.05
CV1 *nikC*	- 0.26 ± 0.01	-0.11 ± 0.01

[a] The gradient ranged from 0 to 100 μM $NiSO_4$ in chemotaxis buffer across the 1050 μm wide channel except for the null gradient where the Ni^{2+} concentration was constant at 50 μM across the channel.

CHAPTER VII

MODELING GROWTH AND QUORUM SENSING IN BIOFILMS GROWN IN MICROFLUIDIC CHAMBERS*

7.1 Overview

Biofilms are highly organized structures coordinately formed by multiple species of bacteria. Quorum sensing (QS) is one cell-cell communication mechanism that is used by bacteria during biofilm formation. Biofilm formation is widely acknowledged to occur through a sequence of spatially and temporally regulated colonization events. While several mathematical models exist for describing biofilm development, these have been developed for open systems and are not applicable to closed systems where biofilm development and hydrodynamics are interlinked. Here, we report the development of a mathematical model describing QS and biofilm formation in a closed system such as a microfluidic channel. The model takes into account the effect of the external environment *viz* the mass and momentum transport in the microfluidic channel on QS and biofilm development. Model predictions of biofilm thickness were verified experimentally by developing *Pseudomonas aeruginosa* PA14 biofilms in microfluidic chambers and reflect the interplay between the dynamics of biofilm community development, mass transport, and hydrodynamics. Our QS model is expected to guide

---

*Reprinted with permission from "Modeling Growth and Quorum Sensing in Biofilms Grown in Microfluidic Chambers" by Vijay Janakiraman, Derek Englert, Arul Jayaraman, and Harihara Baskaran, 2009, Annals of Biomedical Engineering 37: 1206-1216, Copyright by Biomedical Engineering Society.

the design of experiments in closed systems to address spatio-temporal aspects of QS in biofilm development and can lead to novel approaches for controlling biofilm formation through disruption of QS spatio-temporal dynamics.

7.2 Introduction

Biofilms are highly organized structures of multi-species microbial communities that are formed by attachment to surfaces and secretion of an exopolysaccharide matrix along with cell debris from lysed cells (nucleotides and proteins) (35, 36). It has been established that bacteria primarily exist in association with surfaces rather than as free-floating planktonic cells (135, 139). Biofilms are ubiquitous and found in a wide range of clinical and industrial settings including medical implants and devices (35), water pipes (29), and heat exchangers (44). Biofilms pose a serious problem in human health (36, 37) as they are highly resistant to antimicrobial agents and biocides, and are extremely difficult to completely eradicate once they are fully developed (87, 91). Therefore, understanding the mechanisms involved in the formation of biofilms is important for developing effective ways to control their formation.

Several studies have clearly demonstrated the importance of cell-cell communication in biofilm formation (56, 105, 139). Commonly termed as quorum sensing (QS) (134), this is an important signaling mechanism used by bacteria to monitor their population density during growth and regulate the expression of genes controlling different phenotypes. A recent development in QS research is the notion that spatial and temporal gradients of QS molecules (*i.e.*, when QS molecules are produced

and how they are distributed in a developing biofilm community) are key determinants of the extent of biofilm formation. Experimental systems that are commonly used to investigate biofilm formation and dynamics (56) are macroscopic and involve the use of large flow cells that preclude rigorous control of the spatio-temporal microenvironment around the biofilm. However, microfluidic techniques enable precise control of biofilm microenvironment, and are ideally suited for investigating the role of QS spatio-temporal dynamics in biofilm formation. While microfluidic methods have been employed in various biological applications that range from electrophoresis to cell engineering (48, 97, 109, 130), they have been only recently used for investigating biofilm formation and quorum sensing.

Mathematical models of biofilm can be used to obtain insights on the effect of various factors on QS and biofilm development. Such models can also minimize the number of experiments needed to investigate the biological process. Currently, most mathematical models that address quorum sensing within biofilms are spatially-lumped models (42, 127, 132, 133). These models are ideal for studying the temporal dynamics of the quorum sensing systems as asymptotic or complete solutions can be obtained through analytical means. Chopp et al. (33, 34) developed a spatially-distributed continuum model of *Pseudomonas aeruginosa* biofilm growth that incorporated features of quorum sensing such as the production, degradation, and diffusion of acyl-homoserine lactones in the biofilm. They concluded that quorum sensing is affected greatly by the biofilm depth and that a critical depth is needed to trigger quorum sensing in the biofilm (34). However, this model cannot be applied for microfluidics systems where external

conditions that govern biofilm growth and quorum sensing (i.e., flow rate, shear-stress) are themselves affected dynamically by the growth of biofilms (112).

The goal of this work is to quantitatively understand the formation and maintenance of biofilms in a microfluidic system where external hydrodynamic effects play an important role. A mathematical model was developed to describe QS and biofilm formation in microfluidic devices. In addition to the general characteristics of biofilm formation, the model takes into account its effect on the external environment *viz* the mass and momentum transport in the microfluidic channel. Model predictions of biofilm thickness were evaluated experimentally by developing *P. aeruginosa* biofilms in microfluidic chambers. The model developed can also be extended to quantitatively understand the role of QS in the development of multispecies biofilm communities.

7.3 Methods

7.3.1 Model Development

In this section, we develop a continuum-based mathematical model to describe the nutrient- and external hydrodynamics-dependent growth of a biofilm.

7.3.1.1 General Model

A biofilm can be considered to consist of diffusible and non-diffusible species. The bacterial biomass, both active (cells) and inert (exopolysaccharide, DNA, and proteins), is non-diffusible and changes in levels of biomass occurs primarily due to

nutrient-dependent growth. Nutrient limiting substrates such as O_2, and quorum sensing molecules such as N-acylhomoserine lactone (acyl-HSL) and AI-2, are the diffusible species and their levels change due to diffusion as well as consumption/production by cells.

The general one-dimensional unsteady species conservation equation is:

$$\frac{\partial \rho_i}{\partial t} + \frac{\partial n_{iz}}{\partial z} = r_i \tag{7.1}$$

Here, ρ_i represents the mass concentration of species i, n_{iz} represents the mass flux of species i in the *z* direction, and r_i represents the rate of production of i. Fick's law of diffusion is:

$$n_{iz} = \rho_i u_z - D_i \frac{\partial \rho_i}{\partial z} \tag{7.2}$$

Here, D_i represents the diffusivity of the species in the biofilm, and u_z is the mass averaged velocity. Note that for non-diffusible species, the right most term will be zero. Substituting Fick's law of diffusion in Eq. (7.1), the conservation equation can be written as:

$$\frac{\partial \rho_i}{\partial t} = r_i - \frac{\partial}{\partial z}\left(\rho_i u_z\right) + D_i \frac{\partial^2 \rho_i}{\partial z^2} \tag{7.3}$$

For non-diffusible substances such as bacterial biomass, the above equation can be simplified.

$$\frac{\partial \rho_i}{\partial t} = r_i - \frac{\partial}{\partial z}\left(\rho_i u_z\right) \tag{7.4}$$

From Eq. (7.1), assuming constant overall density, we can obtain an overall mass balance equation by summing over all species:

$$\rho \frac{\partial u_z}{\partial z} = \sum_i r_i \tag{7.5}$$

This equation describes the average velocity in the growing biofilm. The assumption of constant *overall* density is warranted as experimental information about the overall density dynamics, *viz* a constitutive relationship, in a biofilm is lacking in the literature, and making such an assumption is probably acceptable given that the biofilm mass density is similar to that of water.

7.3.1.2 Biofilm Growth Rate

In a microfluidic environment, the biofilm surface forms one of the chamber walls (**Figure 7.1**). Due to the confined environment, as the biofilm grows the hydrodynamic environment surrounding the biofilm also changes. Here, we consider the effect of shear-stress on the biofilm surface by allowing for a shear-stress dependent detachment rate, $\xi(\tau_w)$.

$$\frac{dL}{dt} = u_z(t, L) - \xi(\tau_w) \tag{7.6}$$

Here, L represents the thickness of the biofilm. The shear-stress (τ_w) in the micro-channel changes with the biofilm growth, and so will the detachment rate $\xi(\tau_w)$. Currently, no phenomenological relationships are available to describe shear-stress

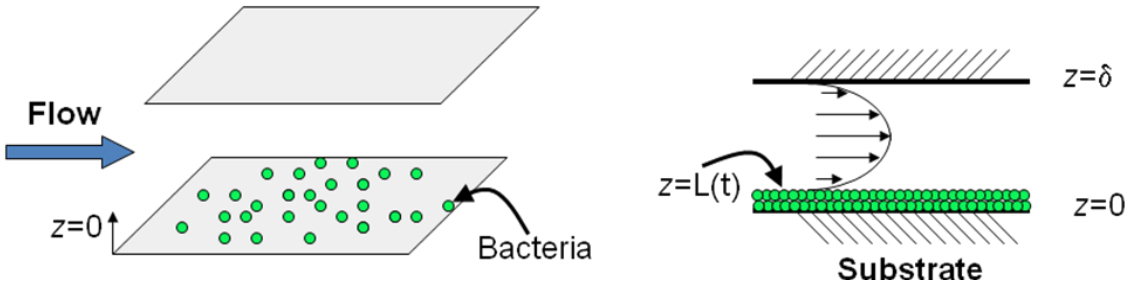

Figure 7.1: Schematic representation of biofilm model. As the biofilm thickness increases, the flow characteristics are also impacted.

dependent biofilm detachment. Experimental studies, however, have been performed to determine the effect of shear-stress conditions on biofilm growth (66, 107). Based on these studies, we propose the following *empirical* relationship between the detachment rate and the shear-stress,

$$\xi = \xi_{max}\left(1\text{-}e^{-k\tau_w}\right) \tag{7.7}$$

Here, τ_w is the shear-stress at the surface of the biofilm, ξ_{max} (maximum detachment rate) and k_w are parameters that were estimated from experimental results (66, 107).

The shear-stress at the biofilm surface can be evaluated from the hydrodynamic conditions in the microchannel. If we assume that the flow development occurs faster than the growth of the biofilm, one can then obtain an expression for the velocity field in the microchannel (71)

$$v_y(x,z,t) = \left(-\frac{dP}{dy}\right)\frac{8}{\pi^3}\frac{W}{\mu}\sum_{n=1,3,\ldots}^{\infty}\frac{(-1)^{(n-1)/2}}{n^3}\left(1-\frac{\cosh(n\pi z/W)}{\cosh\left[n\pi(\delta-L(t))/2W\right]}\right)\cos\left(\frac{n\pi x}{W}\right) \tag{7.8}$$

and an expression for shear-stress at the surface of the biofilm (y=-$\left(\delta - L(t)\right)/2$):

$$\tau_w(x,t) = -\left(-\frac{dP}{dy}\right)\frac{8}{\pi^2}\sum_{n=1,3,\ldots}^{\infty}\frac{(-1)^{(n-1)/2}}{n^2}\tanh\left[\frac{n\pi\left(\delta - L(t)\right)}{2W}\right]\cos\left(\frac{n\pi x}{W}\right) \qquad (7.9)$$

Note that the above equation suggests that the shear-stress at the surface of the biofilm depends on the position in the x-direction (width). If we assume that the microchannel has high aspect ratio of $W/\left(\delta - L(t)\right)$ (>2.4), the equation simplifies to the following wall shear-stress relationship for parallel flow:

$$\tau_w(t) = \frac{6Q\mu}{W\left[\delta - L(t)\right]^2} \qquad (7.10)$$

7.3.1.3 Boundary Conditions

At the surface of the biofilm ($z = L(t)$), the mass fluxes of the limiting substrate and the QS signal are proportional to the difference in their mass densities at the biofilm surface and in the bulk flow. This can be written as,

$$n_{iz}\big|_{z=L} = k_i\left[\rho_i\big|_{z=L} - \rho_{i,bulk}\right] \qquad (7.11)$$

Here, k_i is the mass transfer coefficient, which, among other things, is dependent on the channel geometry, hydrodynamics, and properties of the liquid and the species. In the microchannels and for very low flow rates such as the ones used in this investigation (Reynolds Numbers < 1), the flow is fully developed within a few micrometers from the entrance. For fully developed laminar flows, and for the condition of uniform transport flux on one side with insulated walls on all other sides, researchers (71) have shown that

the dimensionless transfer coefficient (Nusselt number) for a similar problem is a function of only the duct geometry: the aspect ratio $\left(\delta - L(t)\right)/W$. Utilizing heat-mass transfer analogy, the numerical result for the condition of transport in a rectangular duct with three walls insulated and one at constant flux was approximated by the empirical formula:

$$\frac{4k_i r_H}{D_i} = \alpha_0 + \alpha_1\varepsilon + \alpha_2\varepsilon^2 + \alpha_3\varepsilon^3 + \alpha_4\varepsilon^4 \tag{7.12}$$

Here, D_i is the diffusion coefficient of the species i in the medium, $r_H(t)$ is the hydraulic radius, ε is the aspect ratio, α_is are parameters estimated from fitting the relationship to theoretical results (71). The above equation fits the theoretical results with an average error of 0.53%.

$$\varepsilon = \frac{\delta\text{-}L(t)}{W}; \quad r_H = \frac{W\left[\delta\text{-}L(t)\right]}{2\left[W + \delta\text{-}L(t)\right]} \tag{7.13}$$

W, δ and L(t) are the width, the initial height, and thickness of the biofilm, respectively. Due to impermeable substrate at the bottom surface (z = 0), the fluxes are essentially zero.

$$n_{iz}\big|_{z=0} = 0 \tag{7.14}$$

7.3.1.4 Reaction Rates

Eqs. (7.1)-(7.14) can be solved to investigate biofilm formation provided we have rate information r_i. We used information available for *P. aeruginosa* biofilm with acyl-HSL as the quorum sensing (QS) molecule. This is a well-investigated system for

which kinetics parameters are available. There are two non-diffusible species, active biomass (B) and inactive biomass (IB), and two diffusible species, O_2 and acyl-HSL (QS). The corresponding rates for active biomass, inert biomass, oxygen, and acyl-HSL are given here without the explanation of their forms (see Ref. (33) for more information).

$$r_B = \left[\left(Y_{B/O_2} V_{O_2} - \beta \right) \frac{\rho_{O_2}}{K_{O_2} + \rho_{O_2}} \right] \rho_B \tag{7.15}$$

$$r_{IB} = \left[\left(Y_{W/O_2} V_{O_2} + (1 - \varphi_D)\beta \right) \frac{\rho_{O_2}}{K_{O_2} + \rho_{O_2}} \right] \rho_B \tag{7.16}$$

$$r_{O_2} = -\left[\left(V_{O_2} + \varphi_D \beta \gamma \right) \frac{\rho_{O_2}}{K_{O_2} + \rho_{O_2}} \right] \rho_B \tag{7.17}$$

$$r_{QS} = \left[\frac{\varepsilon_1 \rho_{O_2}}{K_{O_2} + \rho_{O_2}} + \varepsilon_2 H\left(\rho_{QS} - \rho_{QS,0} \right) + \varepsilon_3 \right] \rho_B - \varepsilon_4 \rho_{QS} \tag{7.18}$$

The negative sign before the O_2 expression indicates that it is consumed. Monod kinetics with oxygen as the limiting substrate is used in the rate equations above. Equation (7.18) contains a term for natural degradation and uptake and step increase (H function) in production rate when quorum sensing is triggered for $\rho_{QS} > \rho_{QS,0}$. It must be noted that the overall conservation equation (Eq. 7.5) includes contributions from only the active and the inert biomass. This is due to the assumption that the contribution from densities and rates of oxygen and acyl-HSL are negligible compared to those of active biomass and inactive biomass. The model parameters and constant values used to solve the model and verify the results experimentally are summarized in **Table 7.1**.

7.3.1.5 Solution Methodology

The above system of non-linear parabolic equations constitutes a moving boundary problem, and after scaling the z-axis with the biofilm thickness, the equations were solved using an implicit tridiagonal finite difference scheme with a Newton-Raphson non-linear solver. It was found that the biofilm growth rate was substantially slower than the diffusion rates of the species and simulations were carried out by assuming pseudo-steady state conditions for O_2 and QS transport.

7.3.1.6 Parameter Sensitivity Analysis

In order to explain the apparent difference in the model predictions and the experimental observations, we carried out a parameter sensitivity analysis of biofilm growth. Since there are several parameters in the model, (**Table 7.1**) we focused our attention on the rate parameters: maximum oxygen consumption rate (V_{O2}), β, the diffusion coefficients of O_2 and acyl-HSL, the shear-stress constant, ξ_{max}, and the acyl-HSL production rate parameters: ε_1, ε_2, and ε_3. We varied the parameters by ±10% from their base value (**Table 7.1**) and assessed their effect on the stable biofilm thickness at a flow rate of 10nL/s.

Table 7.1: List of parameters used in simulation.[a]

Parameter	Value	Source
Width of the channel (W)	600 micrometers	Device
Depth of the channel (δ)	250 micrometers	Device
Mass transfer coefficient parameters (α's)		(71)
α_0	5.24209	
α_1	-5.22898	
α_2	3.99783	
α_3	-1.37114	
α_4	0.013118	
Biomass-oxygen yield coefficient, $Y_{B/O2}$	0.583 mg/mg O_2	
Maximum oxygen consumption rate, V_{O2}	8 mg oxygen/mg/day	
β	0.3 day^{-1}	
Michaelis constant, K_{O2}	$0.5x10^{-6}$ mg/mm^3	
Inactive biomass-oxygen yield coefficient, $Y_{W/O2}$	0.477 mg/mg O_2	
Biodegradable fraction of active biomass, ϕ_D	0.8	
γ	1.42 mg O_2/mg	
Acyl-HSL production rate parameters (ε's)		
ε_1	10^{-7} mg acyl-HSL/mg/day	
ε_2	10^{-3} mg acyl-HSL/mg/day	
ε_3	10^{-4} mg acyl-HSL/mg/day	
Acyl-HSL degradation and uptake facture, ε_4	0.693	
Initial fraction of active biomass	0.8	
Initial fraction of inactive biomass	0.2	
Density of active biomass	1.025 mg/mm^3	
Density of inactive biomass	1.0125 mg/mm^3	
Initial concentration of O_2, ρ_{O2} (t = 0, z)	0	
Initial concentration of acyl-HSL, ρ_{QS} (t = 0, z)	0	
Critical acyl-HSL concentration, $\rho_{QS,0}$	$6.7x10^{-9}$ mg/mm^3	
Bulk concentration of O_2, $\rho_{O2, bulk}$	$8.3x10^{-6}$ mg/mm^3	
Bulk concentration of acyl-HSL, $\rho_{QS, bulk}$	0	
Initial biofilm thickness L(t = 0)	3 micrometers	
Diffusivity of O_2 in biofilm/medium, D_{O2}	150 mm^2/day	
Diffusivity of acyl-HSL in biofilm/medium, D_{QS}	150 mm^2/day	
Maximum detachment rate, ξ_{max}	1.5 mm/day	(66, 107)
k_w	2.33 Pa^{-1}	(66, 107)

[a] All values are from (33), unless mentioned in source.

7.3.2 Experiments

7.3.2.1 Bacterial Strains and Media

Pseudomonas aeruginosa PA14 (55, 111) with plasmid pP25-GFPo (containing a *lacUV*5 promoter with an optimized Shine-Dalgarno sequence driving expression of the green fluorescent protein gene, (57)) was routinely cultured in Luria Bertani broth (LB) supplemented with 100 µg/mL of carbenicillin at 32°C with aeration. Biofilm experiments were performed using M63 minimal media (13.6 g/L KH_2PO_4, 2.0 g/L $(NH_4)_2SO_4$, 0.2 g/L $MgSO_4 \cdot 7\ H_2O$, 0.5 mg/L $FeSO_4 \cdot 7\ H_20$, 2.0 g/L glycerol, and KOH to make pH 7.0) (26) without carbenicillin.

7.3.2.2 Microfluidic Device Fabrication

Microfluidic devices were fabricated using a previously described procedure (144). Devices were designed in AutoCAD and a high resolution transparency mask was generated. The mask was used in 1:1 contact photolithography of SU-8 100 photoresist (Microchem, Newton, MA, USA) to create a negative master mold of approximately 250 µm high patterned photoresist on a 3" Silicon wafer. Positive replicas were fabricated by pouring PDMS (Slygard 184, Dow Corning, Midland, MI, USA) on the master and curing the PDMS. After removing the cured PDMS from the master, sharpened 20 gauge needles were used to punch inlet and outlet holes. The PDMS replica and a clean glass microscope slide (Thermo Fisher Scientific, Waltham, MA, USA) were treated with oxygen plasma for 30 s and then permanently bonded. Tygon

Microbore tubing was inserted into the inlet and outlet holes and connected to a Harvard Apparatus Pico Plus syringe pumps (Harvard Apparatus, Holliston, MA, USA). The device consists of two flow channels (600 µm wide, 250 µm high, 8000 µm long) and is shown in **Figure 7.2**.

7.3.2.3 Biofilm Experiments

The microfluidic biofilm reactor was disinfected using 50% ethanol for 5 min, followed by rinsing with LB medium to remove the excess ethanol. Devices were seeded with exponential-phase *P. aeruginosa* PA14 and incubated horizontally for 1 h at room temperature. The device was then flushed with M63 media at a flow rate of 800 nL/min for 30 min to remove unattached cells. The flow in the different channels was then switched to the flow rates being tested (2.3, 7.4, 21 nL/s) and the device placed vertically (inlet at the bottom and outlet at the top) in a 32^{o}C incubator. Fluorescence images at different positions along the biofilm depth were obtained at 24 and 48 h using a Leica TCS SP5 Confocal Laser Scanning Microscope (Bannockburn, IL, USA). Biofilm architecture was visualized using the IMARIS software as previously described (85, 86).

Figure 7.2: Schematic of the microfluidic model used for experimental investigation of biofilm thickness.

7.4 Results

7.4.1 Dynamics of Biofilm Thickness

To understand the dynamics of *P. aeruginosa* biofilm formation in confined microchannels, we simulated nutrient-dependent biofilm growth in a microfluidic chamber (**Figure 7.1**). In these simulations, the effects of local hydrodynamics on biofilm detachment and nutrient transport were included. **Figure 7.3A** shows plots of *P. aeruginosa* biofilm thickness as a function of time for different flow rates for a biofilm grown in a confined microchannel. The biofilm thickness increased with time initially but after some time the biofilm attained a stable thickness. This leveling off behavior was not observed for an open system (33). A stable biofilm thickness was obtained for medium flow rates up to a specific flow rate (1-11 nL/s) in the microchannel. For flow

rates greater than this critical flow rate (11 nL/s), new biofilm formation did not occur and even the imposed initial biofilm thickness reduced to zero. For stable biofilm formation, higher flow rate leads to a decrease in biofilm thickness and an increase in the time taken to reach the stable thickness.

Figure 7.3B shows a plot of the final stable biofilm thickness achieved and the corresponding wall shear-stress in the microchannel as a function of the flow rate in the microchannel. Stable *P. aeruginosa* biofilms are predicted to form for flow rates less than or equal to 11 nL/s. The results show that the stable biofilm thickness decreased with increase in flow rate up until the critical flow rate after which it becomes zero. The corresponding critical wall shear-stress within the channel at these flow rates also decreased until the critical flow rate after which it dropped to a lower value and started increasing with flow rate. Beyond the critical flow rate, there was no biofilm formation and the wall shear-stress value behaved the same way as that in an empty microchannel (**Figure 7.3B**).

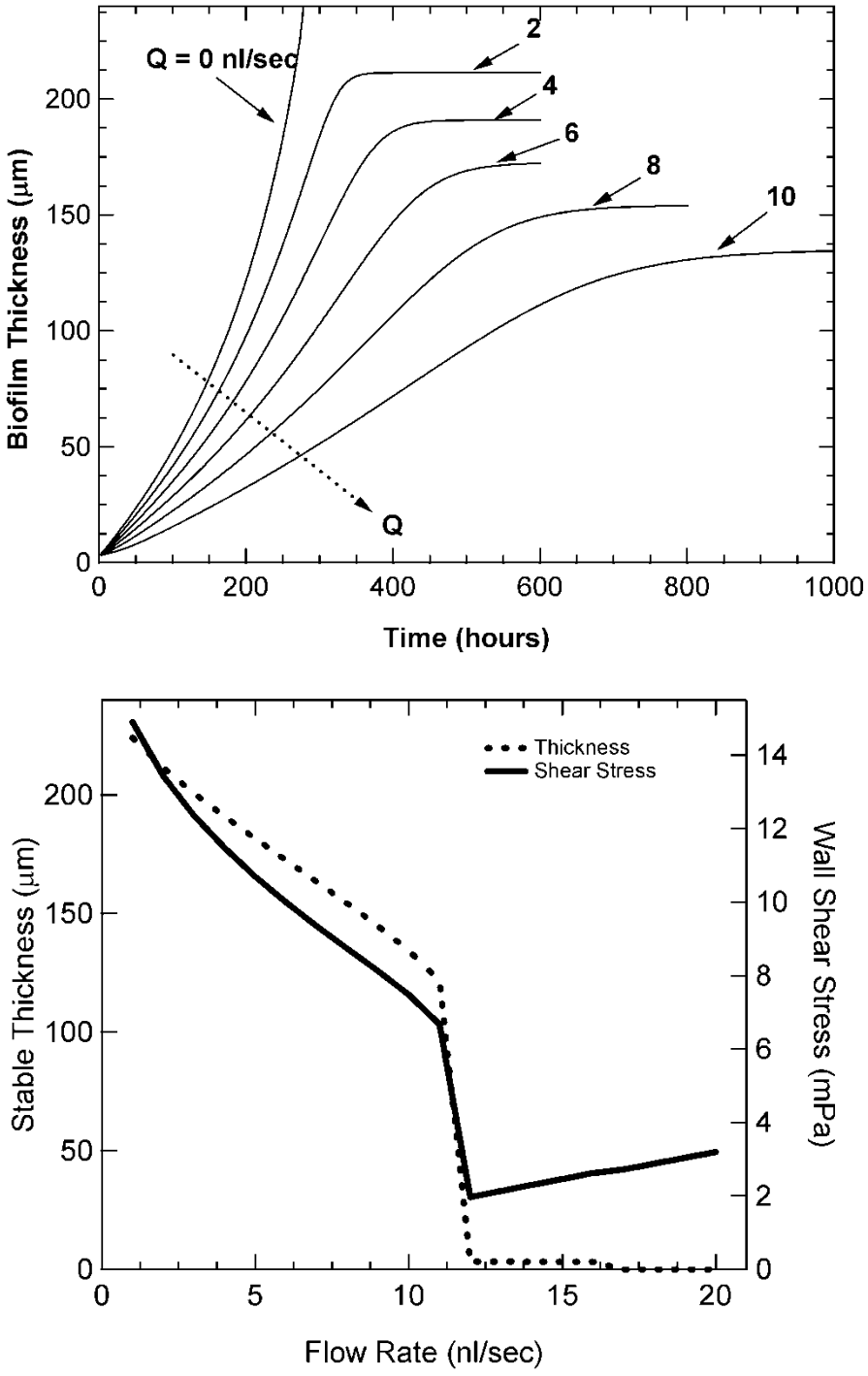

Figure 7.3: Model predictions for biofilm thickness. (A) Predicted relationship between biofilm thickness, flow rate, and time for biofilm development in the microfluidic biofilm model. (B) Relationship between biofilm thickness, wall shear stress, and flow rate.

7.4.2 Oxygen and QS levels

To study the effect of nutrients on biofilm growth dynamics and the latter on quorum sensing, we investigated the mass transport of oxygen and quorum sensing molecule in a growing biofilm through mathematical modeling. **Figures 7.4 (A** and **B)** show plots of normalized oxygen concentration in a biofilm growing in a microchannel at various time points for flow rates of 1 and 10 nL/s respectively. The results show that oxygen concentration increased with position in the biofilm from the bottom. Interestingly, even when the biofilm thickness was small, at initial time points, the entire biofilm had reduced oxygen levels. With time, the biofilm thickness increased, the oxygen levels in the biofilm near the interface between the medium and the biofilm increased, and the oxygen profiles became steeper. The oxygen levels decreased from a level of 0.6 (normalized to maximum level in the bulk solution) to a level of 0.1 within ~10 μm from the top of the biofilm. At the higher flow rate (10 nL/s), a similar behavior was observed although the oxygen levels were much lower in the biofilm; the levels decreased from a level of 0.2 to a level of 0.02 within ~10 μm from the top of the biofilm.

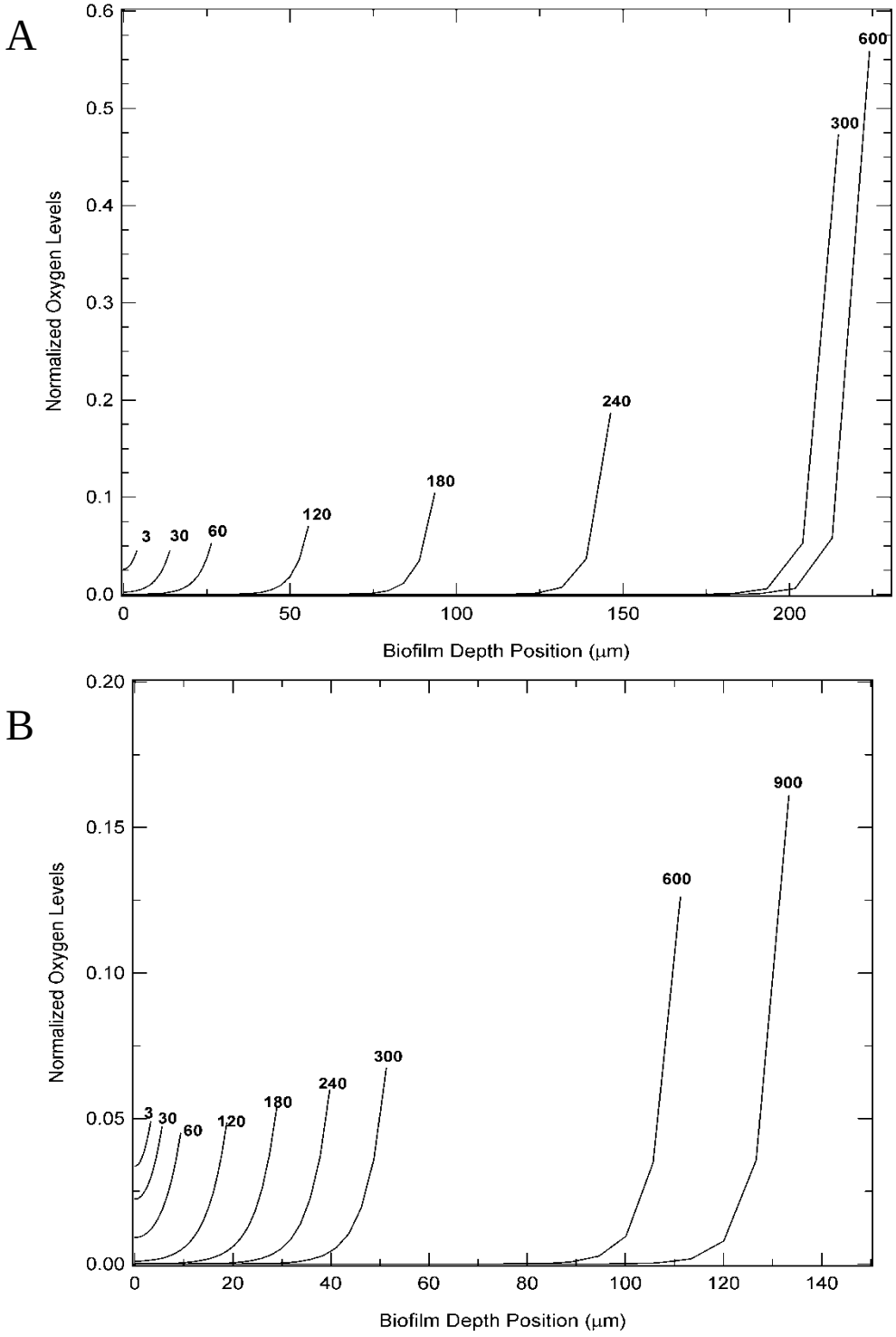

Figure 7.4: Model predictions for oxygen levels. Dissolved oxygen profiles in a biofilm at different depths and time of development at a flow rate of (A) 1 nL/s and (B) 10 nL/s.

Figure 7.5A & B show plots of normalized QS molecule (acyl-HSL) concentration within a growing biofilm in a microchannel at various time points for flow rates of 1 and 10 nL/s, respectively. The concentration levels were normalized to the critical level ($6.7x10^{-9}$ mg/mm^3) that induces quorum sensing in *P.aeruginosa*. The concentration of QS molecule decreased with biofilm depth position. The overall QS molecule levels increased with time. At the lower flow rate of 1 nL/s, and at 240 hours, the entire biofilm was just below the threshold level. With time, the concentration of QS molecule increased beyond the threshold level leading to quorum sensing, a step increase in the production (Eq. 7.18), and the level of QS molecule in the biofilm. This behavior, however, depended on the flow rate; at the higher flow rate of 10 nL/s, the QS molecule level in no part of the biofilm reached the threshold level. The results suggest that a critical biofilm depth/thickness is required for induction of QS in a growing biofilm. In both flow rates, the results show that stable levels of QS can be obtained.

In analyzing the fraction of stable biofilm that is QS active ($\rho_{QS}>\rho_{QS,crit}$) as a function of flow rate, we found that the activity of QS within a biofilm depended on the flow rate in a dichotomous way. For flow rates < 8 nL/s, at stable biofilm thicknesses, the entire film was 'quorum sensing active' ($\rho_{QS}>\rho_{QS,crit}$ everywhere). At flow rates > 7 nL/s, even when stable biofilm was formed, the QS molecule level never reached the threshold level.

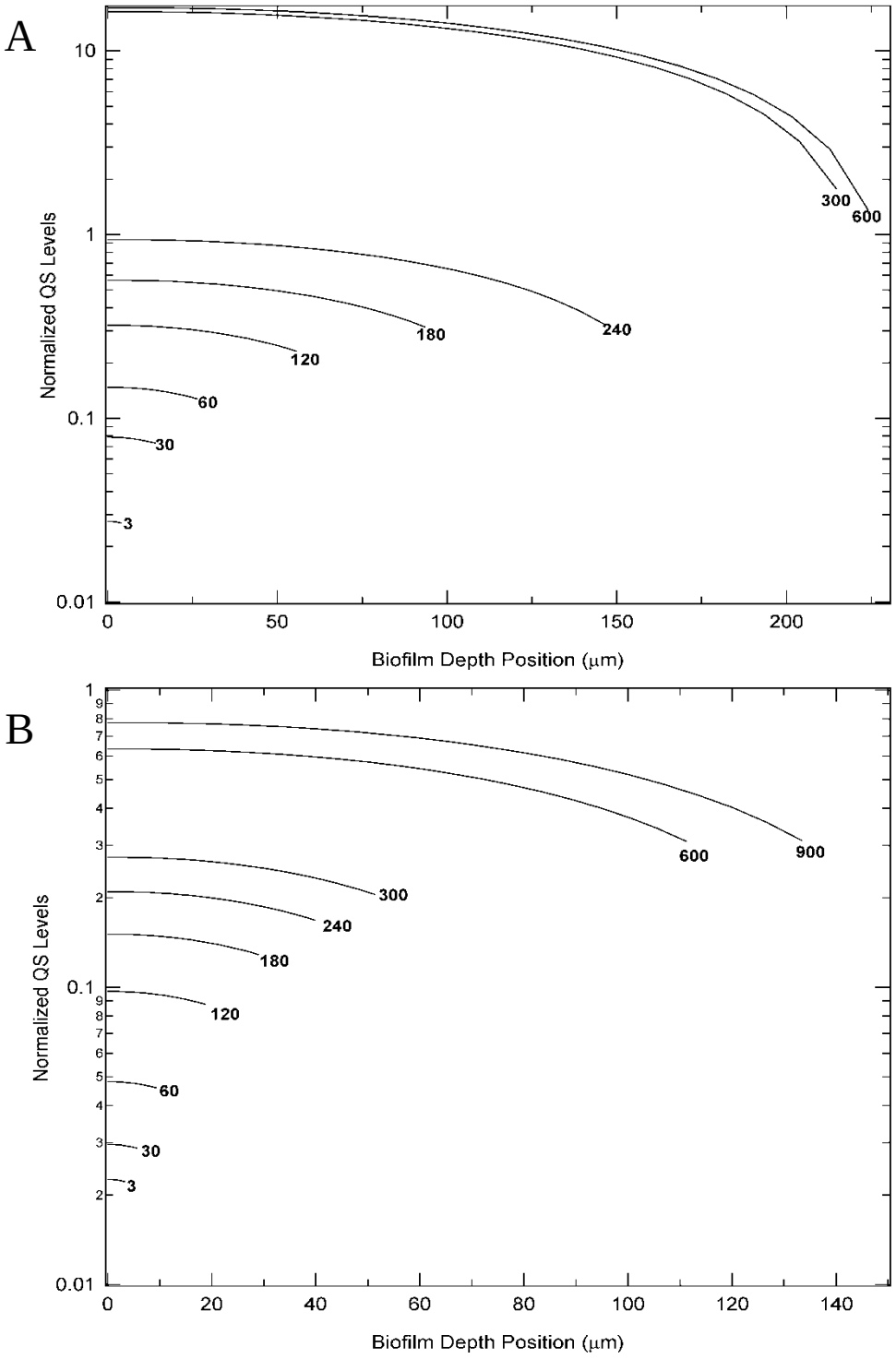

Figure 7.5: Model predictions for QS molecules. Distribution of quorum sensing molecule in a biofilm at different depths and time of development at a flow rate of (A) 1 nL/s and (B) 10 nL/s.

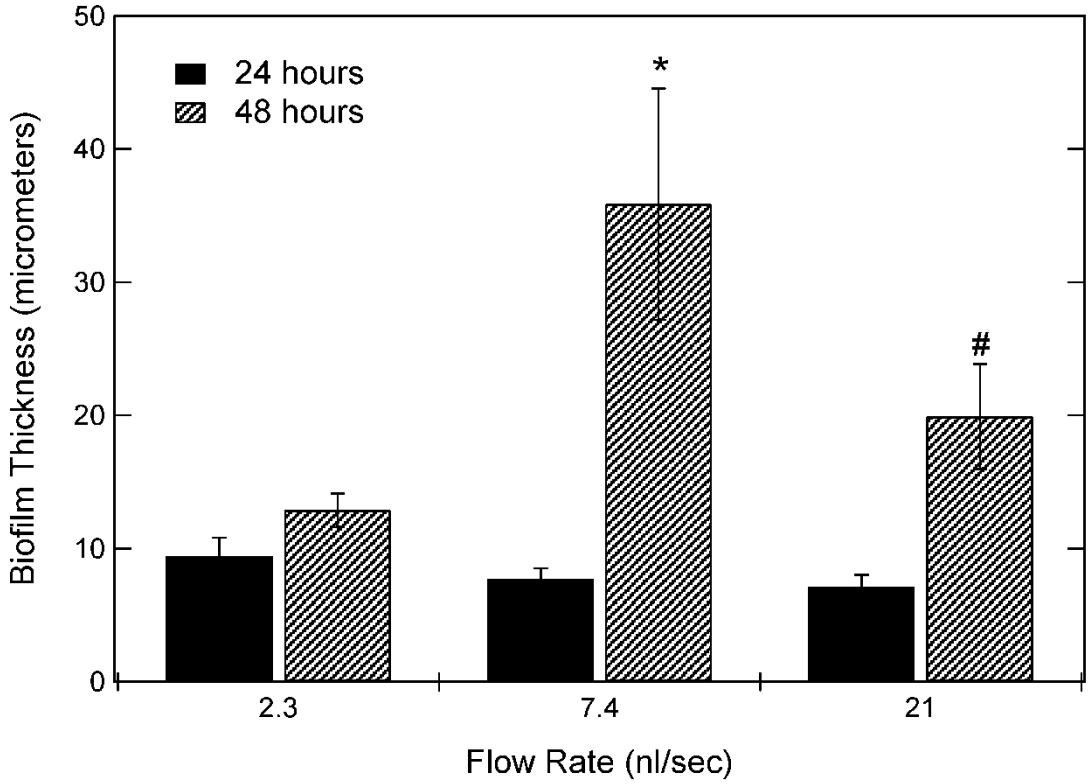

Figure 7.6: Experimental results for biofilm thickness. *P. aeruginosa* PA14 biofilm thickness at 24 and 48 h developed with flow rates of 2.3, 7.4, and 21 nL/s. Biofilm thickness was measured at three different locations in each chamber. Data shown are mean ± standard error of mean. * and # indicate statistically significant ($p < 0.0001$) difference between biofilm thickness at the low and medium, and medium and high flow rates, respectively.

7.4.3 Experimental Measurement of *P. aeruginosa* Biofilm Thickness

To verify model findings, biofilm reactors (**Figure 7.2**) were cultured with *P. aeruginosa* PA14 using three flow rates (2.3, 7.4, and 21 nL/s) that corresponded to the three flow regimes shown in **Figure 7.3B**. Biofilm thickness measurements were performed after 24 and 48 h of biofilm formation in microfluidic devices. The data (**Figure 7.6**) show that the biofilm thickness after 24 h was ~10 μm with little difference between the different flow rates. At 48 h, the biofilm thickness increased significantly (36 ± 9 μm) for the medium flow rate alone. Only a marginal increase in biofilm thickness (20 ± 4 μm) was observed with the high flow rate while no increase in thickness (13 ± 1 μm) was observed for the lowest flow rate used in the experiment (**Figure 7.6**). Since thickness measurement is only one aspect of biofilm structure, we further characterized the biofilm architecture using IMARIS software (**Figure 7.7**). Three-dimensional visualization of biofilms shows that the organization of the biofilm was significantly different at the different flow rates. At the lowest flow rate, the biofilm primarily consisted of small clusters of cells that were uniformly distributed throughout the biofilm (**Figure 7.7A**). At the intermediate flow rate (7.4 nL/s), the distribution of cell clusters was sparse but the clusters were taller (**Figure 7.7B**). The density of cell clusters was maximum at the highest flow rate tested (**Figure 7.7C**) but these clusters were significantly shorter than that observed with the intermediate flow rate. Together, the IMARIS visualization and the thickness measurements indicate the importance of flow rate in biofilm formation, both in terms of maximum stable thickness that can be obtained as well as the architecture of the resultant biofilm.

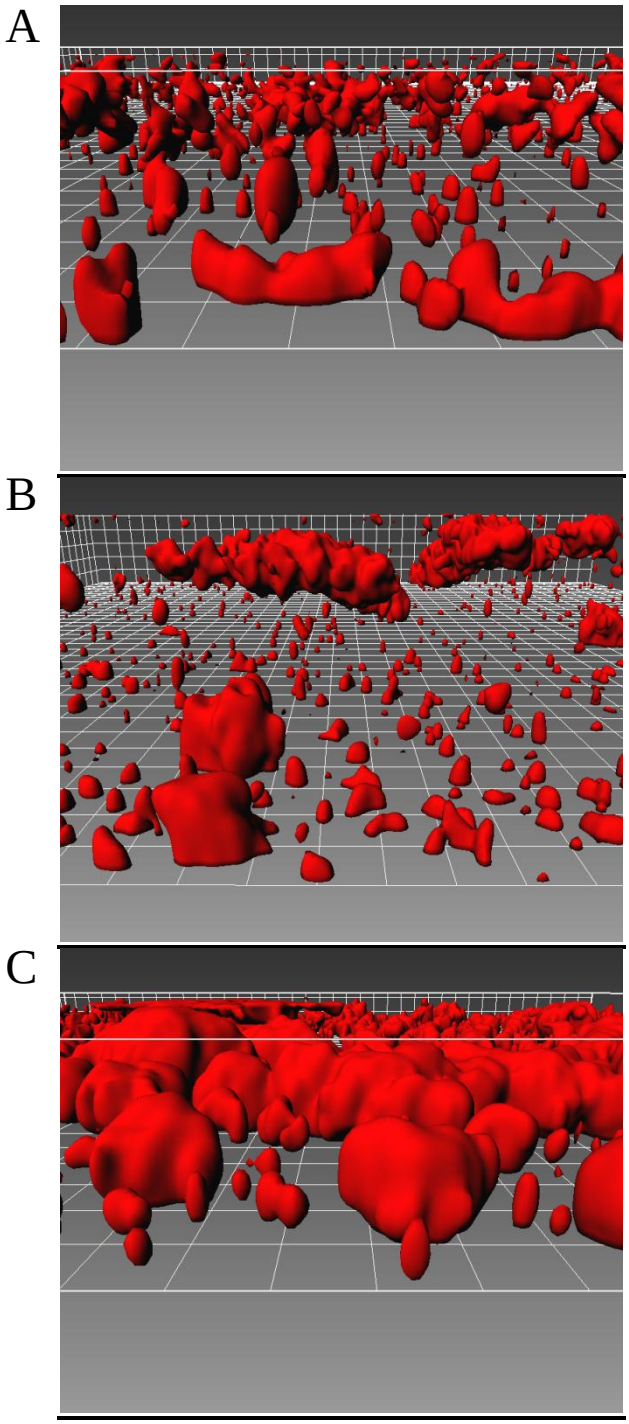

Figure 7.7: IMARIS representation of *P. aeruginosa* biofilms. Flow rates of (A) 2.3, (B) 7.4, and (C) 21 nL/s. The 3D views shown are representative of those obtained at three locations for each flow rate at 48 hours. Each square in the grid is 5 μm x 5 μm.

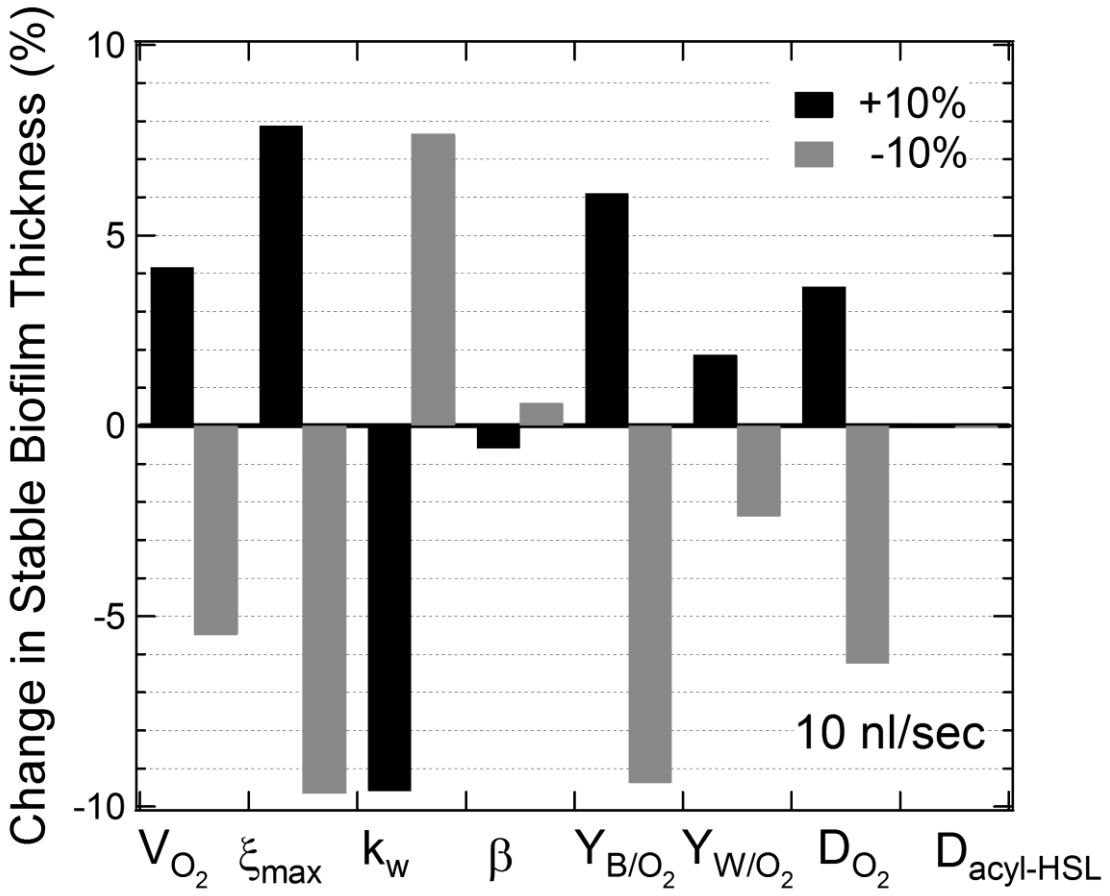

Figure 7.8: Parameter sensitivity analysis of biofilm thickness. We simulated biofilm growth dynamics by varying different model parameters by ±10% from the values listed in Table 7.1. Percent change in stable biofilm thickness observed is shown for various parameters. The flow rate was kept constant at 10 nL/s.

Figure 7.8 shows the results of parameter sensitivity analysis. Difference in the stable biofilm thickness is plotted for various parameters. The results show that the biofilm growth rate is significantly affected by the oxygen consumption rate. Note that the maximum oxygen consumption rate (V_{O_2}) is directly related to the biomass growth rate, and therefore Y_{B/O_2} also has a significant effect (Eq. 7.15). In addition, the maximum detachment rate (ξ_{max}) constant, and shear-stress constant (k_w) also have a significant effect on the stable biofilm thickness. The effect of diffusivity of oxygen is about the same as that of V_{O_2}. The effect of β, on the other hand is much smaller. As expected, the diffusivity and production rate parameters (ε_1, ε_2, and ε_3) of acyl-HSL have no effect at all on the biofilm thickness (only the diffusivity effect is shown).

7.5 Discussion

In this work, we carried out theoretical and experimental investigation of *P. aeruginosa* biofilms grown in confined microchannels. We studied the mutually-dependent effect of hydrodynamics on biofilm growth and vice versa. To our knowledge, to date, no such investigation has been carried out. Our key findings are that biofilms grown under flow conditions in a confined environment can attain stable thicknesses, the amount of stable biofilm formed depends on the hydrodynamics and mass transport conditions, and local hydrodynamics can be used to fine tune the QS activity of the biofilms.

When a biofilm is grown under confined flow conditions, the shear-dependent detachment rate and biofilm formation rate are two key factors that determine the net

growth rate of the biofilm. The biofilm formation rate itself is dependent on O_2 levels in the biofilm, which are in turn dependent on the mass transport of O_2 from the flowing medium to the biofilm. The latter increases as the channel depth in which the medium flow decreases due to increase in biofilm thickness with time. This is countered by the effect of shear-dependent detachment rate, which increases with wall shear-stress. The wall shear-stress itself increases with decrease in channel depth caused by biofilm formation in the device. The dynamics of biofilm thickness data obtained from simulation studies demonstrates this balance between biofilm detachment rate due to shear and biofilm formation (thickness and structure). This is experimentally evident from the biofilm thickness measurements (**Figure 7.6**) and the IMARIS visualization of biofilm structure under the different flow rates (**Figure 7.7**). Although biofilms developed at the lowest flow rate had the least thickness, a good degree of surface coverage was observed. This behavior is what would be expected if flow-induced shear were the sole determinant of biofilm formation. However, our data also show that the biofilm with the least area covered (i.e., at the intermediate flow rate) develops the most in terms of thickness after 48 h. This suggests that in addition to the shear effects, transport of nutrients is also important. At the lowest flow rate, nutrient transport limitation is more dominant than the low shear; as a result, the biofilm covers a large surface but does not increase in thickness. At the highest flow rate, shear effects likely offset the benefit of increased transport. The surface coverage is high because of increased transport with the higher flow rate but the biofilm thickness remains low due to increased shear effects. The medium flow rate likely represents an optimum between

shear-induced biofilm removal and growth arising from increased nutrient transport, having both the tallest structures and moderate coverage of the glass surface. Note that under fully-developed laminar flow conditions, theoretical analysis predicts mass transfer coefficient in ducts depends on the geometry and not the flow rate (71) (Eq. 7.12). This means that thinner biofilms lead to smaller aspect ratio, ε, and correspondingly smaller mass transfer coefficients. Lower flow rates also mean lower shear-dependent detachment rate. Although the above analysis suggests that biofilms can grow well under lower flow rates, it should be noted that the mathematical model does not take into account mass transfer limitations occurring downstream, *viz*, the bulk concentration of oxygen is assumed to be constant.

In the model development, we used a two-parameter empirical relationship (exponential dependence) between biofilm detachment rate and wall shear-stress. As there is no constitutive relationship available to describe this process, we used this relationship as a first step to describe the shear-dependent effect on biofilms. Sensitivity analysis of the parameters in the relationship showed that the parameters, and therefore the relationship do affect the biofilm thickness greatly (**Figure 7.8**). The parameters in this relationship were *estimated*; it is experimentally difficult to distinguish between shear-dependent and mass-transfer dependent biofilm detachment/growth.

The values of both the experimental and predicted growth rates of biofilm thickness in confined channels are about 50 (predicted) – 70% (experimental) of experimental values reported by Xu et al. (145), and about five times smaller than the predicted growth rate values of Chopp et al. (33). The probable reason for the

discrepancy between our values and that predicted by Chopp et al. (33) is that the model developed by latter was for an open system which led to significantly increased transport rates for oxygen at the surface of the biofilm. The model predictions of oxygen profile are consistent with experimental (112) and theoretical (33) findings of other researchers. The former also showed a substantial (~80%) decrease in oxygen levels from the 'bulk' solution to the surface of the biofilm. Our model predicts such a substantial (80-85%) reduction in oxygen levels and is more closely aligned with the experimental results than Chopp et al. (33).

An interesting finding in our results is that the flow rate greatly affects quorum sensing in the biofilm. At higher flow rates, the stable biofilm thickness is smaller, the amount of quorum sensing molecule produced is reduced, and the transport rate of the QS molecule out of the biofilm can be greater than the overall production rate. This leads to a QS molecule level within the film that does not trigger quorum sensing. It should be mentioned that this effect occurs even though the 'mass transfer coefficient' at higher flow rates is smaller than that at lower flow rates. At lower flow rates, the biofilm thickness is larger, the overall QS molecule production rate is greater than the removal rate, and with time, quorum sensing is triggered through the step function in Eq. (7.18). As molecular mechanisms underlying QS regulation, such as the coordinated use of multiple QS systems and QS-mediated communication in multi-species communities, are being identified (121), these can be incorporated into our model for further refining the model and improving its predictive capabilities.

A result from this work is that the model predictions with respect to the observed biofilm thickness at different flow rates are not consistent with the experimental results. This discrepancy can be attributed to the dynamics of biofilm development predicted by the model, as current kinetic models for biofilm modeling studies suffer from the lack of accurate parameters for describing biofilm development and growth. The kinetic parameters used in a majority of the models are based on growth measurements from nutrient rich media whereas biofilm experiments are done in nutrient limiting media. Therefore, it is possible that the use of non-optimal model parameters could be a reason for the lack of agreement between model predictions and experimental data. Results from the parameter sensitivity analysis indicate that kinetic parameters such as V_{O_2} and yield coefficient Y_{B/O_2} are relatively very important in determining biofilm thickness. Further, we used a simple model for shear-stress dependent detachment of biofilms. A more sophisticated model based on future information on bonding in biomass and biomass strength can lead to a more accurate prediction of experimental results.

A second limitation of the model is that the time scales for biofilm development predicted by the model are difficult to validate with experiments. While the model suggests that a stable biofilm with constant thickness can be developed, it predicts that this biofilm will take ~800 h to develop. It is difficult to validate the model predictions as practical considerations limit the duration over which experiments can be performed. First, plasmid stability is an issue as it is important that bacteria retain the GFP expression plasmid for the entire duration of the experiment. However, ensuring plasmid stability over 800 h is non-trivial. Second, clogging of the microfluidic channels

(especially with periodic shedding of biofilms) also precludes long-term (~800 h) experiments. It is expected that better selection of parameters can lead to a more accurate prediction of model development that is in agreement with experimental data. Further, it should be noted that the biofilm experiments were performed in minimal media and not nutrient-rich growth media. Thus, a non-oxygen nutrient (e.g., glucose) level could also affect the biofilm growth rate, especially at low flow rates. Currently, experiments are in progress to determine the effect of nutrient availability on *P. aeruginosa* biofilm thickness and distribution.

In summary, we carried out theoretical and experimental investigation of biofilms formed under confined flow conditions. Our results suggest the following:

- A balance between shear-dependent detachment rate and mass transport-dependent biofilm formation rate determines the biofilm thickness.
- Theoretical analysis suggests that for flow rates below a critical flow rate stable biofilm thickness can be achieved in the channel.
- Further, our results suggest that flow can be used to turn on or off quorum sensing within the biofilm.
- Experimental results validate model findings at flow rates greater than 7.4 nL/s but not at lesser flow rates.

These findings have importance in the investigation of mechanisms of biofilm formation and maintenance. Specifically, the ability to turn off quorum sensing can be used to investigate the role of this mechanism in biofilm formation.

CHAPTER VIII

CONCLUSIONS AND RECOMMENDATIONS

8.1 Conclusions

We developed three new chemotaxis models (Chapter III) that address the drawbacks of current methods used for investigating bacterial chemotaxis. The first method, the TFCA plug assay, made improvements on a previously described method by incorporating fluorescently-labeled protein to the bacteria for discriminating between movement due to chemotaxis and that due to bulk fluid movement. The second method, the μPlug assay, virtually eliminates bulk fluid movement allowing two different bacteria to be compared simultaneously. The μPlug assay also allows for longer experimental times by minimizing evaporation from the plug and surrounding cells. The third method, the μFlow chemotaxis device, creates stable concentration gradients under flow conditions for investigating bacterial chemotaxis. By controlling the flow conditions and the gradient strength, the extent of chemotactic migration can be precisely controlled in the μFlow chemotaxis device. Based on feedback and interest in collaborations, we anticipate the μFlow to have significant utility in bacterial chemotaxis studies.

We also investigated the effect of four major variables that influence the chemotactic behavior observed in the μFlow chemotaxis device (Chapter IV). These include process variables related to preparation of the motile bacterial population, the strength of the concentration gradient (i.e., the steepness), the flow rate used in the

device, and the position at which the extent of migration is measured. The importance of considering these variables while designing chemotaxis experiments has been demonstrated using migration of *E. coli* RP437 chemotaxis in Ni^{2+} concentration gradients.

We have used the μFlow device to investigate the response of *E. coli* RP437 to a broad range of canonical chemoeffectors such as *L*-aspartic acid and Ni^{2+}, as well as to putative mediators of GI tract infections such as AI-2 and indole (Chapters V & VI). We showed that the bacterial signal indole was a strong repellent, while AI-2 and isatin, another bacterial signal and a derivative of indole, are attractants. When *E. coli* RP437 are exposed to a combined gradient of both indole and AI-2, the bacteria are attracted even though indole is a much stronger repellent when exposed individually to *E. coli* RP437 (Chapter V). These results do not represent the GI tract, but merely a few of the complex gradients that may be present. This work demonstrates the ability to use the μFlow device for studying complex gradients as they are identified as chemotactically relevant.

The μFlow chemotaxis device has also been used to investigate the role for the nickel transport and binding proteins in the repellent response of *E. coli* RP437 to Ni^{2+}. We showed that the nickel binding protein, Nik A, and the Ni^{2+} transport system are not required for repellent chemotaxis to Ni^{2+} (Chapter VI), and the Tar chemoreceptor is likely to be the primary transducer used for sensing Ni^{2+}. This work is significant as it refutes a long-standing view on how Ni^{2+} is sensed by *E. coli* for chemotaxis (40).

A novel microfluidic model system for biofilm development inside a microfluidic system was discussed (Chapter VII). This model is the first to consider the effects of a developing biofilm on the hydrodynamics of biofilm formation in a closed channel such as the microfluidic device.

8.2 Recommendations

The μFlow device has significant potential for quantitatively investigating bacterial chemotaxis, especially repellent taxis. For studies investigating the mechanisms underlying bacterial chemotaxis, the ability to select mutants that behave differently than the wild type strain is very important. In other words, the ability to isolate a small fraction of the total population that exhibits a specific response is important. By making simple modifications to the μFlow chemotaxis device, it is possible to screen a population of cells for variants exhibiting a particular desired response. By using three (or more) outlets instead of the single outlet for the μFlow device, it is possible to isolate cells that exhibit different levels of response to the chemoeffector gradient. If the outlets are connected to collection tubes, the different cell populations can be collected and used for further analysis. These different fractions can also be passed through the sorting device multiple times to enrich a specific fraction.

A related application for the μFlow device is to select for high motility cells from a low-motility population. For example, unpublished data from our laboratory show that EHEC has lower motility than non-pathogenic *E. coli* strains, which hinders their use in chemotaxis studies. Based on our results (Chapter V) showing the bacteria in the

absence of a gradient spread evenly throughout the μFlow chemotaxis device, it is possible to select for mutants that migrate the farthest (i.e., spread the most distance). These selected bacteria can then be cultured, and sorted repeatedly until the desired motility is reached.

REFERENCES

1. **Abouhamad, W. N., and M. D. Manson.** 1991. Peptide transport and chemotaxis in *Escherichia coli* and *Salmonella typhimurium*: characterization of the dipeptide permease (Dpp) and the dipeptide-binding protein. Molecular Microbiology **5:**1035-1047.
2. **Abouhamad, W. N., and M. D. Manson.** 1994. The dipeptide permease of *Escherichia coli* closely resembles other bacterial transport systems and shows growth-phase-dependent expression Molecular Microbiology **14:**1077-1092.
3. **Adler, J.** 1966. Chemotaxis in bacteria. Science **153:**708-716.
4. **Adler, J.** 1973. A method for measuring chemotaxis and use of the method to determine optimum conditions for chemotaxis by *Escherichia coli*. Journal of General Microbiology **74:**77-91.
5. **Adler, J., and W.-W. Tso.** 1974. "Decision"-making in bacteria: chemotactic response of *Escherichia coli* to conflicting stimuli. Science **184:**1292-1294.
6. **Adler, J., G. L. Hazelbauer, and M. M. Dahl.** 1973. Chemotaxis toward sugars in *Escherichia coli*. Journal of Bacteriology **115:**824-847.
7. **Aksamit, R. R., and D. E. Koshland.** 1974. Identification of the ribose binding protein as the receptor for ribose chemotaxis in *Salmonella typhimurium*. Biochemistry **13:**4473-4478.
8. **Amsler, C. D.** 1996. Use of computer-assisted motion analysis for quantitative measurements of swimming behavior in peritrichously flagellated bacteria. Analytical Biochemistry **235:**20-25.

9. **Aneman, A., G. Eisenhofer, L. Olbe, J. Dalenbäck, P. Nitescu, L. Fändriks, and P. Friberg.** 1996. Sympathetic discharge to mesenteric organs and the liver. Evidence for substantial mesenteric organ norepinephrine spillover. The Journal of Clinical Investigation **97:**1640-1646.

10. **Aravind, L., and C. P. Ponting.** 1999. The cytoplasmic helical linker domain of receptor histidine kinase and methyl-accepting proteins is common to many prokaryotic signalling proteins. FEMS Microbiology Letters **176:**111-116.

11. **Armitage, J. P., and R. Schmitt.** 1997. Bacterial chemotaxis: *Rhodobacter sphaeroide* and *Sinorhizobium meliloti* - variations on a theme? Microbiology **143:**3671-3682.

12. **Baba, T., T. Ara, M. Hasegawa, Y. Takai, Y. Okumura, M. Baba, K. A. Datsenko, M. Tomita, B. L. Wanner, and H. Mori.** 2006. Construction of *Escherichia coli* K-12 in-frame, single-gene knockout mutants: the Keio collection. Molecular Systems Biology **2**.

13. **Bainer, R., H. Park, and P. Cluzel.** 2003. A high-throughput capillary assay for bacterial chemotaxis. Journal of Microbiological Methods **55:**315-319.

14. **Bansal, T., P. Jesudhasan, S. Pillai, T. K. Wood, and A. Jayaraman.** 2008. Temporal regulation of enterohemorrhagic *Escherichia coli* virulence mediated by autoinducer-2. Applied Microbiology and Biotechnology **78:**811-819.

15. **Bansal, T., D. Englert, J. Lee, M. Hegde, T. K. Wood, and A. Jayaraman.** 2007. Differential effects of epinephrine, norepinephrine, and indole on

Escherichia coli O157:H7 chemotaxis, colonization, and gene expression. Infection and Immunity **75:**4597-4607.

16. **Berg, H. C.** 1971. How to track bacteria. Review of Scientific Instruments **42:**868-871.
17. **Berg, H. C.** 1976. Does the flagellar rotary motor step?, p. A47-A56. *In* R. Goldman, T. Pollard, and J. Rosenbaum (ed.), Cold Spring Harbor Conferences on Cell Proliferation, Vol. 3: Cell Motility. Cold Spring Harbor Press, Cold Spring Harbor, NY.
18. **Berg, H. C.** 1993. Random Walks in Biology. Princeton University Press, Princeton, NJ.
19. **Berg, H. C.** 2005. Q&A Howard Berg. Current Biology **15:**R189-R190.
20. **Berg, H. C., and S. M. Block.** 1984. A miniature flow cell designed for rapid exchange of media under high-power microscope objectives. Journal of General Microbiology **130:**2915-2920.
21. **Berg, H. C., and D. A. Brown.** 1972. Chemotaxis in *Escherichia coli* analysed by three-dimensional tracking. Nature **239:**500-504.
22. **Block, S. M., J. E. Segall, and H. C. Berg.** 1982. Impulse responses in bacterial chemotaxis. Cell **31:**215-226.
23. **Block, S. M., J. E. Segall, and H. C. Berg.** 1983. Adaptation kinetics in bacterial chemotaxis. Journal of Bacteriology **154:**312-323.
24. **Brody, J. P., P. Yager, R. E. Goldstein, and R. H. Austin.** 1996. Biotechnology at low Reynolds numbers. Biophysical Journal **71:**3430-3441.

25. **Brown, D. A., and H. C. Berg.** 1974. Temporal stimulation of chemotaxis in *Escherichia coli*. Proceedings of the National Academy of Sciences of the United States of America **71:**1388-1392.

26. **Caiazza, N. C., and G. A. O'Toole.** 2004. SadB is required for the transition from reversible to irreversible attachment during biofilm formation by *Pseudomonas aeruginosa* PA14. Journal of Bacteriology **186:**4476-4485.

27. **Campbell, K., and A. Groisman.** 2007. Generation of complex concentration profiles in microchannels in a logarithmically small number of steps. Lab on a Chip **7:**264-272.

28. **Carter, A. O., A. A. Borczyk, J. A. Carlson, B. Harvey, J. C. Hockin, M. A. Karmali, C. Krishnan, D. A. Korn, and H. Lior.** 1987. A severe outbreak of *Escherichia coli* O157:H7--associated hemorrhagic colitis in a nursing home. The New England Journal of Medicine **317:**1496-1500.

29. **Characklis, W. G.** 1990. Microbial fouling, p. 523-84. *In* W. G. Characklis and K. C. Marshall (ed.), Biofilms. Wiley, New York, NY.

30. **Charlton, T., M. Givskov, R. Denys, J. B. Andersen, M. Hentzer, S. Rice, and S. Kjelleberg.** 2001. Genetic and chemical tools for investigating signaling processes in biofilms, p. 108-128. *In* R. J. Doyle (ed.), Microbial Growth in Biofilms Part A: Developmental and Molecular Biological Aspects, vol. 336. Academic Press, New York, NY.

31. **Chen, X., and H. C. Berg.** 2000. Torque-speed relationship of the flagellar rotary motor of *Escherichia coli*. Biophysical Journal **78:**1036-1041.

32. **Cheng, S. Y., S. Heilman, M. Wasserman, S. Archer, M. L. Shuler, and M. Wu.** 2007. A hydrogel-based microfluidic device for the studies of directed cell migration. Lab on a Chip **7:**763-769.

33. **Chopp, D. L., M. J. Kirisits, B. Moran, and M. R. Parsek.** 2002. A mathematical model of quorum sensing in a growing bacterial biofilm. Journal of Industrial Microbiology and Biotechnology **29:**339-346.

34. **Chopp, D. L., M. J. Kirisits, B. Moran, and M. R. Parsek.** 2003. The dependence of quorum sensing on the depth of a growing biofilm. Bulletin of Mathematical Biology **65:**1053-1079.

35. **Costerton, J. W., P. S. Stewart, and E. P. Greenberg.** 1999. Bacterial biofilms: a common cause of persistent infectons. Science **284:**1318-1322.

36. **Costerton, J. W., K.-J. Cheng, G. G. Geesey, T. I. Ladd, J. C. Nickel, M. Dasgupta, and T. J. Marrie.** 1987. Bacterial biofilms in nature and disease. Annual Review of Microbiology **41:**435-464.

37. **Cvikovitch, D. G., Y. H. Li, and R. P. Ellen.** 2003. Quorum sensing and biofilm formation in Streptococcal infections. The Journal of Clinical Investigation **112:**1626-1632.

38. **Dahlquist, F. W., P. Lovely, and D. E. Koshland.** 1972. Quantitative analysis of bacterial migration in chemotaxis. Nature: New Biology **236:**120-123.

39. **de Pina, K., V. Desjardin, M.-A. Mandrand-Berthelot, G. Giordano, and L.-F. Wu.** 1999. Isolation and characterization of the *nikR* gene encoding a nickel-responsive regulator in *Escherichia coli*. Journal of Bacteriology **181:**670-674.

40. **de Pina, K., C. Navarro, L. Mcwalter, D. H. Boxer, N. C. Price, S. M. Kelly, M. A. Mandrand-Berthelot, and L. F. Wu.** 1995. Purification and characterization of the periplasmic nickel-binding protein NikA of *Escherichia coli* K12. European Journal of Biochemistry **227:**857-865.

41. **Diao, J., L. Young, S. Kim, E. A. Fogarty, S. M. Heilman, P. Zhou, M. L. Shuler, M. Wu, and M. P. DeLisa.** 2006. A three-channel microfluidic device for generating static linear gradients and its application to the quantitative analysis of bacterial chemotaxis. Lab on a Chip **6:**381-388.

42. **Dockery, J. D., and J. P. Keener.** 2001. A mathematical model for quorum sensing in *Pseudomonas aeruginosa*. Bulletin of Mathematical Biology **63:**95-116.

43. **Dunten, P., and S. L. Mowbray.** 1995. Crystal structure of the dipeptide binding protein from *Escherichia coli* involved in active transport and chemotaxis. Protein Science **4:**2327-2334.

44. **Eguía, E., A. Trueba, A. Girón, B. Río-Calonge, F. Otero, and C. Bielva.** 2007. Optimisation of biocide dose as a function of residual biocide in a heat exchanger pilot plant effluent. Biofouling **23:**231-247.

45. **Eisenbach, M., A. Wolf, M. Welch, S. R. Caplan, I. R. Lapidus, R. M. Macnab, H. Aloni, and O. Asher.** 1990. Pausing, switching and speed fluctuation of the bacterial flagellar motor and their relation to motility and chemotaxis. Journal of Molecular Biology **211:**551-563.

46. **Englert, D. L., A. Jayaraman, and M. D. Manson.** 2009. Microfluidic Techniques for the Analysis of Bacterial Chemotaxis. *In* T. Jin and D. Herald (ed.), Chemotaxis, Methods and Protocols, vol. 571. Humana Press, Totowa, NJ.

47. **Englert, D. L., M. D. Manson, and A. Jayaraman.** 2009. Flow-based microfluidic device for quantifying bacterial chemotaxis in stable, competing gradients. Applied and Environmental Microbiology **75:**4557-4564.

48. **Farinas, J., A. W. Chow, and H. G. Wada.** 2001. A microfluidic device for measuring cellular membrane potential. Analytical Biochemistry **295:**138-142.

49. **Fenzen, P. D., A. Drake, and F. J. Angulo.** 2005. Economic cost of illness due to *Escherichia coli* O157 infections in the United States. Journal of Food Protection **68:**2623-2630.

50. **Flemming, H. C.** 2002. Biofouling in water systems – cases, causes and countermeasures. Applied Microbiology and Biotechnology **59:**629-640.

51. **Freestone, P. P., P. H. Williams, R. D. Haigh, A. F. Maggs, C. P. Neal, and M. Lyte.** 2002. Growth stimulation of intestinal commensal *Escherichia coli* by catecholamines: a possible contributory factor in trauma-induced sepsis. Shock **18:**465-470.

52. **Futrelle, R. P., and H. C. Berg.** 1972. Specification of gradients used for studies of chemotaxis. Nature **239:**517-518.

53. **Gardina, P. J., A. F. Bormans, and M. D. Manson.** 1998. A mechanism for simultaneous sensing of aspartate and maltose by the Tar chemoreceptor of *Escherichia coli*. Molecular Microbiology **29:**1147-1154.

54. **Gardina, P. J., C. Conway, M. Kossman, and M. D. Manson.** 1992. Aspartate and maltose-binding protein interact with adjacent sites in the Tar chemotactic signal transducer of *Escherichia coli*. Journal of Bacteriology **174:**1528-1536.

55. **Gill, R. K., S. Saksena, S. Tyagi, W. A. Alrefai, J. Malakooti, Z. Sarwar, J. R. Turner, K. Ramaswamy, and P. K. Dudeja.** 2005. Serotonin inhibits Na+/H+ exchange activity via 5-HT4 receptors and activation of PKC alpha in human intestinal epithelial cells. Gastroenterology **128:**962-974.

56. **Gonzalez Barrios, A. F., R. Zuo, Y. Hashimoto, L. Yang, W. E. Bentley, and T. K. Wood.** 2006. Autoinducer 2 controls biofilm formation in *Escherichia coli* through a novel motility quorum-sensing regulator (MqsR, B3022). Journal of Bacteriology **188:**305-316.

57. **Goodman, A. L., B. Kulasekara, A. Rietsch, D. Boyd, R. S. Smith, and S. Lory.** 2004. A signaling network reciprocally regulates genes associated with acute infection and chronic persistence in *Pseudomonas aeruginosa*. Developmental Cell **7:**745-754.

58. **Hansen, M. C., R. J. Palmer, Jr., C. Udsen, D. C. White, and S. Molin.** 2001. Assessment of GFP fluorescence in cells of *Streptococcus gordonii* under conditions of low pH and low oxygen concentration. Microbiology **147:**1383-1391.

59. **Harshey, R. M.** 1994. Bees aren't the only ones: swarming in gram-negative bacteria. Molecular Microbiology **13:**389-394.

60. **Hartl, D. L., and D. E. Dykhuizen.** 1984. The population genetics of *Escherichia coli*. Annual Review Genetics **18:**31-68.

61. **Hazelbauer, G. L.** 1975. Maltose chemoreceptor of *Escherichia coli*. Journal of Bacteriology **122:**206-214.

62. **Hazelbauer, G. L., and J. Adler.** 1971. Role of the galactose binding protein in chemotaxis of *Escherichia coli* toward galactose. Nature: New Biology **230:**101-104.

63. **Hazelbauer, G. L., R. E. Mesibov, and J. Adler.** 1969. *Escherichia coli* mutants defective in chemotaxis towards specific chemicals. Proceedings of the National Academy of Sciences of the United States of America **64:**1300-1307.

64. **Hegde, M., T. Wood, and A. Jayaraman.** 2009. The neuroendocrine hormone norepinephrine increases *Pseudomonas aeruginosa* PA14 virulence through the *las* quorum-sensing pathway. Applied Microbiology and Biotechnology (E-pub ahead of print).

65. **Hiles, I. D., L. M. Powell, and C. F. Higgins.** 1987. Peptide transport in *Salmonella typhimurium*: molecular cloning and characterization of the oligopeptide permease genes. Molecular and General Genetics **206:**101-109.

66. **Horn, H., H. Reiff, and E. Morgenroth.** 2003. Simulation of growth and detachment in biofilm systems under defined hydrodynamic conditions. Biotechnology and Bioengineering **81:**607-617.

67. **Horswill, A., P. Stoodley, P. Stewart, and M. Parsek.** 2007. The effect of the chemical, biological, and physical environment on quorum sensing in structured microbial communities. Analytical and Bioanalytical Chemistry **387:**371-380.

68. **Jarrell, K. F., and M. J. McBride.** 2008. The surprisingly diverse ways that prokaryotes move. Nature Reviews: Microbiology **6:**466-476.

69. **Jayaraman, A., and T. K. Wood.** 2008. Bacterial quorum sensing: signals, circuits, and implications for biofilms and disease. Annual Review of Biomedical Engineering **10:**145-167.

70. **Jeon, N. L., H. Baskaran, S. K. W. Dertinger, G. M. Whitesides, L. V. D. Water, and M. Toner.** 2002. Neutrophil chemotaxis in linear and complex gradients of interleukin-8 formed in a microfabricated device. Nature Biotechnology **20:**826-830.

71. **Kakac, S., R. K. Shah, and W. Aung.** 1987. Handbook of Single-Phase Convective Heat Transfer. John Wiley & Sons, New York, NY.

72. **Kaper, J. B., and V. Sperandio.** 2005. Bacterial cell-to-cell signaling in the gastrointestinal tract. Infection and Immunity **73:**3197-3209.

73. **Kaper, J. B., J. P. Nataro, and H. L. T. Mobley.** 2004. Pathogenic *Escherichia coli*. Nature Reviews: Microbiology **2:**123-139.

74. **Keenan, T. M., and A. Folch.** 2008. Biomolecular gradients in cell culture systems. Lab on a Chip **8:**34-57.

75. **Khan, S., K. Amoyaw, J. L. Spudich, G. P. Reid, and D. R. Trentham.** 1992. Bacterial chemoreceptor signaling probed by flash photorelease of a caged serine. Biophysical Journal **62:**67-68.

76. **King, K. R., S. Wang, D. Irimia, A. Jayaraman, M. Toner, and M. L. Yarmush.** 2007. A high-throughput microfluidic real-time gene expression living cell array. Lab on a Chip **7:**77-85.

77. **Kirisits, M. J., J. J. Margolis, B. L. Purevdorj-Gage, B. Vaughan, D. L. Chopp, P. Stoodley, and M. R. Parsek.** 2007. Influence of the hydrodynamic environment on quorum sensing in *Pseudomonas aeruginosa* biofilms. Journal of Bacteriology **189:**8357-8360.

78. **Koenig, D. W., and D. L. Pierson.** 1997. Microbiology of the space shuttle water system. Water Science Technology **35:**59-64.

79. **Koshland, D. E.** 1977. A response regulator model in a simple sensory system. Science **196:**1055-1063.

80. **Krikos, A., M. P. Conley, A. Boyd, H. C. Berg, and M. I. Simon.** 1985. Chimeric chemosensory transducers of *Escherichia coli*. Proceedings of the National Academy of Sciences of the United States of America **82:**1326-1330.

81. **Kuwajima, G.** 1988. Construction of a minimum-size functional flagellin of *Escherichia coli*. Journal of Bacteriology **170:**3305-3309.

82. **Lamanna, A. C., G. W. Ordal, and L. L. Kiessling.** 2005. Large increases in attractant concentration disrupt the polar localization of bacterial chemoreceptors. Molecular Microbiology **57:**774-785.

83. **Lanning, L. M., R. M. Ford, and T. Long.** 2008. Bacterial chemotaxis transverse to axial flow in a microfluidic channel. Biotechnology and Bioengineering **100:**653-663.

84. **Leclerc, H., D. A. A. Mossel, S. C. Edberg, and C. B. Struijk.** 2001. Advances in the bacteriology of the coliform group: their suitability as markers of microbial water safety. Annual Review of Microbiology **55:**201-234.

85. **Lee, J., A. Jayaraman, and T. K. Wood.** 2007. Indole is an inter-species biofilm signal mediated by SdiA. BMC Microbiology **7:**42.

86. **Lee, J., T. Bansal, A. Jayaraman, W. E. Bentley, and T. K. Wood.** 2007. Enterohemorrhagic *Escherichia coli* biofilms are inhibited by 7-hydroxyindole and stimulated by isatin. Applied and Environmental Microbiology **73:**4100-4109.

87. **Lewis, K.** 2001. Riddle of biofilm resistance. Antimicrobial Agents and Chemotherapy **45:**999-1007.

88. **Lyczak, J. B., C. L. Cannon, and G. B. Pier.** 2002. Lung infections associated with cystic fibrosis. Clinical Microbiology Reviews **15:**194-222.

89. **Lyte, M.** 2004. Microbial endocrinology and infectious disease in the 21st century. Trends in Microbiology **12:**14-20.

90. **Macnab, R. M., and D. E. Koshland.** 1972. The gradient-sensing mechanism in bacterial chemotaxis. Proceedings of the National Academy of Sciences of the United States of America **69:**2509-2512.

91. **Mah, T. F., B. Pitts, B. Pellock, G. C. Walker, P. S. Stewart, and G. A. O'Toole.** 2003. A genetic basis for *Pseudomonas aeruginosa* biofilm antibiotic resistance. Nature **426:**306-310.

92. **Manson, M. D., V. Blank, G. Brade, and C. F. Higgins.** 1986. Peptide chemotaxis in *E. coli* involves the Tap signal transducer and the dipeptide permease. Nature **321:**253-256.

93. **Mao, H., P. S. Cremer, and M. D. Manson.** 2003. A sensitive, versatile microfluidic assay for bacterial chemotaxis. Proceedings of the National Academy of Sciences of the United States of America **100:**5449-5454.

94. **McDonald, J. C., M. L. Chabinyc, S. J. Metallo, J. R. Anderson, A. D. Stroock, and G. M. Whitesides.** 2002. Prototyping of microfluidic devices in poly(dimethylsiloxane) using solid-object printing. Analytical Chemistry **74:**1537-1545.

95. **McGee, D. J., M. L. Langford, E. L. Watson, J. E. Carter, Y. T. Chen, and K. M. Ottemann.** 2005. Colonization and inflammation deficiencies in Mongolian gerbils infected by *Helicobacter pylori* chemotaxis mutants. Infection and Immunity **73:**1820-1827.

96. **Mesibov, R., and J. Adler.** 1972. Chemotaxis toward amino acids in *Escherichia coli*. Journal of Bacteriology **112:**315-326.

97. **Mitchell, P.** 2001. Microfluidics--downsizing large-scale biology. Nature Biotechnology **19:**717-721.

98. **Navarro, C., L. F. Wu, and M. A. Mandrand-Berthelot.** 1993. The *nik* operon of *Escherichia coli* encodes a periplasmic binding-protein-dependent transport system for nickel. Molecular Microbiology **9:**1181-1191.

99. **Nilsson, E., A. Amini, B. Wretlind, and A. Larsson.** 2007. *Pseudomonas aeruginosa* infections are prevented in cystic fibrosis patients by avian antibodies binding *Pseudomonas aeruginosa* flagellin Journal of Chromatography. B, Biomedical Applications **856:**75-80.

100. **O'Sullivan, D. J., and T. R. Klaenhammer.** 1993. High- and low-copy-number Lactococcus shuttle cloning vectors with features for clone screening. Gene **137:**227-231.

101. **O'Toole, G., H. B. Kaplan, and R. Kolter.** 2000. Biofilm formation as microbial development. Annual Review of Microbiology **54:**49-79.

102. **Parkinson, J. S.** 2007. A "bucket of light" for viewing bacterial colonies in soft agar, p. 432-435. *In* M. I. Simon, B. R. Crane, and A. Crane (ed.), Two-Component Signaling Systems, Part B, vol. 423. Academic Press, New York, NY.

103. **Parkinson, J. S., and S. E. Houts.** 1982. Isolation and behavior of *Escherichia coli* deletion mutants lacking chemotaxis functions. Journal of Bacteriology **151:**106-113.

104. **Parkinson, J. S., P. Ames, and C. A. Studdert.** 2005. Collaborative signaling by bacterial chemoreceptors. Current Opinion in Microbiology **8:**116-21.

105. **Parsek, M. R., and E. P. Greenberg.** 2005. Sociomicrobiology: the connections between quorum sensing and biofilms. Trends in Microbiology **13:**27-33.

106. **Parsek, M. R., and P. K. Singh.** 2003. Bacterial biofilms: An emerging link to disease pathogenesis. Annual Review of Microbiology **57:**677-701.

107. **Patel, A., G. Nakhla, and J. Zhu.** 2005. Detachment of multi species biofilm in circulating fluidized bed bioreactor. Biotechnology and Bioengineering **92:**427-437.

108. **Picioreanu, C., M. C. M. van Loosdrecht, and J. J. Heijnen.** 2001. Two-dimensional model of biofilm detachment caused by internal stress from liquid flow. Biotechnology and Bioengineering **72:**205-218.

109. **Polson, N. A., and M. A. Hayes.** 2001. Microfluidics: controlling fluids in small places. Analytical Chemistry **73:**312A-319A.

110. **Purcell, E. M.** 1977. Life at low Reynolds number. American Journal of Physics **45:**3-11.

111. **Rahme, L. G., E. J. Stevens, S. F. Wolfort, J. Shao, R. G. Tompkins, and F. M. Ausubel.** 1995. Common virulence factors for bacterial pathogenicity in plants and animals. Science **268:**1899-1902.

112. **Rasmussen, K., and Z. Lewandowski.** 1998. Microelectrode measurements of local mass transport rates in heterogeneous biofilms. Biotechnology and Bioengineering **59:**302-309.

113. **Saadi, W., S. Rhee, F. Lin, B. Vahidi, B. Chung, and N. Jeon.** 2007. Generation of stable concentration gradients in 2D and 3D environments using a microfluidic ladder chamber. Biomedical Microdevices **9:**627-635.

114. **Scharf, B. E., K. A. Fahrner, L. Turner, and H. C. Berg.** 1998. Control of direction of flagellar rotation in bacterial chemotaxis. Proceedings of the National Academy of Sciences of the United States of America **95:**201-206.

115. **Shioi, J., C. V. Dang, and B. L. Taylor.** 1987. Oxygen as attractant and repellent in bacterial chemotaxis. Journal of Bacteriology **169:**3118-3123.

116. **Silverman, M., and M. Simon.** 1974. Flagellar rotation and the mechanism of bacterial motility. Nature **249:**73-74.

117. **Singh, P. K., A. L. Schaefer, M. R. Parsek, T. O. Moninger, M. J. Welsh, and E. P. Greenberg.** 2000. Quorum-sensing signals indicate that cystic fibrosis lungs are infected with bacterial biofilms. Nature **407:**762-764.

118. **Springer, M. S., M. F. Goy, and J. Adler.** 1977. Sensory transduction in *Escherichia coli*: a requirement for methionine in sensory adaptation. Proceedings of the National Academy of Sciences of the United States of America **74:**183-187.

119. **Stocker, R., J. R. Seymour, A. Samadani, D. E. Hunt, and M. F. Polz.** 2008. Rapid chemotactic response enables marine bacteria to exploit ephemeral microscale nutrient patches. Proceedings of the National Academy of Sciences of the United States of America **105:**4209-4214.

120. **Stroock, A. D., S. K. W. Dertinger, A. Ajdari, I. Mezic, H. A. Stone, and G. M. Whitesides.** 2002. Chaotic mixer for microchannels. Science **295:**647-651.

121. **Taga, M. E., and B. L. Bassler.** 2003. Chemical communication among bacteria. Proceedings of the National Academy of Sciences of the United States of America **100:**14549-14554.

122. **Tarr, P. I., C. A. Gordon, and W. L. Chandler.** 2005. Shiga-toxin-producing *Escherichia coli* and haemolytic uraemic syndrome Lancet **365:**1073-1086.

123. **Thompson, D. M., K. R. King, K. J. Wieder, M. Toner, M. L. Yarmush, and A. Jayaraman.** 2004. Dynamic gene expression profiling using a microfabricated living cell array. Analytical Chemistry **76:**4098-4103.

124. **Tso, W.-W., and J. Adler.** 1974. Negative chemotaxis in *Escherichia coli*. Journal of Bacteriology **118:**560-576.

125. **van Loosdrecht, M. C. M., J. J. Heijnen, H. Eberl, J. Kreft, and C. Picioreanu.** 2002. Mathematical modelling of biofilm structures. Antonie Van Leeuwenhoek **81:**245-256.

126. **van Loosdrecht, M. C. M., D. Eikelboom, A. Gjaltema, A. Mulder, L. Tijhuis, and J. J. Heijnen.** 1995. Biofilm structures. Water Science Technology **32:**35-43.

127. **Viretta, A. U., and M. Fussenegger.** 2004. Modeling the quorum sensing regulatory network of human- pathogenic *Pseudomonas aeruginosa*. Biotechnology Progress **20:**670-678.

128. **Wadhams, G. H., and J. P. Armitage.** 2004. Making sense of it all: bacterial chemotaxis. Nature Reviews: Molecular Cell Biology **5:**1024-1037.

129. **Walker, G. M., N. Monteiro-Riviere, J. Rouse, and A. T. O'Neill.** 2007. A linear dilution microfluidic device for cytotoxicity assays. Lab on a Chip **7:**226-232.

130. **Wang, J.** 2002. On-chip enzymatic assays. Electrophoresis **23:**713-718.

131. **Wang, L., Y. Hashimoto, C. Y. Tsao, J. J. Valdes, and W. E. Bentley.** 2005. Cyclic AMP (cAMP) and cAMP receptor protein influence both synthesis and uptake of extracellular autoinducer 2 in *Escherichia coli*. Journal of Bacteriology **187:**2066-2076.

132. **Ward, J. P., J. R. King, A. J. Koerber, J. M. Croft, R. E. Sockett, and P. Williams.** 2003. Early development and quorum sensing in bacterial biofilms. Journal of Mathematical Biology **47:**23-55.

133. **Ward, J. P., J. R. King, A. J. Koerber, P. Williams, J. M. Croft, and R. E. Sockett.** 2001. Mathematical modelling of quorum sensing in bacteria. IMA Journal of Mathematics Applied in Medicine and Biology **18:**263-292.

134. **Waters, C. M., and B. L. Bassler.** 2005. Quorum sensing: cell-to-cell communication in bacteria. Annual Review of Cell and Developmental Biology **21:**319-346.

135. **Watnick, P., and R. Kolter.** 2000. Biofilm, city of microbes. Journal of Bacteriology **182:**2675-2679.

136. **Wieder, K. J., K. R. King, D. M. Thompson, C. Zia, M. L. Yarmush, and A. Jayaraman.** 2005. Optimization of reporter cells for expression profiling in a microfluidic device. Biomedical Microdevices **7:**213-222.

137. **Willcox, M. D., H. Zhu, T. C. Conibear, E. B. Hume, M. Givskov, S. Kjelleberg, and S. A. Rice.** 2008. Role of quorum sensing by *Pseudomonas aeruginosa* in microbial keratitis and cystic fibrosis. Microbiology **154:**2184-2194.

138. **Williams, S. M., Y. T. Chen, T. M. Andermann, J. E. Carter, D. J. McGee, and K. M. Ottemann.** 2007. *Helicobacter pylori* chemotaxis modulates inflammation and bacterium-gastric epithelium interactions in infected mice. Infection and Immunity **75:**3747-3757.

139. **Winans, S. C., and B. L. Bassler.** 2002. Mob psychology. Journal of Bacteriology **184:**873-883.

140. **Wolfe, A. J., and H. C. Berg.** 1989. Migration of bacteria in semisolid agar. Proceedings of the National Academy of Sciences of the United States of America **86:**6973-6977.

141. **Wong, C. S., S. Jelacic, R. L. Habeeb, S. L. Watkins, and P. I. Tarr.** 2000. The risk of the hemolytic-uremic syndrome after antibiotic treatment of *Escherichia coli* O157:H7 infections. The New England Journal of Medicine **342:**1930-1936.

142. **Wu, L. F., and M. A. Mandrand-Berthelot.** 1995. A family of homologous substrate-binding proteins with a broad range of substrate specificity and dissimilar biological functions. Biochimie **77:**744-750.

143. **Xavier, K. B., and B. L. Bassler.** 2005. Regulation of uptake and processing of the quorum-sensing autoinducer AI-2 in *Escherichia coli*. Journal of Bacteriology **187:**238-248.

144. **Xia, Y. N., and G. M. Whitesides.** 1998. Soft lithography. Annual Review of Materials Science **28:**153-184.

145. **Xu, K. D., P. S. Stewart, F. Xia, C. T. Huang, and G. A. McFeters.** 1998. Spatial physiological heterogeneity in *Pseudomonas aeruginosa* biofilm is determined by oxygen availability. Applied and Environmental Microbiology **64:**4035-4039.

146. **Yu, H. S., and M. Alam.** 1997. An agarose-in-plug bridge method to study chemotaxis in the Archaeon *Halobacterium salinarum*. FEMS Microbiology Letters **156:**265-269.

APPENDIX

MATLAB CODE

```
function centroid_chemotaxis_bg_7(thresh, slice_len)
dd = dir('images/to_process/');
if (length(dd) > 2)
    for i = 1 : length(dd)
        if ((~strcmp(dd(i).name, '.')) && (~strcmp(dd(i).name, '..')) && (dd(i).isdir == 1))
            %       elseif strcmp(dd(i).name, '..')
            %      else
            %          dd(i).isdir
            %         if dd(i).isdir == 1
            dd(i).name


            % Set Names
            dir1 = strcat('images/output - No BG/', dd(i).name, '/');
            dir2 = strcat('images/to_process/', dd(i).name, '/');
            mkdir('images/output - No BG/', dd(i).name);
            dd2 = dir(dir2);
            for j = 1 : length(dd2)
                if ((~strcmp(dd2(j).name, '.')) && (~strcmp(dd2(j).name, '..')) && (dd2(j).isdir
                    == 1))
```

```
                mkdir(dir1, dd2(j).name);
                out_path = strcat(dir1, dd2(j).name, '/');
                in_path = strcat(dir2, dd2(j).name, '/');
                if length(dir(dir2)) > 2
                    centroid_chemotaxis(thresh, slice_len, in_path, out_path);
                end
            end
        end
    end
end
end


function centroid_chemotaxis(thresh, slice_len, in_path, out_path)
%This version of the chemotaxis program will analyze all the pictures in a series
%and create ONLY 1 output file for the profile
%Thresh hold limit (0.0 - 1.0)

code_version{1} = 'Version 4.0';
slices = 1;
%    if length(varargin) >= 1
```

```
if ((thresh > 1.0) || (thresh < 0.0))
   ['************************************************';
      '*                                              *'
      '*        Program Operation Aborted!!           *';
      '*    Threshold must be between 0.0 and 1.0     *';
      '*                                              *'
      '************************************************']
   return;
end


sec_pic = 1;
bg_amt = [1, 3, 5];


grn_img_list = dir(strcat(in_path, 'green/*ch00.tif'));
red_img_list = dir(strcat(in_path, 'red/*ch01.tif'));
%    bg_per = 0.65;  %Background percentage (0.0 - 1.0)
grn_path = strcat(in_path, 'green/');
red_path = strcat(in_path, 'red/');
distro = [];
summed = [];
```

```
%Gets the image information from the image list
img_info = grn_img_list(1);

%Gets the various parts from the filename (in this case path and versn are placeholders)
[path, name, ext, versn] = fileparts(img_info.name)
%Adds the correct path to the image relative to the working directory
img_name = fullfile(grn_path,img_info.name);

%Gets the Base Name for Use in Output File Name
name_end = length(name) - 9;
base_name = name(1 : name_end);


%Loads the image
image = imread(img_name);

%Gets the size of the image
[r_max,c_max]=size(image);

increments = 0;
bg_perc = 1.01;
```

```
for amt = 1 : length(bg_amt)

    grn_path
    grn_img_list
    thresh
    centroid_array = Remove_BG2(grn_path, grn_img_list, thresh, bg_amt(amt));
    red_centroid_array = Remove_BG2(red_path, red_img_list, thresh, bg_amt(amt));

    %Sums up the rows by calling the y_sum function
    grn_sum = sum(centroid_array)';
    red_sum = sum(red_centroid_array)';

    grn_distr = Slice_Centroid(grn_sum', slice_len);
    red_distr = Slice_Centroid(red_sum', slice_len);


%%%
```

```
    %   Calculating the Mean and Standard Deviation as well as the Chemotaxis
Coefficients  %
    %                                                                    %
%%%
```

```
%%%
```

```
    stdev_red_s_sum = 0;
    for gs = 1 : length(grn_s)
        stdev_grn_s_sum = stdev_grn_s_sum + (grn_s(gs) * ((gs - mean_grn_s) .^ 2));
        stdev_red_s_sum = stdev_red_s_sum + (red_s(gs) * ((gs - mean_red_s).^ 2));

        %Calculating the Chemotaxis Stats Coefficients for Summed Data
        grn_s_chemo_stats = chemo_coef(grn_s, mean_grn_s, mean_red_s);
        red_s_chemo_stats = chemo_coef(red_s, mean_red_s, mean_red_s);
    end

    stdev_grn_s = ((stdev_grn_s_sum / grn_s_sum) .^ (0.5));    %Standard Deviation for
Summed Pixels
    stdev_red_s = ((stdev_red_s_sum / red_s_sum) .^ (0.5));    %Standard Deviation for
Summed Pixels

    %%%%%%%%%%%%%%%%%%%%%%%%%%%%%%%%%%%%%%%%%%%%%%%%%%%%%%%%%%%%%%%%%%%%%%%
    % This section is for the sliced images %
    %%%%%%%%%%%%%%%%%%%%%%%%%%%%%%%%%%%%%%%%%%%%%%%%%%%%%%%%%%%%%%%%%%%%%%%

    %Calculating Sums for Mean Calculation Below
    for gd = 1 : length(grn_d)
        mean_grn_d_sum = mean_grn_d_sum + (gd * grn_d(gd));
```

```
    mean_red_d_sum = mean_red_d_sum + (gd * red_d(gd));
    grn_d_sum = grn_d_sum + grn_d(gd);
    red_d_sum = red_d_sum + red_d(gd);
  end

  mean_grn_d = mean_grn_d_sum / grn_d_sum;    %Mean for Summed Pixels
  mean_red_d = mean_red_d_sum / red_d_sum;    %Mean for Summed Pixels

  %Calculate the Standard Deviation
  stdev_grn_d_sum = 0;
  stdev_red_d_sum = 0;
  for gd = 1 : length(grn_d)
    stdev_grn_d_sum = stdev_grn_d_sum + (grn_d(gd) * ((gd - mean_grn_d) .^ 2));
    stdev_red_d_sum = stdev_red_d_sum + (red_d(gd) * ((gd - mean_red_d) .^ 2));

    %Calculating the Chemotaxis Stats Coefficients for Sliced Data
    grn_d_chemo_stats = chemo_coef(grn_d, mean_grn_d, mean_red_d);
    red_d_chemo_stats = chemo_coef(red_d, mean_red_d, mean_red_d);
  end

  stdev_grn_d = ((stdev_grn_d_sum / grn_d_sum) .^ (0.5));    %Standard Deviation for
Summed Pixels
```

```
    stdev_red_d = ((stdev_red_d_sum / red_d_sum) .^ (0.5));    %Standard Deviation for
Summed Pixels

%%%
```

```
%Output for Summed Red Stats
stats_red_s(1) = mean_red_s;
stats_red_s(2) = stdev_red_s;
stats_red_s(3) = mean_red_s - (3 * stdev_red_s);
stats_red_s(4) = mean_red_s - (2 * stdev_red_s);
stats_red_s(5) = mean_red_s - stdev_red_s;
stats_red_s(6) = mean_red_s;
stats_red_s(7) = mean_red_s + stdev_red_s;
stats_red_s(8) = mean_red_s + (2 * stdev_red_s);
stats_red_s(9) = mean_red_s + (3 * stdev_red_s);

%Output for Sliced Green Stats
stats_grn_d(1) = mean_grn_d;
stats_grn_d(2) = stdev_grn_d;
stats_grn_d(3) = mean_grn_d - (3 * stdev_grn_d);
stats_grn_d(4) = mean_grn_d - (2 * stdev_grn_d);
stats_grn_d(5) = mean_grn_d - stdev_grn_d;
stats_grn_d(6) = mean_grn_d;
stats_grn_d(7) = mean_grn_d + stdev_grn_d;
stats_grn_d(8) = mean_grn_d + (2 * stdev_grn_d);
stats_grn_d(9) = mean_grn_d + (3 * stdev_grn_d);
```

```
%Output for Sliced Red Stats

stats_red_d(1) = mean_red_d;

stats_red_d(2) = stdev_red_d;

stats_red_d(3) = mean_red_d - (3 * stdev_red_d);

stats_red_d(4) = mean_red_d - (2 * stdev_red_d);

stats_red_d(5) = mean_red_d - stdev_red_d;

stats_red_d(6) = mean_red_d;

stats_red_d(7) = mean_red_d + stdev_red_d;

stats_red_d(8) = mean_red_d + (2 * stdev_red_d);

stats_red_d(9) = mean_red_d + (3 * stdev_red_d);


%%%
```

```
    chemo_red_distr = red_d_chemo_stats';

    stats_row_header = {'Mean'; 'Stnd Dev'; '-3 St Dev'; '-2 St Dev'; '-1 St Dev'; 'Mean';
'+1 St Dev'; '+2 St Dev'; '+3 St Dev'};
    chemo_row_header = {'Shift'; 'Pixel Count'; 'CPC'; 'CMC'};

    grn_summed = grn_sum;
    red_summed = red_sum;
    grn_distrd = grn_distr';
    red_distrd = red_distr';

    summed = cat(2, grn_summed, red_summed);
    distro = cat(2, grn_distrd, red_distrd);
    stats_summed = cat(2, stats_grn_sum, stats_red_sum);
    stats_distro = cat(2, stats_grn_distr, stats_red_distr);
    chemo_summed = cat(2, chemo_grn_sum, chemo_red_sum);
    chemo_distro = cat(2, chemo_grn_distr, chemo_red_distr);

    [C, I] = max(grn_distrd);

    column_header1 = {['bg_amt ' int2str(bg_amt(amt))], ' '};
    column_header2 = {'Green',  'Red'};
```

```
    if amt == 1
        xls_summed = summed;
        xls_distro = distro;
        xls_stats_summed = stats_summed;
        xls_stats_distro = stats_distro;
        xls_chemo_summed = chemo_summed;
        xls_chemo_distro = chemo_distro;
        xls_column_header1 = column_header1;
        xls_column_header2 = column_header2;
    else
        xls_summed = cat(2, xls_summed, summed);
        xls_distro = cat(2, xls_distro, distro);
        xls_stats_summed = cat(2, xls_stats_summed, stats_summed);
        xls_stats_distro = cat(2, xls_stats_distro, stats_distro);
        xls_chemo_summed = cat(2, xls_chemo_summed, chemo_summed);
        xls_chemo_distro = cat(2, xls_chemo_distro, chemo_distro);
        xls_column_header1 = cat(2, xls_column_header1, column_header1);
        xls_column_header2 = cat(2, xls_column_header2, column_header2);
    end
end
%Creates the output file name and path
```

```
output1 = strcat(out_path, base_name, '_sum_output.xlsx')

output2 = strcat(out_path, base_name, '_slice_output.xlsx')


%Creates the output file

xlswrite(output1, code_version, 'Sheet1','A1');

xlswrite(output2, code_version, 'Sheet1','A1');

xlswrite(output1, code_version, 'Sheet2','A1');

xlswrite(output2, code_version, 'Sheet2','A1');

xlswrite(output1, code_version, 'Sheet3','A1');

xlswrite(output2, code_version, 'Sheet3','A1');

xlswrite(output1, xls_column_header1, 'Sheet1','A2'); %Write column header

xlswrite(output2, xls_column_header1, 'Sheet1','A2'); %Write column header

xlswrite(output1, xls_column_header2, 'Sheet1','A3'); %Write column header

xlswrite(output2, xls_column_header2, 'Sheet1','A3'); %Write column header

xlswrite(output1, xls_summed, 'Sheet1','A4');

xlswrite(output2, xls_distro, 'Sheet1','A4');

xlswrite(output1, xls_column_header1, 'Sheet2','A2'); %Write column header

xlswrite(output2, xls_column_header1, 'Sheet2','A2'); %Write column header

xlswrite(output1, xls_column_header2, 'Sheet2','B3'); %Write column header

xlswrite(output2, xls_column_header2, 'Sheet2','B3'); %Write column header

xlswrite(output1, xls_stats_summed, 'Sheet2','B4');

xlswrite(output1, stats_row_header, 'Sheet2','A4');
```

```
xlswrite(output2, xls_stats_distro, 'Sheet2','B4');
xlswrite(output2, stats_row_header, 'Sheet2','A4');
xlswrite(output1, xls_column_header1, 'Sheet3','A2'); %Write column header
xlswrite(output2, xls_column_header1, 'Sheet3','A2'); %Write column header
xlswrite(output1, xls_column_header2, 'Sheet3','B3'); %Write column header
xlswrite(output2, xls_column_header2, 'Sheet3','B3'); %Write column header
xlswrite(output1, xls_chemo_summed, 'Sheet3','B4');
xlswrite(output1, chemo_row_header, 'Sheet3','A4'); %Write row header
xlswrite(output2, xls_chemo_distro, 'Sheet3','B4');
xlswrite(output2, chemo_row_header, 'Sheet3','A4'); %Write row header
run = 'Finished Successfully!'
end
function odd = check_odd(num)
    %This function is checking to see if a number is odd.  It then returns
    %a yes (1) or a no (0).  The way it checks is by dividing the number,
    %num, by 2.  It then rounds the result down and multiples by 2.  If the
    %result is different from num, then it is an odd number.  Otherwise it
    %is even.
    %Ex: 5/2 = 2.5  Round down is 2.  2*2 = 4 does not equal 5.  So
    %therefore it is an odd number.  If the number had been 4, then 4/2 = 2
    %which rounded down is still 2.  2*2 = 4 = 4.  Therefore it is even and
    %not odd.
```

```
    tnum = num / 2;
    tnum = floor(tnum);
    if (tnum * 2) == num
        odd = 0;
    else
        odd = 1;
    end
    return;
end

function conc_prof = conc_profile(profile, max_conc, min_conc)
    profile = round(profile);
    max_val = max(profile);
    min_val = min(profile);
    range = max_val - min_val;
    conc_range = max_conc - min_conc;
    slope = conc_range / range;
    len = length(profile);
    for i = 1 : len
        xval = profile(1,i);
        yval = ((xval - min_val) * slope) + min_conc;
        conc_prof(1,i) = yval;
```

```
    end
    return;
end

function avg_prof = pic_profile(xmax, ymax, array)
    avg_prof = [];
    for i = 1 : xmax
        avg_prof(1,i) = y_avg(i, ymax, array);
    end
    return;
end

function avg = y_avg(x_line, ymax, array)
    sum = 0;
    for j = 1 : ymax
        sum = sum + array(j, x_line);
    end
    avg = sum / ymax;
    return;
end

function bg = bg_finder(thresh, bg_per, img_list, filepath, r_max, c_max)
```

```
%Used for finding the background of a series of images
%This function will take the images in the image list and convert them to
%logical matrices based on the thresh hold given.  It will then add them
%all together into a single matrix.  Then based on the percentage given it
%will set the limit and anything above that in the matrix will be consided
%background.  The background matrix will then be returned as the solution
%of the function.
%thresh is the thresh hold set to convert the images to logical (0 & 1's).
%bg_per is the percentage of the total pictures to have the pixel for it to
%be counted as background.
%img_list is the list of the images to be used to find the background.
%filepath is the file path for the file related to working directory.
   bg_test = zeros(r_max, c_max);
   for im = 1 : length(img_list)

      %Gets the image information from the image list
      img_info = img_list(im);
      %Gets the various parts from the filename (in this case path and versn are
         placeholders)
```

```
    [path, name, ext, versn] = fileparts(img_info.name);
    %Adds the correct path to the image relative to the working directory
    img_name = fullfile(filepath,img_info.name);
    %Loads the image
    image = imread(img_name);
    %Converts image to black and white (logical 0 & 1's)
    bw = im2bw(image,thresh);
    bg_test = bg_test + bw;


end
n_limit = floor(bg_per * length(img_list));
[r_max,c_max]=size(bg_test);
bg=[];
for i = 1 : r_max
    for j = 1 : c_max
        if (bg_test(i, j) >= n_limit)
            bg(i, j) = bg_test(i, j);
        else
            bg(i, j) = 0;
        end
    end
end
```

```
    return;
end



function imfull = img_pro(thresh, bg_per, img_list, filepath, r_max, c_max, sec_pic)
%Used for finding the background of a series of images
%This function will take the images in the image list and convert them to
%logical matrices based on the thresh hold given.  It will then add them
%all together into a single matrix.  Then based on the percentage given it
%will set the limit and anything above that in the matrix will be consided
%background.  The background matrix will then be returned as the solution
%of the function.
%thresh is the thresh hold set to convert the images to logical (0 & 1's).
%bg_per is the percentage of the total pictures to have the pixel for it to
%be counted as background.
%img_list is the list of the images to be used to find the background.
%filepath is the file path for the file related to working directory.
    bg_test = zeros(r_max, c_max);


    %Set the number of sections, if sec_pic is equal to 0, then there is
    %only one section because all pictures are analyzed as one section
    if sec_pic == 0
```

```
    sections = 1;
else
    sections = floor(length(img_list)/sec_pic);
end
imfull={};
for secs = 1 : sections
    for ij = 1 : sec_pic
        im = ((secs - 1) * sec_pic) + ij;


        %Gets the image information from the image list
        img_info = img_list(im);
        %Gets the various parts from the filename (in this case path and versn are
placeholders)
        [path, name, ext, versn] = fileparts(img_info.name);
        %Adds the correct path to the image relative to the working directory
        img_name = fullfile(filepath,img_info.name);
        %Loads the image
        image = imread(img_name);
        %Converts image to black and white (logical 0 & 1's)
        bw = im2bw(image,thresh);
        bg_test = bg_test + bw;
    end
```

```
        n_limit = floor(bg_per * length(img_list));
       [r_max,c_max]=size(bg_test);
       impic=[];
       for i = 1 : r_max
          for j = 1 : c_max
             if (bg_test(i, j) >= n_limit)
                impic(i, j) = 0;
             else
                impic(i, j) = bg_test(i, j);
             end
          end
       end
%        return;
       imfull{secs}=impic;
    end
    return
end



function imfull = img_pro_nosec(thresh, bg_per, img_list, filepath, r_max, c_max)
%Used for finding the background of a series of images
%This function will take the images in the image list and convert them to
```

```
%logical matrices based on the thresh hold given.  It will then add them
%all together into a single matrix.  Then based on the percentage given it
%will set the limit and anything above that in the matrix will be consided
%background.  The background matrix will then be returned as the solution
%of the function.
%thresh is the thresh hold set to convert the images to logical (0 & 1's).
%bg_per is the percentage of the total pictures to have the pixel for it to
%be counted as background.
%img_list is the list of the images to be used to find the background.
%filepath is the file path for the file related to working directory.
   bg_test = zeros(r_max, c_max);

   %Set the number of sections, if sec_pic is equal to 0, then there is
   %only one section because all pictures are analyzed as one section
   imfull=[];
   length(img_list)
      for im = 1 : length(img_list)

         %Gets the image information from the image list
         img_info = img_list(im);
         %Gets the various parts from the filename (in this case path and versn are
               placeholders)
```

```
    [path, name, ext, versn] = fileparts(img_info.name);
    %Adds the correct path to the image relative to the working directory
    img_name = fullfile(filepath,img_info.name);
    %Loads the image
    image = imread(img_name);
    %Converts image to black and white (logical 0 & 1's)
    bw = im2bw(image,thresh);
    bg_test = bg_test + bw;
end



n_limit = floor(bg_per * length(img_list));
[r_max,c_max]=size(bg_test);
impic=[];
for i = 1 : r_max
    for j = 1 : c_max
        if (bg_test(i, j) >= n_limit)
            impic(i, j) = 0;
        else
            impic(i, j) = bg_test(i, j);
        end
```

```
            end
        end
%       return;
        imfull = impic;

    return
end

function comp = img_compiler(thresh, bg, img_list, filepath, r_max, c_max)
%Used to subtract out the background from a set of images and then add them
%together into a single matrix.
%thresh is the thresh hold set to convert the images to logical (0 & 1's).
%bg is the background found using the bg_finder function.
%img_list is the list of the images to be used to find the background.
%filepath is the file path for the file related to working directory.
    comp = zeros([r_max, c_max]);
    for im = 1 : length(img_list)

        %Gets the image information from the image list
        img_info = img_list(im);
        %Gets the various parts from the filename (in this case path and versn are
placeholders)
```

```
        [path, name, ext, versn] = fileparts(img_info.name);
        %Adds the correct path to the image relative to the working directory
        img_name = fullfile(filepath,img_info.name);
        %Loads the image
        image = imread(img_name);
        %Converts image to black and white (logical 0 & 1's)
        bw = im2bw(image,thresh);
        %Subtracts the background from the image
        of_int = bw - bg;
        %Adds the remaining logical image to the compiled matrix.  This
        %matrix is a count of the number of positive pixels at the
        %location of the image.
        comp = comp + of_int;
    end
    return;
end

function SliceLimits = SliceSizes(c_max, slices)
    %This function creates the limits for each slice based on the width of
    %image and the number od slices.  It will add any extra to the middle
    %set of slices that is needed.  The extra width will be added from the
    %center out.  If the slices are Odd and the extra is Even, they will
```

```
%add the extra starting on either side of the middle slice.  If the
%Slices are Even and the Extra is Odd, it will start at the left center
%slice.
%c_max is the width or number of columns of the matrix
%slices is the number of slices

%Makes sure the number of slices is an integer
slices = round(slices);

%Check if slices is an odd number (Calls check_odd function)
Odd = check_odd(slices);

%Create Slice Limits (MWOS = Minimum Width Of Slice)
MWOS = floor(c_max / slices);  %Finds min slice width
Extra = c_max - (MWOS * slices);  %Finds how many pixels are left
ExtraOdd = check_odd(Extra);  %Checks if Left Over Pixels is Odd
CenterSlice = ceil(slices / 2);  %Finds Center Slice, rounds up for Odd Slices

%Setting where to start and stop the extra slices
if ExtraOdd == 1
    ExtraSlices = (Extra - 1) / 2;
else
```

```
    ExtraSlices = Extra / 2;
end

if Odd == 1
    ExtraStart = CenterSlice - ExtraSlices;
    ExtraEnd = CenterSlice + ExtraSlices;
else
    ExtraStart = CenterSlice - ExtraSlices + 1;
    ExtraEnd = CenterSlice + ExtraSlices;
end

val = 0;
SliceLimits = [];
for i = 1 : slices
    if (i < ExtraStart) | (i > ExtraEnd)
        max = val + MWOS;
    else
        if (Odd == 1) & (ExtraOdd == 0) & (i == CenterSlice)
            max = val + MWOS;
        elseif (Odd == 0) & (ExtraOdd == 1) & (i == CenterSlice)
            max = val + MWOS +2;
        else
```

```
            max = val + MWOS + 1;
        end
    end
    val = max;
    SliceLimits(i) = max;
  end
  return;
end

function y_struct = y_sum(r_max, c_max, struct)
  %This function will take an array and sum up the columns.  The result
  %is single row matrix with c_max columns.
  [a1, a2] = size(struct);
  %struct
  for ar = 1 : a2
    array = struct{ar};
    y_line = zeros([c_max, 1]);
    for i = 1 : c_max
      sum = 0;
      for j = 1 : r_max
        sum = sum + array(j, i);
      end
```

```
            y_line(i) = sum;
        end
        y_struct{ar} = y_line;
    end
    return;
end

function y_struct = y_sum_nosec(r_max, c_max, struct)
    %This function will take an array and sum up the columns.  The result
    %is single row matrix with c_max columns.
    [a1, a2] = size(struct);
    %struct
        array = struct;
        y_line = zeros([c_max, 1]);
        for i = 1 : c_max
            sum = 0;
            for j = 1 : r_max
                sum = sum + array(j, i);
            end
            y_line(i) = sum;
        end
        y_struct = y_line;
```

```
    return;
end

function distr_struct = Slice_Distr(y_struct, c_max, slices, SliceLimits)
    %Calculate Labeled Item Distribution
    [a1, a2] = size(y_struct);
    for ar = 1 : a2
        y_line = y_struct{ar};
        distr = zeros([slices, 1]);
        for i = 1 : c_max
            cont = 1;
            while cont == 1
                if ((i > 0) & (i <= SliceLimits(1)))
                    if ~distr(1)
                        distr(1) = y_line(i);
                    else
                        distr(1) = distr(1) + y_line(i);
                    end
                    cont = 0;
                else
                    for s = 2 : slices
                        if ((i > SliceLimits(s - 1)) & (i <= SliceLimits(s)))
```

```
                    if ~distr(s)
                        distr(s) = y_line(i);
                    else
                        distr(s) = distr(s) + y_line(i);
                    end
                    cont = 0;
                end
            end
        end
        cont = 0;
    end
end

    distr_struct{ar} = distr;
end

return;
end


function chemo_stats = chemo_coef(input, input_mean, red_mean)
    %Calculates the Shift, CPC, and CMC for the chemotaxis effects
```

```
    %Input is a line array
    %Input_mean is the mean of the input data
    %Red_mean is the mean of the corresponding red data

    shift = input_mean - red_mean;

    mid = floor(length(input)/2);
    low_mid = floor(length(input)/2);
    up_mid = low_mid + 1;
    CPC_Vector = zeros(length(input), 1);
    CMC_Vector = zeros(length(input), 1);

%   L1 = mid - low_mid;
%   U1 = up_mid - mid;

%   if L1 >= U1
%       max = mid - L1;
%   else
%       max = mid - U1;
%   end

    max = mid - 1;
```

```
cell_count = 0;
CPC_sum = 0;
CMC_sum = 0;

for i = 0 : max - 1
   CPC_Vector(low_mid - i) = -1;
   CPC_Vector(up_mid + i) = 1;
   CMC_Vector(low_mid - i) = ((-i - 0.5)/(max + 0.5));
   CMC_Vector(up_mid + i) = (i + 0.5)/(max + 0.5);



   cell_count = cell_count + abs(CPC_Vector(low_mid - i) * input(low_mid - i));
   cell_count = cell_count + abs(CPC_Vector(low_mid + i) * input(low_mid + i));
   CPC_sum = CPC_sum + (CPC_Vector(low_mid - i) * input(low_mid - i));
   CPC_sum = CPC_sum + (CPC_Vector(low_mid + i) * input(low_mid + i));
   CMC_sum = CMC_sum + (CMC_Vector(low_mid - i) * input(low_mid - i));
   CMC_sum = CMC_sum + (CMC_Vector(low_mid + i) * input(low_mid + i));
end

CPC = CPC_sum / cell_count;
```

```
    CMC = CMC_sum / cell_count;


    chemo_stats(1) = shift;
    chemo_stats(2) = cell_count;
    chemo_stats(3) = CPC;
    chemo_stats(4) = CMC;


    return;
end


function centered_data = center_data(grn_array, red_array)
    %Finds the max value of the red data.  It then moves that to the center
    %and makes both sides of the center have an equal number of slices.
    [max_value max_slice] = max(red_array)


    if red_array(max_slice - 1) >= red_array(max_slice + 1)
        if (length(red_array) - max_slice) < (max_slice - 1 - 1)
            startpos = max_slice - 1 - (length(red_array) - max_slice);
            endpos = length(red_array);
        elseif (length(red_array) - max_slice) > (max_slice - 1 - 1)
            startpos = 1;
            endpos = max_slice + (max_slice - 1 - 1);
```

```
        else
            startpos = 1;
            endpos = length(red_array);
        end
%    elseif red_array(max_slice - 1) < red_array(max_slice + 1)
    else
        if (length(red_array) - (max_slice + 1)) < (max_slice - 1)
            startpos = max_slice - (length(red_array) - (max_slice + 1));
            endpos = length(red_array);
        elseif (length(red_array) - (max_slice + 1)) > (max_slice - 1)
            startpos = 1;
            endpos = max_slice + 1 + (max_slice - 1);
        else
            startpos = 1;
            endpos = length(red_array);
        end
    end

    spaces_needed = length(grn_array) - length(grn_array(startpos : endpos));
    end_spaces = spaces_needed / 2;
```

```
    centered_grn = grn_array(startpos : endpos);
    centered_red = red_array(startpos : endpos);
%    centered_centroid = centroid_array(startpos : endpos);

    if end_spaces >= 1
        endfiller = zeros([end_spaces, 1])
        centered_grn = cat(1, endfiller, centered_grn, endfiller);
        centered_red = cat(1, endfiller, centered_red, endfiller);
%        centered_centroid = cat(1, endfiller, centered_centroid, endfiller);
    end


    centered_data{1} = centered_grn;
    centered_data{2} = centered_red;
%    centered_data{3} = centered_centroid;
    return;
end

%%%
```

```
%                                                %
%%%
```

```
% Finds the regions and labels them
label_pic = bwlabel(clnbw2, 4);

% Gets the properties for the regions
stats_pic = regionprops(label_pic, 'basic');

AllArea = [stats_pic.Area];

% Finds Regions with an Area less than __ and creates new image
idx = find([stats_pic.Area] < 100);
bw2 = ismember(label_pic,idx);

% Finds the regions and labels them
label_pic2 = bwlabel(bw2, 4);

% Gets the properties for the regions
stats_pic2 = regionprops(label_pic2, 'basic');

AllArea2 = [stats_pic2.Area];

sA = size(AllArea2);
sA_len = sA(2);
```

```
    sp = size(label_pic2);
    xvector = zeros(1, sp(2));

    % Create Centroid Summary Vector
    for i = 1 : sA_len
        Centroid = [stats_pic2(i).Centroid];
        xl = round(Centroid(1));
        xvector(xl) = xvector(xl) + 1;
    end

    Centroid_Locations = xvector;

    return;

end



% Function to Run a Series of Pictures Through Centroid Locator and Sum Results
function Summed_Centroids = Centroid_Series(picture_array, filepath, threshold)

    for im = 1 : length(picture_array)
```

```
        %Gets the image information from the image list
        img_info = picture_array(im);
        %Gets the various parts from the filename (in this case path and versn are
           placeholders)
        [path, name, ext, versn] = fileparts(img_info.name);
        %Adds the correct path to the image relative to the working directory
        img_name = fullfile(filepath,img_info.name);
        %Loads the image
        image = imread(img_name);


        if im == 1
           Summed_Centroids = Centroid_Finder(image, threshold);
        else
           Summed_Centroids = Summed_Centroids + Centroid_Finder(image, threshold);
        end


    end


    return;


end
```

```
% Function to Slice the Centroid Location Vector
function Sliced_Centroid = Slice_Centroid(vector, slice_len)
    % Create Sliced Centroid Summary Vector
    num_slices = length(vector) / slice_len;
    Sliced_Centroid = zeros(1, num_slices);

    k = 1;
    for i = 1 : num_slices
        for j = 1 : slice_len
        Sliced_Centroid(i) = Sliced_Centroid(i) + vector(k);
        k = k + 1;
        end
    end
    return;
end
function out = No_BG_Centroid_Vector(path, img_list, thresh)
    %path_grn = strcat(in_path, 'green/');
    %path_red = strcat(in_path, 'red/');
    %grn_img_list = dir(strcat(path_grn, '*ch00.tif'));
```

```
    %red_img_list = dir(strcat(path_red, '*ch01.tif'));
    cps = centroid_pic_struct(path, img_list, thresh);

    NBG_pic = Remove_BG(cps); %Creates the summed picture with the background
removed
    NBG_vector = sum(NBG_pic);  %Sums the columns of the picture so that the result is
a vector
    out = NBG_vector;
end

function cent_pic_struct = centroid_pic_struct(path, pic_list, thresh)
    %cent_pic_struct = {};
        for im = 1 : length(pic_list)
        img_info = pic_list(im);
        img_info.name;
        c_pic = centroid_pic(path, img_info.name, thresh);
        cent_pic_struct{im} = c_pic;
        if im == 1
            summed_c_pic = c_pic;
        else
            summed_c_pic = summed_c_pic + c_pic;
        end
```

```
    end
    cent_pic_struct{length(pic_list) + 1} = summed_c_pic;
end



function cent_pic = centroid_pic(path, pic, thresh)
pic1 = imread(strcat(path, pic));
bw1 = im2bw(pic1, thresh);
% Removes Single Pixels
clnbw1 = bwmorph(bw1, 'clean', 1);

% Fills the Single Empty Pixels that are Surrounded by Filled Pixels
flbw1 = bwmorph(clnbw1, 'fill', 1);

% Disconnects Areas COnnected on Diagonal
hbrkbw1 = bwmorph(flbw1, 'hbreak', 2);

% Removes Any Spurs
sprbw1 = bwmorph(hbrkbw1, 'spur', 1);

% Removes Single Pixels
cln2bw1 = bwmorph(sprbw1, 'clean', 1);
```

```
% Finds the regions and labels them
label_pic1 = bwlabel(cln2bw1, 4);

% Gets the properties for the regions
stats_pic1 = regionprops(label_pic1, 'basic');

AllArea = [stats_pic1.Area];

% Finds Regions with an Area less than __ and creates new image
idx = find([stats_pic1.Area] < 100);
bws1 = ismember(label_pic1,idx);

% Finds the regions and labels them
label_pic1 = bwlabel(bws1, 4);

% Gets the properties for the regions
stats_pic1 = regionprops(label_pic1, 'basic');

AllArea = [stats_pic1.Area];

% Finds Regions with an Area greater than __ and creates new image
```

```
idx = find([stats_pic1.Area] > 4);

bws1 = ismember(label_pic1,idx);


% Finds the regions and labels them

label_pics1 = bwlabel(bws1, 4);


% Gets the properties for the regions

stats_pics1 = regionprops(label_pics1, 'basic');


AllAreaS = [stats_pics1.Area];

sA = size(AllAreaS);

sA_len = sA(2);

sp = size(bws1);

cent_pic = zeros(sp);


% Create Centroid Summary Vector

for i = 1 : sA_len

   Centroid = [stats_pics1(i).Centroid];

   xc = round(Centroid(1));

   yr = round(Centroid(2));

   cent_pic(yr,xc) = 1;

end
```

```
end



function No_BG = Remove_BG(test2_out)
    dil_sqr =  [ 1 1 1; 1 1 1; 1 1 1];
    for im = 1 : length(test2_out) - 1
        dil_im = imdilate(test2_out{im}, dil_sqr);
        dil_im_struct{im} = dil_im;
    end
    new_summed_cent_pic = zeros(size(test2_out{1}));
    for im = 1 : length(test2_out) - 1
        if im == 1
            summed_im{im} = dil_im_struct{im};
        elseif im == 2
            summed_im{im} = dil_im_struct{im} + dil_im_struct{im - 1};
        elseif im == 3
            summed_im{im} = dil_im_struct{im} + dil_im_struct{im - 1} +
dil_im_struct{im - 2};
        elseif im == 4
            summed_im{im} = dil_im_struct{im} + dil_im_struct{im - 1} +
dil_im_struct{im - 2} +  dil_im_struct{im - 3};
```

```
else
   summed_im{im} = dil_im_struct{im} + dil_im_struct{im - 1} +
            dil_im_struct{im - 2} + dil_im_struct{im - 3} + dil_im_struct{im - 4};
end


   if im > 5
   di = dil_im_struct{im};
   si = summed_im{im - 1};
   li = ismember(si,5);
   ndi = di - li;
   di_lab = bwlabel(ndi, 8);
   rp = regionprops(di_lab, 'basic');
   idx = find([rp.Area] == 9);
   newim = ismember(di_lab,idx);
   ni_lab = bwlabel(newim, 8);
   rp = regionprops(ni_lab, 'basic');
   sA = size([rp.Area]);
   sA_len = sA(2);
   sp = size(newim);
   di = zeros(sp);

   % Create Centroid Summary Vector
```

```
            for i = 1 : sA_len
                Centroid = [rp(i).Centroid];
                xc = round(Centroid(1));
                yr = round(Centroid(2));
                di(yr,xc) = 1;
            end

        else
            di = test2_out{im};
        end
        new_summed_cent_pic = new_summed_cent_pic + di;
    end
    No_BG = new_summed_cent_pic;
end

function No_BG = Remove_BG2(path, pic_list, thresh, bg_amt)
        dil_sqr =  [ 1 1 1; 1 1 1; 1 1 1];
    cent_pic = cell(bg_amt);
    dil_pic = cell(bg_amt);

    for im = 1 : length(pic_list)
        img_info = pic_list(im);
```

```
img_info.name;
if im <= bg_amt
    cent_pic{im} = centroid_pic(path, img_info.name, thresh);
    dil_pic{im} = imdilate(cent_pic{im}, dil_sqr);
    if im == 1
        size_cent_pic = size(cent_pic{1});
        new_summed_pic = zeros(size(cent_pic{1}));
    end

else
    summed_im = new_summed_pic;
    for i = 1 : bg_amt
        summed_im = summed_im + dil_pic{i};
    end
    for i = 1 : bg_amt - 1
        cent_pic{i} = cent_pic{i+1};
        dil_pic{i} = dil_pic{i+1};
    end

    cent_pic{bg_amt} = centroid_pic(path, img_info.name, thresh);
    dil_pic{bg_amt} = imdilate(cent_pic{bg_amt}, dil_sqr);
    di = dil_pic{bg_amt};
```

```
    si = summed_im;


    li = ismember(si, bg_amt);


    ndi = di - li;
    di_lab = bwlabel(ndi, 8);
    rp = regionprops(di_lab, 'basic');
    idx = find([rp.Area] == 9);
    newim = ismember(di_lab,idx);
    ni_lab = bwlabel(newim, 8);
    rp = regionprops(ni_lab, 'basic');


    sA = size([rp.Area]);
    sA_len = sA(2);
    sp = size(newim);
    for i = 1 : sA_len
        Centroid = [rp(i).Centroid];
        xc = round(Centroid(1));
        yr = round(Centroid(2));
        new_summed_pic(yr,xc) = new_summed_pic(yr,xc) + 1;
    end
end
```

```
    end
    No_BG = new_summed_pic;
end
```

VITA

Name:	Derek Lynn Englert
Address:	Artie McFerrin Department of Chemical Engineering Texas A&M University 200 JEB 3122 TAMU College Station, TX 77843-3122
Email Address:	derekenglert@gmail.com
Education:	B.S., Chemical Engineering, The University of Mississippi, 2002